THE UNIVERSITY OF CHICAGO

DEVELOPING A PLATFORM FOR 2D IR STUDIES OF THE ELECTRIC DOUBLE LAYER AT ELECTROCHEMICAL INTERFACES IN AQUEOUS ELECTROLYTE SOLUTIONS

A DISSERTATION SUBMITTED TO
THE FACULTY OF THE DIVISION OF THE PHYSICAL SCIENCES
IN CANDIDACY FOR THE DEGREE OF
DOCTOR OF PHILOSOPHY

DEPARTMENT OF CHEMISTRY

BY
MELISSA GRACE BODINE

CHICAGO, ILLINOIS
AUGUST 2024

Contents

List of Tables

List of Figures

Acknowledgements

There was no way to foresee all of the challenges graduate school would throw my way, and I would like to sincerely thank my advisor, Andrei, for his calm leadership through all of the trials of graduate school. I have enjoyed learning from him how to approach the most difficult scientific questions with excitement and creativity. He has also worked incredibly hard to foster a group culture that encourages individual growth and is full of respect and scientific curiosity, and I thank him for allowing me to be a part of that culture.

During my first year I knew I wanted to join Andrei's group after spending time with his graduate students and seeing their enthusiasm for the science in the group, and I would like to especially thank Memo and John for mentoring me that first year, and John for being my deskmate and always giving me insight when I was stumped on a problem.

I had the pleasure of working closely with and being mentored by Nick Lewis, who taught me every lab skill I needed and remains a wealth of knowledge on all things spectroscopy. I have appreciated his patience and leadership in lab, and am happy to have been able to continue to work closely with him and celebrate as he transitioned to Assistance Research Professor during my time here.

Some of my favorite times in graduate school have been due to the amazing co-workers I have had. Lukas always made time to look over my shoulder and ~~devastate~~ help me improve my figures, Ram was always there to lighten the mood with his incessantly positive attitude, and Brennan always laughed at my jokes (even though half of them went over his head). Abhirup became a good friend in my time here, and I look forward to working with him in the future. Vepa Rozyyev was an amazing peer mentor and I also look forward to working with him in the future. Yumin has been the best role model I could ask

for, and I am so grateful for the time I have been able to learn from her. I would also like to thank Jakob for his generosity with chocolate, and Seung Yeon for all of our chats and being my international travel buddy on my first overseas trip. Sam Knight has been been eager to learn from day one, and I am excited to see what he does in the future. Liv has been a bright light in the group, bringing new creativity to every project, and I will forever be grateful to them for lending me books. Jill was an okay replacement for Brennan, but she understands too many of my jokes, which will probably get me in trouble one day. Ian has also brought a lot of joy to the office (and protein powder). Chih-Tsun is one of the most genuinely nice people I have ever met, and I am glad to see him thrive during his first year. Anuj joined during my last year, and I appreciate all of his immediate support and positively.

My friends I have made during my time here have been some of the closest I have had, and I would like to personally thank Jesus, Jeri, Danny, Adrian, Julie, and Latte for being an amazing support system and cheering me along the whole way. I am also grateful to all the people I met here in graduate school, including the members of the Engel group who enabled my crippling coffee addiction, and the Mazziotti group members who let me crash their lunches and adopted me into their group. Sam Warren, my partner, deserves the biggest thanks for supporting me through one of the most challenging times of my life, and I look forward to our next adventures, wherever they may be.

My family I would like to thank as well, for keeping me grounded and reminding me that the work I do doesn't matter, as long as I visit them often. My parents John and Lisa I would like to thank for always providing the resources I need, emotionally or otherwise. It is hard to express how much I rely on my relationships with my sisters and brothers, Brian, Shannon, Rachel, Michael, Jenny, Jessie, Lily, Michelle, Laura, and Ben, but I am so

grateful to call them my family.

Funding

This work was supported as part of the Advanced Materials for Energy–Water Systems (AMEWS) Center, an Energy Frontier Research Center funded by the U.S. Department of Energy, Office of Science, Basic Energy Sciences, under Contract DE-AC02-06CH11357. M.B. also acknowledges support by the U.S. Department of Energy Grant DE-SC0014305.

Abstract

Solvation in aqueous electrolyte solutions and at interfaces still has many questions remaining despite being prevalent throughout the energy and water remediation industries. The electrical double layer is where many important dynamical processes such as catalysis and electron transfer occur. The goal of this thesis is to study solvation through development of vibrational probes, and the electrical double layer with two-dimensional infrared (2D IR) spectroscopy to experimentally access the details of the structural dynamics of this complex environment. However, there are several experimental challenges to applying 2D IR spectroscopy to this application, such as assuring the surface specificity of the spectrum, optimizing the signal strength while minimizing spectral distortions from dispersion and Fano lineshapes, and selecting electrode materials that are both sufficiently IR compatible and conductive. Here we will discuss various considerations when designing 2D IR experiments of electrode interfaces, utilizing several substrates and experimental configurations and demonstrate a robust method for 2D IR experiments of electrode interfaces under applied potential that combines non-conducting Si ATR wafers with conductive ITO and thin nanostructured films of plasmonically active Au functionalized with thiol monolayers. We show that layered electrodes on thin Si ATR wafers with thiol monolayers are sensitive to applied potential, and that the distortions in the linear and 2D IR spectra are heavily dependent on the morphology of the Au surface. Additionally, interpretation of spectra taken at the interface is a complex question, and we also discuss possible interpretations in this thesis, as well as suggest future studies that could help to elucidate structural and dynamical processes at the electrochemical interface. Overall, the findings in this thesis contribute to the broader field of electrochemistry and spectroscopy,

offering new tools and methodologies for probing interfacial phenomena at the molecular level.

Chapter 1

Introduction

The main theme throughout this thesis is the idea that continuum theories in the realm of solvation are insufficient to fully describe all of the phenomena observed. This is true in bulk solution where solutes are fully solvated by solution, and at the interface where there is a large perturbation to the bulk solution's ability to form complete solvation shells. Unexplained solvation phenomena are especially ubiquitous in aqueous solutions, where water is the solvent. This thesis works towards developing two-dimensional infrared (2D IR) experiments for studying electrochemical interfaces to explore the molecular level structure and dynamics in the electric double layer. The next few sections contextualize the goal of this thesis, and discuss why 2D IR is appropriate tool, but has yet to be fully developed for electrochemical applications.

1.1 Complex Solvation in Aqueous Electrolyte Solutions

There are two main approaches when using IR spectroscopy as a tool for looking at solvation. The first is to look directly at the solutes or solvent, but this is dependent on having vibrational modes intrinsic to the system that are both bright and sensitive to

changes in solvation. The other approach, which is the one used in this thesis, is to add a vibrational probe that is not native to the system but that can report on its surroundings. The criteria for a good vibrational probe is that they are bright (since the goal is to add a minimum amount so as not to significantly change the system being studied), minimally perturbative to the system under study, and in a clear part of the IR spectrum so that issues with background signal are minimized. This leads to vibrational probes that are generally small molecules, and have functional groups like carbonyls, nitriles, amides, and others.[1–4] These functional groups are especially suited for hydration problems because they are sensitive to the hydrogen bonding (HB) structure as well as the overall local electric field from nearby ions. For these reasons, they have been used by the IR community for various investigations into solvent properties in various conditions.[5–11]
The two main pieces of theory that connect experimental observables to the properties of the system is first-order vibrational electrochromism, which connects the frequency shifts of a normal mode to the local external electric field, and Onsager's reaction field theory, which connects the dielectric of the solvent to the field felt by the vibrational probe.[12–14]
Vibrational electrochromism has had great success with modeling a vibrational probe's frequency shift using perturbation theory to describe the interaction between the local environment and the probe. If taking the results from first-order perturbation theory, we get a linear equation which predicts that the change in frequency of a probe is dependent on the local electric field and the transition dipole moment of the vibrational probe.[13]

$$\Delta\nu = \nu_o - \mu \cdot F_{ons} \tag{1.1}$$

Where the local electric field can be modeled using the Onsager reaction field.[14] This models the space outside of a sphere determined by the molecular radius as a continuum

based on the dielectric constant of the solution. The magnitude of the field felt by any given vibrational mode will be dependent on the magnitude of the transition dipole moment of the vibration, also called the electrochromatic tuning rate. Taken for an isotropic solution, the Onsager field, F_{ons} is shown in Equation 3.2.

$$F_{ons} = \frac{2\mu}{4\pi\varepsilon_o a^3}\frac{(\varepsilon - 1)}{(2\varepsilon + 1)} \tag{1.2}$$

However, while these theories work well for different types of solvents, they fall short when explaining the origin of specific ion effects in aqueous solutions, and we see responses of well-behaved reporters like carbonyl being unexplained by the continuum theories.[3,15–17] This opens up questions about the molecular details of aqueous systems, where due to the complex interactions between the ions, water HB system, and probe, specific interactions may lead to charge transfer effects, and there may be non-intuitive structure in solution that cannot be accounted for in continuum theories. Additionally, different vibrational probes may be sensitive to different specific interactions, and understanding how each probe is sensitive to molecular level interactions is key to selecting probes suited to the study at hand.

1.2 The Electric Double Layer Structure and Continuum Theories

Clearly, solvation is a tricky question even in bulk solutions. How does the solvation structure of water and ions change at the electrochemical interface? The study of electrochemical interfaces, particularly the electric double layer (EDL), has long been a

cornerstone of understanding processes in electrochemistry.[18–20] Traditional continuum theories, such as the Gouy-Chapman-Stern model, have provided foundational insights into the behavior of ions at these interfaces.[21–24] These models effectively describe the distribution of electric potential and charge density near the electrode surface by treating the solvent as a continuous dielectric medium and the ions as point charges. An example illustration is shown in Figure 1.1, showing the key components of the electric double layer, including the Stern layer of adsorbed counter ions onto the charged surface, the diffuse layer where the concentration of counter ions are greater than the complementary ion, and the bulk solution.

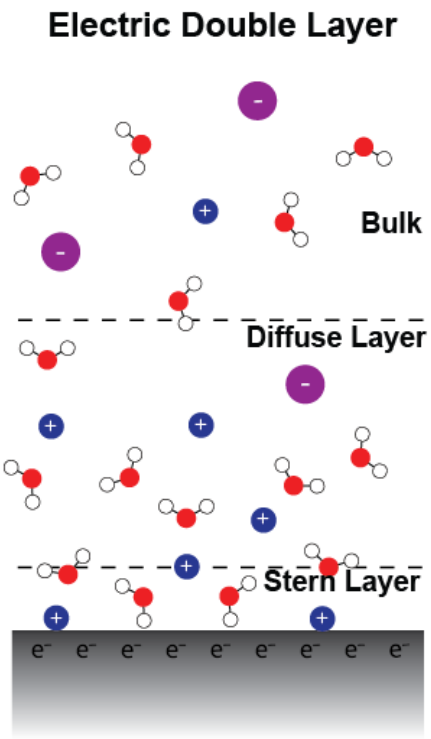

Figure 1.1: Illustration of the electric double layer, including a Stern layer of adsorbed counter ions, a diffuse layer where counter ions are more concentrated than their complement ion, and the transition into bulk-like solution.

Also included in the illustration is water as the solvent, which is not included in classical models. These classical models fall short in capturing the complex, molecular-level interactions and dynamics that occur at the solid-liquid interface.[25–27] Continuum theories often fail to account for the discrete nature of solvent molecules, specific ion effects, and the detailed structural organization at the interface. For instance, they do not consider the spatial arrangement and orientation of water molecules, which can significantly influence the properties and behavior of the EDL.[28,29] Furthermore, these models cannot adequately describe the influence of molecular interactions such as hydrogen bonding and ion pairing, which are critical for understanding the behavior of solvated ions and molecules at electrochemical interfaces.

1.3 2D IR for Studying Interfacial Dynamics

The properties of the electric double layer's structure and dynamics at solid-liquid interfaces is still not fully understood, despite being vitally important to a wide class of problems. These problems include developing efficient materials for water remediation, where controlling specific adsorbate-adsorbent interactions is important for selective filtration and recycling of water-soluble finite resources, and range to understanding the impact of fluctuations in the electric double layer (EDL) on important electrochemical processes such as catalysis and electron transfer.[18,30,31] The examples mentioned above all have similar questions remaining, related to how the water in the EDL dynamically restructures to accommodate solutes being adsorbed/desorbed, surface reactions, and interfacial charge transfer. Investigating these problems remains difficult because of the complex interplay between the solution, solutes, and electrochemical interface that imparts

a large electric field on the system and complicates interpretation of experiments.[19] The advantage of using vibrational spectroscopy to study solid-liquid interfaces is the detailed information it can provide related to molecular structure, and by combining vibrational spectroscopy with electrochemical techniques it is possible to specifically isolate small changes in the monolayer species that are impacted by the surface potential.[32] There is a long history of the development of surface enhanced IR (SEIRAS), Raman (SERS) and sum frequency generation (SFG) methods for vibrational spectroelectrochemical measurements,[33–41] with the scientific focus ranging from problems in catalysis to voltage-sensitive biomolecules and fundamental properties of solutions at an electrified interface.[42–49] With the addition of ultrafast techniques, such as 2D IR, it is possible to obtain additional insights into the dynamics of the system on the timescales of molecular vibrations.[50,51] Of particular interest to us is the change in the hydrogen-bonding structure and dynamics at electrode-electrolyte interfaces, and the dynamical role of water in electrochemical processes. Additionally, specific ion effects influence the EDL properties and understanding the origin of these influences can help to inform the design of more efficient electrode-electrolyte systems for important applications such as CO_2 reduction.[52]

1.4 Thesis Outline

This thesis aims to develop and apply 2D IR spectroscopy to study electrochemical interfaces. By using this advanced spectroscopic technique, we hope to gain new insights into the solvation structure, ion distribution, and dynamic processes that govern the behavior of electrochemical systems. Our approach involves the use of tethered vibrational probes to investigate the influence of different solvents, electrode materials, and applied

potentials on the EDL. The majority of this thesis will focus on the design challenges associated with adapting 2D IR to investigate electrochemical interfaces. A summary of what is covered in each chapter is below.

Chapter 2 will discuss the theoretical background and experimental setup for 2D IR spectroscopy, including considerations when moving to ATR geometries and the importance of substrate selection. This chapter aims to prepare the reader for interpreting the 2D IR spectra presented in later chapters, and provide an understanding of the physical setup for the experiments.

Chapter 3 looks at potential vibrational probes, and how the vibrational shifts correlate to specific ion properties in aqueous electrolyte solutions. This chapter highlights the importance of selecting an appropriate vibrational probe for the question being asked, since each vibrational probe presented has a unique response to the identity of the electrolytes present in solution.

Chapter 4 covers the theory of plasmonic enhancement, which is critical to the success of the experiments in this thesis, and includes an experimental evaluation of several possible IR substrates for ATR geometries. It also includes a experimental measurement of the enhancement factor at the surface for a thin sputtered gold film, which shows rapid decay of the plasmon away from the surface.

Chapter 5 is the bulk of the thesis and covers the experimental fabrication details and initial characterization of the electrochemical system designed for 2D IR, as well a discussion of the plasmonic and potential effects on the experimental spectra. It brings together the background and experiments done in several of the previous chapters in order to form a test system for experimentally looking at the electric double layer, and demonstrates the validity of the experimental technique.

Chapter 6 investigates the vibrational dynamics of the monolayer test system used in this thesis, as well as effects of the surface on solvatochromism. It explores the possible pictures that could give rise to the complex, information rich 2D IR spectra measured at the interface of both non-electrified and electrified interfaces.

Chapter 7 summarizes future directions and key next steps to designing experiments within the large parameter space that exists for electrochemical systems, including ideas for improving the spectroscopic quality, ideal test systems for electron transfer at interfaces, and vibrational probe design.

Chapter 2

Theory and Experiment for ATR 2D IR

2.1 Introduction

The first SEIRAS spectrum was taken in 1980 by Hartstein, Kirtley, and Tsang,[53] and the field continued to advance rapidly, driven by development in nanofabrication that allowed more refined approaches to optimizing plasmons for IR enhancement.[54] However, it wasn't until 1998 that the first 2D IR spectrum was reported by Hamm, Lim, and Hochstrasser[55], and even longer until 2D IR was applied to electrochemical interfaces. Since then, there has been interest from many 2D IR groups in integrating 2D IR with electrode interfaces. While integrating 2D IR with electrode interfaces comes with its own set of experimental challenges beyond that of SEIRAS, it provides a large toolbox to build surface-sensitive 2D IR experiments. This is evident in the variety of ways 2D IR has been successfully used to study electrochemical interfaces.[56–58]

However, because there are so many experimental approaches that can be used, it is important to understand the design principles so that an appropriate approach can be used for the question at hand. This chapter has three main parts, the first aims to guide the reader on how to interpret a 2D IR spectrum, and the relevant information contained in a

linear vs 2D IR spectrum. The theoretical basis for linear and 2D IR has been explored in detail many other places, and only the information relevant to the experiments in this thesis is summarized here.

The second part of this chapter covers the experimental details and considerations, the goal of which is to provide an appreciation for the experimental hurdles when applying 2D IR spectroscopy as a surface-sensitive method to look at electrochemical interfaces. This section will focus on the geometry used in our experiments, the Kretschmann attenuated total reflection (ATR) geometry with Si as the ATR material. Si was chosen for the ATR material after testing a few different promising materials. The discussion and results of those material tests are in Chapter 5.

The last section of the chapter describes the ultra fast IR system used, and the data collection and processing details.

2.2 Interpreting IR and 2D IR spectra

2.2.1 The Response Function

The basis of coherent spectroscopy is observing the result of light-matter interactions. To understand these interactions, we need to ultimately connect our experimental observables to the matter properties. We start by describing the material as a collection of quantum mechanical dipole moments $\boldsymbol{\mu}$, that have an induced macroscopic polarization $\mathbf{P}$ upon interaction with an external oscillating electric field $\mathbf{E}$.

$$\mathbf{E}_{in}(\mathbf{r},t) = A_0(\mathbf{r},t)exp(-i\omega t + i\mathbf{k}\cdot\mathbf{r}) + c.c. \tag{2.1}$$

The incident electric field(s), $\mathbf{E}_{in}$, are described classically as a transverse plane wave with angular frequency ω, propagating in the direction of the wavevector $\mathbf{k}$, with amplitude A.

$$\mathbf{P}(\mathbf{r},t) = P(t)exp(-i\omega t + i\mathbf{k_{sig}}\cdot\mathbf{r}) + c.c. \tag{2.2}$$

The resulting polarization, $\mathbf{P}$, can be shown to have the form of a plane wave that is shifted in phase from the electric field by a factor of $\pi/2$. The resulting polarization is coupled to the electric field through Maxwell's equations.

$$\nabla^2\mathbf{E}(\mathbf{r},t) - \frac{1}{c^2}\frac{\partial^2\mathbf{E}(\mathbf{r},t)}{\partial^2 t^2} = \frac{4\pi}{c^2}\frac{\partial^2\mathbf{P}(\mathbf{r},t)}{\partial^2 t^2} \tag{2.3}$$

Where c is the speed of light in a vacuum. The resulting oscillating polarization then emits another electric field that is our signal. For linear IR spectroscopy the electric field is weak enough that the polarization scales linearly with the field. However, for pulsed lasers the electric field amplitude can be large enough to result in non-linearity in the polarization, in which case we can expand the polarization by the order of non-linearity.

$$P(t) = P^{(0)}(t) + P^{(1)}(t) + P^{(2)}(t) + P^{(3)}(t) + ... \tag{2.4}$$

Where the n^{th} order terms arise from n light-matter interactions and scale to the n^{th} power in the electric field, as shown by writing the polarization expansion in the frequency domain in terms of the susceptibility of the material χ.

$$\mathbf{P}(\omega) = \chi^{(1)}\mathbf{E}(\mathbf{r},t) + \chi^{(2)}\mathbf{E}^2(\mathbf{r},t) + \chi^{(3)}\mathbf{E}^3(\mathbf{r},t) + \chi^{(4)}\mathbf{E}^4(\mathbf{r},t) + ... \tag{2.5}$$

We can also relate the polarization to the emitted electric field, $\mathbf{E}_{sig}$, by using the slowly

varying envelope approximation and integrating Equation 2.3. The absorption spectrum is related to Equation 2.5 through the imaginary part of the susceptibility.

$$\mathbf{E}_{sig}(\mathbf{r},t) = i\frac{2\pi\omega_{sig}}{nc} l\mathbf{P}(t) sinc\left(\frac{\Delta\mathbf{k}_{sig}l}{2}\right) exp\left(\frac{\Delta\mathbf{k}_{sig}l}{2}\right) \tag{2.6}$$

There are few important conclusions to be taken from Equation 2.6. One, we can see that the generated electric field is proportional to the nonlinear polarization with an additional π phase shift. There is also a spatial dependence within the sinc function ($sinc = sin(x)/x$), which peaks at $x = 0$ and means that the generated electric field will only have efficient radiation when $\Delta k_{sig} = 0$, called the phase-matched direction. To relate the macroscopic polarization to the microscopic states of the system, we can use the quantum Liouville equation,

$$\frac{\partial}{\partial t}\rho(t) = -\frac{i}{\hbar}\left[H(t), \rho(t)\right] \tag{2.7}$$

Where $\rho(t)$ is the density matrix of our system. In the semi-classical regime with the matter being treated quantum mechanically and the electric field perturbation being treated classically, we describe our Hamiltonian as,

$$H(t) = H_0(t) + \mathbf{V}(t) \tag{2.8}$$

Here H_0 is the unperturbed system and $V(t)$ is the perturbation that couples the electric field to the system. Under the electric dipole approximation, $V = -\boldsymbol{\mu} \cdot \mathbf{E}$.

$$\mathbf{P}(\mathbf{r},t) = \sum_i \mu_i(\mathbf{r},t) = \langle \mu_i(\mathbf{r},t)\rho(t)\rangle \tag{2.9}$$

The polarization is related to the density matrix of our system through the expectation value of the dipole operator. If we use time dependent perturbation theory to find a solution to the quantum Liouville equation, the resulting polarization can be expressed in the interaction picture as a perturbative expansion of the density matrix. For the n^{th} order polarization, this becomes,

$$P^{(n)}(t) = \left(\frac{-i}{\hbar}\right)^n \int_{t_0}^{t} dt_n ... \int_{t_0}^{t} dt_2 \int_{t_0}^{t} dt_1 \left\langle \mu(t) \left[V(t_n) ... \left[V(t_2) \left[V(t_1), \rho(t_0)\right]\right] ...\right]\right\rangle \tag{2.10}$$

If we change the time ordering to reflect a series of incident pulses and substitute in the interaction term $V(t)$, we can separate out the electric field from the material degrees of freedom, which are contained in our important result, the response function, $R(t)$.

$$\begin{aligned} P^{(n)}(t) = \int_{-\infty}^{\infty} d\tau_n ... \int_{-\infty}^{\infty} d\tau_2 \int_{-\infty}^{\infty} d\tau_1 E(t-\tau_n) E(t-\tau_n-\tau_{n-1}) \\ ... E(t-\tau_n-...-\tau_1) R^{(n)}(\tau_1 ... \tau_n) \end{aligned} \tag{2.11}$$

$$\begin{aligned} R^{(n)}(\tau_1 ... \tau_n) = \left(\frac{i}{\hbar}\right)^n <[\mu(\tau_n + ... + \tau_2 + \tau_1]), \\ ...[\mu(\tau_2+\tau_1), [\mu(\tau_1), \mu(0)]]...]\rho_{eq} > \theta(\tau_1) ... \theta(\tau_n) \end{aligned} \tag{2.12}$$

Here we have set $t_0 = -\infty$, $t_1 = 0$, and defined the time intervals $\tau_i = t_{i+1} - t_i$. The $\theta(\tau_i)$ terms are step functions that enforce causality of the light-matter interactions. We have already shown the relationship between the polarization and the emitted signal electric field, and in an experiment the incident electric fields are light pulses that are under our

control. Therefore, in order to fully understand the emitted signal electric field, we need to understand the response function.

2.2.2 Linear Absorption Spectroscopy

For a linear IR spectrum, we can write the first order polarization as a convolution of the external electric field and the linear response function, as previously shown in Equation 2.11, where the linear response function is essentially a single dipole correlation function.

$$P^{(1)}(t) = \int_{-\infty}^{\infty} d\tau E(t-\tau) R^{(1)}(\tau) \tag{2.13}$$

$$\begin{aligned} R^{(1)}(\tau) &= \frac{i}{\hbar} < [\mu(\tau), \mu(0)]\rho_{eq} > \theta(\tau) \\ &= \frac{2}{\hbar} \Im \left(C_{\mu\mu}(\tau) \right) \theta(\tau) \end{aligned} \tag{2.14}$$

$$C_{\mu\mu}(\tau) =< \mu(\tau)\mu(0)\rho_{eq} > \tag{2.15}$$

In the above equations $C_{\mu\mu}$ is the dipole correlation function that describes the response function R, which is in turn related back to the induced polarization, P, from the incident light field, E. In the case of a single unperturbed particle with Hamiltonian H_0, the correlation function can be written as,

$$\begin{aligned} C_{\mu\mu}(\tau) &= \sum_a p_a \left\langle a \left| e^{iH_B\tau/\hbar} \mu e^{-iH_B\tau/\hbar} \mu \right| a \right\rangle \\ &= \sum_a \sum_b p_a \left| \mu_{ba} \right|^2 e^{-i\omega_{ba}\tau} \end{aligned} \tag{2.16}$$

Where $< a|$ and $< b|$ are eigenstates of H_0, p_a is the distribution of states in $< a|$ according to a Boltzmann distribution, and $\omega_{ba} = (E_b - E_a)/\hbar$. In condensed phases, particle-particle interactions are quite strong, and it is easier to separate the Hamiltonian into our system DOF, H_S, that contains the "bright" states observed during experiment, the unobserved "dark" states, H_B, and the system-bath coupling, H_{SB}.

$$H_0 = H_S + H_B + H_{SB} \tag{2.17}$$

For a system and bath that are adiabatically separated with weak coupling, the correlation function becomes,

$$\begin{aligned} C_{\mu\mu}(\tau) &= \sum_a \sum_b p_a \left\langle \mu_{ba}(\tau)\mu_{ba}(0)e^{-i\int_0^\tau d\tau' \omega_{ba}(\tau)} \right\rangle_B \\ \mu_{ba}(\tau) &= e^{iH_B\tau/\hbar}\mu_{ba}e^{-iH_B\tau/\hbar} \end{aligned} \tag{2.18}$$

For the purpose of illustrating the relationship between the dipole-dipole correlation function and the linear absorption spectrum, we can further simplify Equation 2.18 by using the Condon approximation that assumes adiabatic separation between the electron and nuclear DOF, and assuming the fluctuations in the bath are Gaussian, which can be done by truncating the cumulant expansion at the second order. Our dipole correlation function can now be expressed as,

$$C_{\mu\mu}(\tau) = |\mu_{ba}|^2 e^{-i\overline{\omega}_{ba}\tau} e^{-g(\tau)} \tag{2.19}$$

Where $g(\tau)$ is the lineshape function that is determined by the autocorrelation function of the frequency fluctuations ($\delta\omega$) from the mean frequency (ω_{ba}).

$$g(\tau) = \int_0^\tau d\tau'(\tau - \tau') \left\langle \delta\omega_{ba}(\tau')\delta\omega_{ba}(0) \right\rangle \tag{2.20}$$

So the lineshape function is a frequency-frequency correlation function (FFCF). In the Gaussian stochastic model, the FFCF is treated as a single exponential decay with correlation time τ_c, leading to a lineshape function of the form,

$$g(\tau) = \Delta^2\tau_c^2 \left(e^{-\tau/\tau_c} + \frac{\tau}{\tau_c} - 1 \right) \tag{2.21}$$

Where Δ is the static distribution of oscillators with different frequencies. In the inhomogeneous limit, $\tau_c >> \tau$, and the linewidth is determined by Δ. This leads to a Gaussian dipole correlation function.

$$C_{\mu\mu}(\tau) = |\mu_{ba}|^2 \, e^{-i\overline{\omega}_{ba}\tau} e^{-\Delta^2\tau^2/2} \tag{2.22}$$

We can recall that the linear absorption spectrum is proportional to the imaginary part of the linear susceptibility, which is in turn the Fourier transform of the response function. This means that for a Gaussian dipole correlation function the lineshape in the frequency domain should be Gaussian as well.

In the homogeneous limit, $\tau_c << \tau$, the bath fluctuations are now faster than the experimental time limit and the dipole function will decay exponentially, leading to a Lorentzian lineshape in the frequency domain. In this limit the linewidth is determined by the dephasing rate $\Gamma = \Delta^2\tau_c$.

$$C_{\mu\mu}(\tau) = |\mu_{ba}|^2 \, e^{-i\overline{\omega}_{ba}\tau} e^{-\Gamma\tau} \tag{2.23}$$

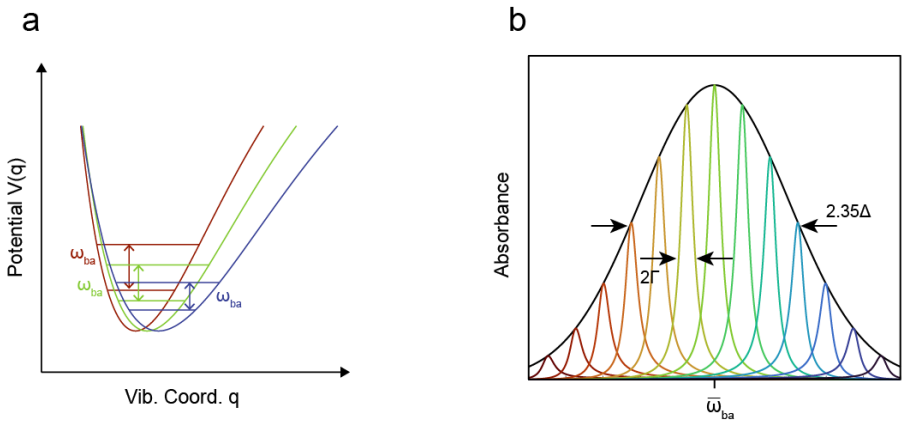

Figure 2.1: (a) Potential energy diagrams plotted to show relationship to frequency in the anharmonic oscillator picture. (b) Contributions of static distribution of homogeneous linewidths to overall FTIR spectrum.

Both the homogeneous and inhomogeneous lineshapes are convolved in the linear spectrum, and it is not possible to separate the two contributions, as illustrated in Figure 2.1. This is one advantage to 2D IR spectroscopy, where the contributions are separated, as will be shown in the next section.

2.2.3 Third Order Response Function

In the third order response function that describes a 2D IR spectrum, there are three light matter interactions before signal emission. This corresponds to two "pump" IR pulses and a third "probe" IR pulse and then signal emission, with corresponding time delays illustrated in Figure 2.2.

For experiments done in the pump-probe geometry such as the ones in this thesis, the signal field is emitted colinearly with the probe pulse with phase matching conditions $k_{sig} = \pm k_1 \mp k_2 + k_3$. Therefore we can say the the signal is heterodyned with the probe pulse, where the probe pulse acts as the local oscillator (LO). This is important becuase it

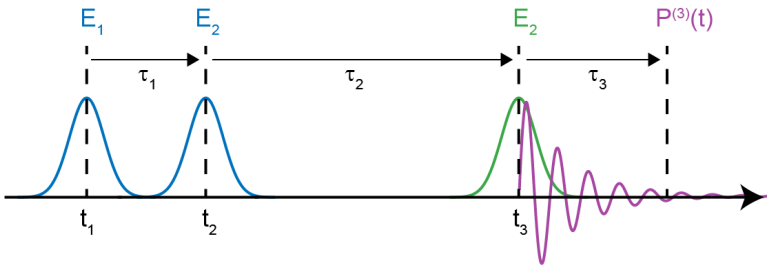

Figure 2.2: Pulse sequence for 2D IR experiment showing the two pump pulses E_1 and E_2, probe pulse E_3, and resulting polarization response $P^{(3)}(t)$. Delay times between pulses are τ_i, and represents the time between the peak maxima at t_i.

allows for information on the phase of the signal to be collected relative to the LO, since otherwise only the intensity is measured in an experiment. For a heterodyned signal, the measured intensity is approximated as the intensity of the LO and the interference between the LO and signal. This is an appropriate approximation because the signal field is much smaller than the LO. Through subtraction of the LO, only the interference term can be collected, which contains information on the phase difference between the signal and LO, ϕ_{sig}.

$$\begin{aligned} I(\omega) &= \frac{nc}{4\pi} \left| E_{sig}(\omega) + E_{LO}(\omega) \right|^2 \\ S(\omega) = \Delta I(\omega) &\approx \frac{nc}{4\pi} \left| E_{sig}(\omega) \right| \left| E_{LO}(\omega) \right| cos(\phi_{sig}) \end{aligned} \tag{2.24}$$

Now with Equations 2.24 and 2.6 we can directly relate the experimental observables to the response function, which we can in turn relate to a sum of correlation functions in a similar manner as we did for the linear case.

$$\begin{aligned} R^{(3)}(\tau_1,\tau_2,\tau_3) &= \left(\frac{i}{\hbar}\right)^3 \langle[\mu(\tau_3+\tau_2+\tau_1)[\mu(\tau_2+\tau_1)[\mu(\tau_1),\mu(0)]]]\rho_{\text{eq}}\rangle \\ &\quad ...\theta(\tau_1)\theta(\tau_2)\theta(\tau_3) \\ &= \left(\frac{i}{\hbar}\right)^3 \sum_{j=1}^{4} R_j^{(3)}(\tau_1,\tau_2,\tau_3) - R_j^{(3)*}(\tau_1,\tau_2,\tau_3) \end{aligned} \tag{2.25}$$

Where each dipole-dipole correlation function is evaluated at four points in time with three time delays. We can re-write the dipole terms to reflect the time-ordered sequence of events and whether the operators are acting on the bra (right) or ket (left) side of the density matrix. This can be done using the cyclic invariance of the trace, and by convention the last interaction is always placed on the ket side.

$$\begin{aligned} R_1^{(3)}(\tau_1,\tau_2,\tau_3) &= \langle\mu(\tau_3+\tau_2+\tau_1)\mu(0)\rho_{eq}\mu(\tau_1)\mu(\tau_1+\tau_2)\rangle\,\theta(\tau_1)\theta(\tau_2)\theta(\tau_3) \\ R_2^{(3)}(\tau_1,\tau_2,\tau_3) &= \langle\mu(\tau_3+\tau_2+\tau_1)\mu(\tau_1)\rho_{eq}\mu(0)\mu(\tau_1+\tau_2)\rangle\,\theta(\tau_1)\theta(\tau_2)\theta(\tau_3) \\ R_3^{(3)}(\tau_1,\tau_2,\tau_3) &= \langle\mu(\tau_3+\tau_2+\tau_1)\mu(\tau_1+\tau_2)\rho_{eq}\mu(0)\mu(\tau_1)\rangle\,\theta(\tau_1)\theta(\tau_2)\theta(\tau_3) \\ R_4^{(3)}(\tau_1,\tau_2,\tau_3) &= \langle\mu(\tau_3+\tau_2+\tau_1)\mu(\tau_1+\tau_2)\mu(\tau_1)\mu(0)\rho_{eq}\theta(\tau_1)\theta(\tau_2)\theta(\tau_3)\rangle \end{aligned} \tag{2.26}$$

Again, similar to the linear case, we make use of the Condon approximation as well as separate our system and bath DOF to obtain the dipole correlation functions in terms of the transition dipole matrix elements, μ, oscillation center frequencies, ω, and lineshape function F, which now depends on three time intervals as opposed to one for the linear case. The different contributions to the 2D spectrum can be split up by the transition frequencies and oscillations during τ_1 and τ_3, as well as the population state in τ_2. For a

single oscillator that is weakly anharmonic, we can use a three-level system and write out the six appropriate response functions that will contribute to the spectrum.

$$\begin{aligned}
R_1^{(3)}(\tau_1,\tau_2,\tau_3) &= p_0\mu_{01}\mu_{01}^*\mu_{10}^*\mu_{10}exp(-i\omega_{10}\tau_1 - i\omega_{10}\tau_3)F(\tau_1,\tau_2,\tau_3)\\
R_2^{(3)}(\tau_1,\tau_2,\tau_3) &= p_0\mu_{01}\mu_{01}^*\mu_{10}\mu_{10}^*exp(-i\omega_{01}\tau_1 - i\omega_{10}\tau_3)F(\tau_1,\tau_2,\tau_3)\\
R_3^{(3)}(\tau_1,\tau_2,\tau_3) &= p_0\mu_{01}\mu_{10}\mu_{01}^*\mu_{10}^*exp(-i\omega_{01}\tau_1 - i\omega_{10}\tau_3)F(\tau_1,\tau_2,\tau_3)\\
R_4^{(3)}(\tau_1,\tau_2,\tau_3) &= p_0\mu_{01}\mu_{10}\mu_{01}\mu_{10}exp(-i\omega_{10}\tau_1 - i\omega_{10}\tau_3)F(\tau_1,\tau_2,\tau_3)\\
R_1^{(3)*}(\tau_1,\tau_2,\tau_3) &= p_0\mu_{12}\mu_{21}\mu_{10}\mu_{10}^*exp(-i\omega_{01}\tau_1 - i\omega_{21}\tau_3)F(\tau_1,\tau_2,\tau_3)\\
R_2^{(3)*}(\tau_1,\tau_2,\tau_3) &= p_0\mu_{12}\mu_{21}\mu_{10}^*\mu_{10}exp(-i\omega_{10}\tau_1 - i\omega_{21}\tau_3)F(\tau_1,\tau_2,\tau_3)
\end{aligned} \tag{2.27}$$

Here $R_1 \rightarrow R_4$ all oscillate at ω_{10} during τ_1 and τ_3, but R_1 and R_2 are in $|1\rangle\langle 1|$ during τ_2 and those pathways are called stimulated emission (SE). R_3 and R_4 are in $|0\rangle\langle 0|$ during τ_2 and are referred to as the ground state bleach (GSB) pathways. Both R_1^* and R_2^* oscillate at ω_{21} during τ_3 and contribute to the excited state absorption (ESA) peak. Additionally, $R_1 \rightarrow R_4$ are all positively signed and lead to an increase in the light transmitted in and experiment due to an even number of bra side interactions, each of which contributes a negative term. However, R_1^* and R_2^* are negative and correspondingly lead to a loss of transmitted light. Additionally, each response function can be described as rephasing or non-rephasing depending on if the phase acquired in τ_1 and τ_3 is the same (non-rephasing) or different (rephasing). However, these contributions are only separated in the boxcar geometry, and for the pump-probe geometry used in this thesis both are collinear and collected simultaneously leading to a pure absorption spectrum.

2.2.4 Interpreting 2D IR spectra

To plot a 2D spectrum, τ_1 and τ_3 are Fourier transformed to provide the excitation and detection axis, respectively, and the real part of the measured spectrum is plotted at measured τ_2 waiting times. Our spectrum is therefore,

$$S_{2D}(\omega_1, \tau_2, \omega_3) \propto \Re \left[\int_{-\infty}^{\infty} d\tau_3 e^{i\omega_3 \tau_3} \int_{-\infty}^{\infty} d\tau_1 e^{i\omega_1 \tau_1} R^{(3)}(\tau_1, \tau_2, \tau_3) \right] \tag{2.28}$$

An example spectrum is plotted in Figure 2.3b, where we have assumed a simple population relaxation T_1, and dephasing Γ so that our lineshape function can be expressed as,

$$F(\tau_1, \tau_2, \tau_3) = e^{-\Gamma\tau_1 - \tau_2/T_1 - \Gamma\tau_3} \theta(\tau_1)\theta(\tau_2)\theta(\tau_3) \tag{2.29}$$

In Figure 2.3, the detection frequency axis separates out ω_{10} and ω_{21}, and the separation between the two, α, is a measure of the anharmonicity of the system since for a perfectly harmonic system $\omega_{10} = \omega_{21}$. The intensity of the peaks in the spectrum depends on the number of contributing pathways and the transition dipole such that the GSB + SE $\propto 4|\mu_{10}|^2$, while ESA $\propto 2|\mu_{21}|^2|\mu_{10}|^2$. If we approximate the transition dipole strength to that of a harmonic oscillator, $\mu_{21} = \sqrt{2}|\mu_{10}|$, and the positive and negative peaks will have the same intensity.

The lineshape is further a measure of the correlation between the initial excited oscillators and the detected oscillations. After the initial IR pulse perturbation, there is an excitation of an ensemble of oscillators in a distribution of molecular environments. Over waiting time τ_2, the bath environment fluctuates, leading to a loss of correlation between excited and detected oscillations due to changing molecular environments. We can see how the loss of correlation affects the lineshape in Figure 2.4, where the Gaussian-stochastic model in

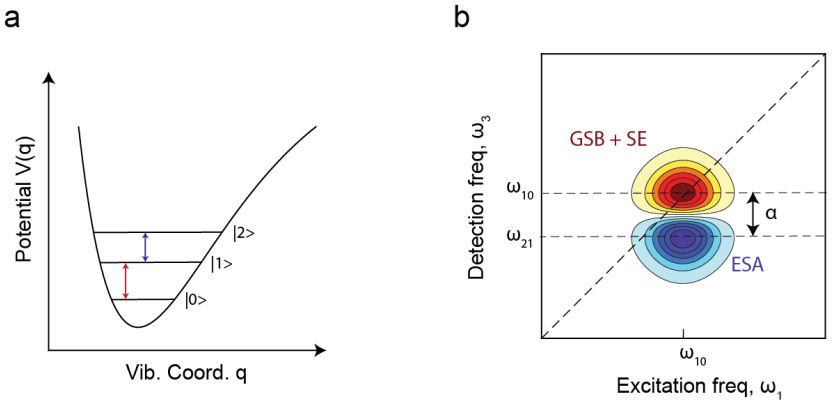

Figure 2.3: (a) Potential energy diagram and (b) corresponding 2D IR spectrum.

Equation 2.21 was employed to look at the limits of homogeneous and heterogeneous broadening, with correlation time τ_c and linewidth Δ. We see that the diagonal width is due to both homo- and heterogeneous broadening, while the antidiagonal is due to purely homogeneous broadening. This leads to several methods of extracting information about the dynamics of the FFCF that was not possible in the linear spectrum. For example, we can measure changes in the lineshape as we change the waiting time τ_2, which will correlate to the dynamics of the FFCF during τ_2. There are a few different ways to quantify the change in lineshape. One is the center line slope (CLS) through the local maxima, another is the nodal line slope (NLS) between the positive and negative features. The ellipticity (ELP) of the peak can also be used, which fits the diagonal (a) and antidiagonal (b) widths and calculates ELP $= \frac{a^2-b^2}{a^2+b^2}$. In Figure 2.4 that the ELP lineshape parameters decay on the same timescale as the FFCF. Note that the ELP does not decay fully to zero because of overlap with the ESA.

2D IR spectroscopy can also provide information on correlations between vibrations when two or more peaks are present in a spectrum. If the two vibrations are correlated, this will be seen as an additional change in absorbance at the cross section between the two

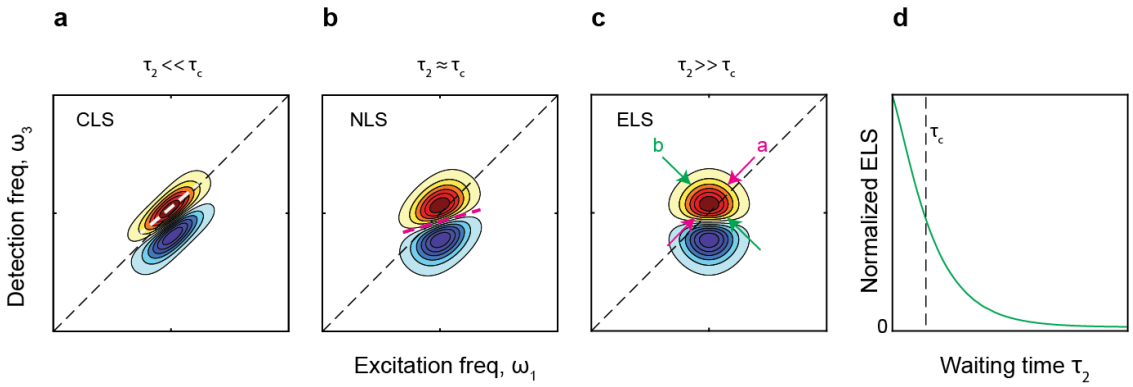

Figure 2.4: (a-c) Model 2D IR spectrum as a function of increasing waiting time showing the homogeneous broadening and (d) ELP decay.

frequencies, called a crosspeak. Crosspeaks can arise from anharmonic coupling between two oscillators, in which case the crosspeak will be present at $\tau_2 = 0$, or they can arise from chemical exchange where an oscillator exchanges configurations. If the latter case, then the crosspeak will grow in with increasing τ_2 times. Further ways of extracting information from crosspeaks is not explored here since there are no clear crosspeaks in the data presented in this thesis.

2.3 Kretchmann ATR Geometry for Interfacial Spectroscopy

2.3.1 Angle of Incidence and Critical Angle

For interfacial electrochemical experiments the Kretschmann ATR configuration is preferred because it provides advantages when designing the electrochemical cell. In spectroelectrochemistry it can become technically difficult to fit a working, reference, and counter electrode in between two sample cell windows that need to be close together (on

the order of μm for aqueous solutions) to reduce solvent background. This is true for both transmission and external reflection experiments, where the beam will pass fully through the solvent at least once. If the windows are too close, this can cause issues with mass transport of electrolytes with changes in applied potential to the working electrode, and interfere with the formation of the electric double layer. This can be solved by incorporating a flow cell design[58], which increases the complexity of an already technically difficult experiment. For those reasons, we will focus on the Kretschmann ATR configuration. In a general ATR configuration, the sample is placed on top of the ATR prism and the IR beam is passed through the prism and is totally internally reflected (TIR), as shown in Figure 2.5.

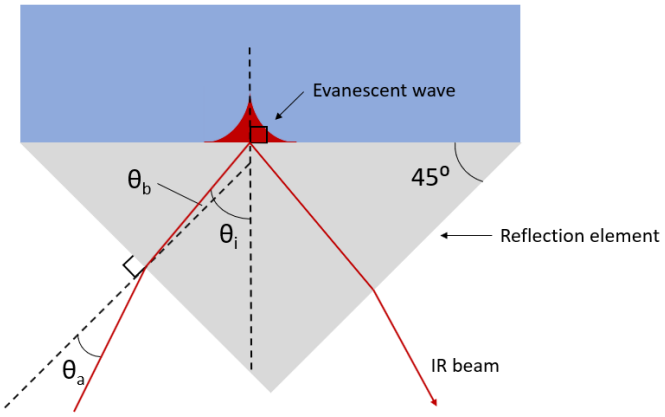

Figure 2.5: Total internal reflection of an IR beam in a prism (reflection element) with a non-normal angle of incidence θ_a on the prism face, leading to internal angle of incidence θ_i.

According to Snell's laws, this can only occur when the refractive index of the prism material, n_p, is greater than the refractive index of the sample, n_s.

$$n_p sin(\theta_i) = n_s sin(\theta_r) \tag{2.30}$$

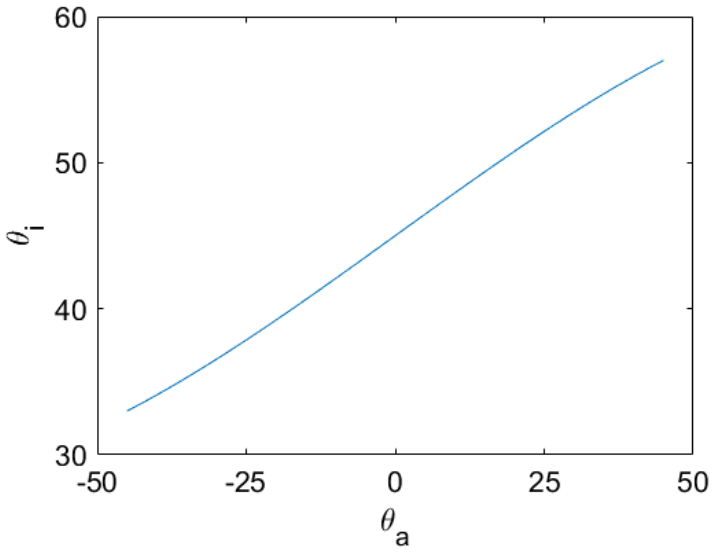

Figure 2.6: Internal AOI (θ_i) as a function of external AOI (θ_a) for a Si ATR prism with a 90°apex angle.

In this case, we can solve for the critical angle of incidence that will lead to the refracted beam angle being 90°, after which all the light will be reflected.

$$\theta_c = arcsin(\frac{n_s}{n_p}) \tag{2.31}$$

Where θ_c is the critical angle. For a Si ATR prism with a pure water sample, the critical angle turns out to be 22.74°. Of course, unless the IR beam is perfectly normal to the ATR prism face, it will be refracted and the internal angle of incidence (AOI) will defer from the AOI at the prism/sample interface, which is the one we care about for achieving TIR. This is easy to correct for using Snell's law, and Figure 2.6 shows the internal AOI, θ_i, as a function of the external AOI, θ_a (shown in Figure 2.5). We can see that for reasonable experimental AOIs, the internal AOI is always above the critical angle of 22.74°when using Si as the ATR material.

2.3.2 Reflective Losses

Another concern when designing ATR experiments is minimizing reflective losses when the light is incident on the air-prism interface. Ideally, reflective losses would be no more than 20-30%. We can estimate reflective losses from Fresnel equations for both s and p polarized light and see how it changes with incident angle and the index of refraction of the prism material.

$$R_s = \left| \frac{n_{air} cos\theta_a - n_{re}[1 - (\frac{n_{air}}{n_{re}} sin\theta_a)^2]^{\frac{1}{2}}}{n_{air} cos\theta_a + n_{re}[1 - (\frac{n_{air}}{n_{re}} sin\theta_a)^2]^{\frac{1}{2}}} \right|^2 \tag{2.32}$$

$$R_p = \left| \frac{n_{air}[1 - (\frac{n_{air}}{n_{re}} sin\theta_a)^2]^{\frac{1}{2}} - n_{re} cos\theta_a}{n_{air}[1 - (\frac{n_{air}}{n_{re}} sin\theta_a)^2]^{\frac{1}{2}} + n_{re} cos\theta_a} \right| \tag{2.33}$$

$$R_{av} = \frac{R_s + R_p}{2} \tag{2.34}$$

We can see in Figure 2.7 that reflective losses are minimized at a normal incident angle with respect to the air-prism interface. The reflective losses also increase when the refractive index of the prism increases. However, as we showed before, since we are working with aqueous solutions we still need a material with a fairly high refractive index in order to work with reasonable AOIs.

Clearly, the choice of prism material will have substantial influence on how the experiment is set up and its overall success. There are also other considerations when selecting an ATR prism material for 2D IR electrochemistry experiments, which are discussed in the next section.

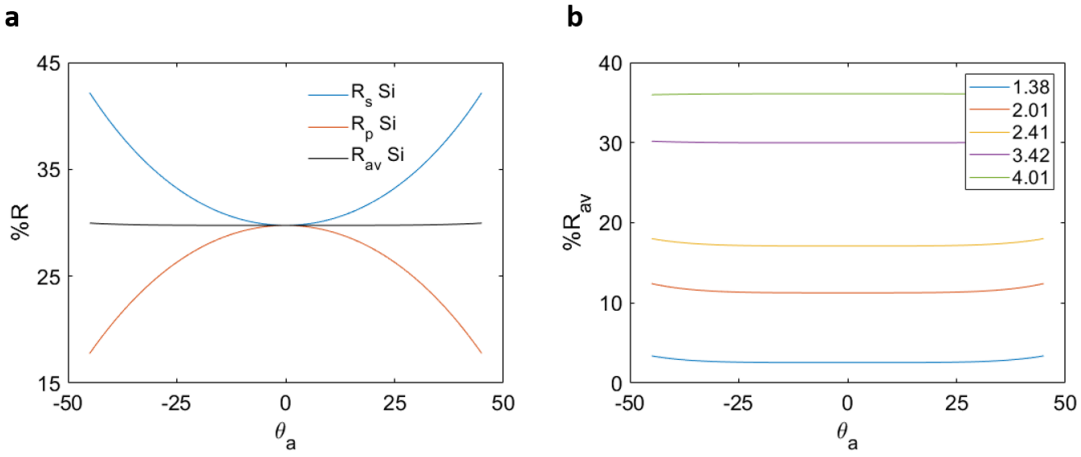

Figure 2.7: (a) Reflective losses for air-Si interface for both s (R_s) and p (R_p) polarized light, as well as the average (R_{av}), shown over the incident angle θ_a as defined in Figure 2.5. (b) Average reflective losses shown over θ_a for different prism materials with the refractive index shown in the legend.

2.3.3 ATR Materials

For linear IR, common ATR materials are shown in Table 2.1. Included in that table but which are not commonly used as an ATR materials are CaF_2 and ZrO_2. Typically, when selecting IR ATR materials, the criteria are broad transparency in the IR, a high index of refraction, and a large effective path length or penetration depth. For interfacial 2D IR, the penetration depth should not matter since we are probing monolayers in the first 1 nm from the surface. Added considerations are the chirp or temporal dispersion of the fs pulses, whether the material will have a long-lived transient responses when in the beam focus due to the multiphoton excitation of free carriers, and balancing reflective losses which may be more detrimental for signal intensities in nonlinear spectroscopic measurements. For electrochemical experiments where the conditions can degrade the electrodes from the current cycling as well as concentrated electrolyte solutions which can alter pH, the

robustness and chemical compatibility of the ATR material is also a consideration. The relevant material properties for potential ATR substrates are shown in Table 2.1.

Material	Refractive index, n	Critical angle***, °	GVD, fs^2/mm	Absorption coefficient, cm^{-1}	Hardness, Kg/mm^2	Bandgap, eV
KRS-5	2.38	34.0	34.999	0.7696 (2)	40	na
ZnSe	2.41	33.5	-82.066	0.004 (2)	120	2.70
ZnS	2.24	36.4	-439.73	0.0006 (2)	240	3.54
Ge	4.01	19.4	697.69	0.006 (2)	550	0.66
Diamond	2.38	34.0	185.52*	1.74 (1)	5700	5.47
Si	3.42	22.9	259.93	0.0356	1150	1.12
ZrO_2^{**}	2.01	41.5	-2691	0.498 (2)	1370	3.84
CaF_2	1.38	74.6	-1113	0.0035 (2)	158	11.8

Table 2.1: Material properties for potential ATR prisms at 6 um. *at 0.76 um, **at 5.135 um, n and gvd taken from refractiveindex.info. ***Critical angle calculated for each material with pure water as the sample. (1)[59] (2)[60]

Many of the materials listed are soft and can potential leach ions into solution, such as KRS-5 (also toxic), and ZnSe. Diamond, while being the most robust material, is cost inhibiting and has interfering phonon resonances across the IR region. Ge has a very small bandgap and multiphoton excitation can easily occur, leading to a long-lived transient response. It also has a very high refractive index which leads to larger reflective losses. Combining the reflective losses with the lower beam power needed to avoid the multiphoton excitation of free carriers, Ge is not an ideal option. For those reasons, the materials considered for ATR 2D IR in Chapter 5 were Si, ZrO_2, and CaF_2.

CaF_2, a material commonly used in 2D IR experiments, has a low index of refraction, limiting its use as an ATR material when working with electrolyte solutions (which have indices of refraction near that of pure water at 1.33) due to the large critical angle required for total internal reflection. This is illustrated in Figure 2.8, which shows that the critical angle increases linearly as the refractive index of the sample increases, until the refractive index of the sample nears that of the ATR prism (Si and ZrO_2 shown for comparison), where the critical angle increases steeply.

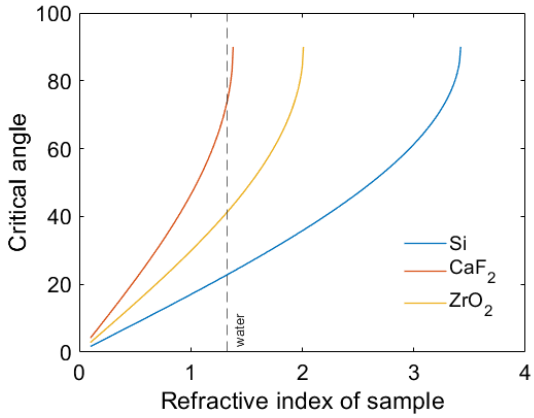

Figure 2.8: Critical angle at prism-sample interface for different refractive indices of the sample. The black line represents the refractive index of pure water at 1.33.

Being near the critical angle can lead to dispersive lineshapes in 2D IR spectra[61], which is only a concern for surface-sensitive 2D IR because the plasmon-enhanced spectra can resemble dispersive lineshapes and lead to convolution of the two effects that cannot be untangled. However, for some applications (such as when the sample refractive index is around or less than 1, or when working in transmission/external reflection geometries) CaF_2 is still a preferred substrate because of its transparency in the IR and high band gap, making it easy to work with.

Si is a common ATR material because of its robustness, and high refractive index. It has a relatively small GVD as well, but it does have a small band gap which requires attenuation of beam power for non linear measurements. However, the band gap is larger than Ge and it is possible to use without exciting a long-lived transient response. Like diamond, it does have some phonon modes infringing on the IR region from native SiO_2, but the intensity of the peaks is low since they arise from only a few nms of oxide. They also do not appear above 1650 cm^{-1}

While not a widely used optical material, ZrO_2 has many of the properties that are

necessary for a 2D IR ATR experiment. The refractive index is 2.01, which means the critical angle with an aqueous sample is 41.5°, providing plenty of space to tune the incident angle away from the critical angle. It is extremely durable, and also has a relatively large band gap of 3.84 eV. It does have a large negative GVD, but this can be compensated for with Ge. It also has a higher adsorption coefficient than most other materials listed, but is still usable and beam powers can be higher than for Si because of the higher band gap.

2.4 2D IR in Practice

2.4.1 Experimental Layout

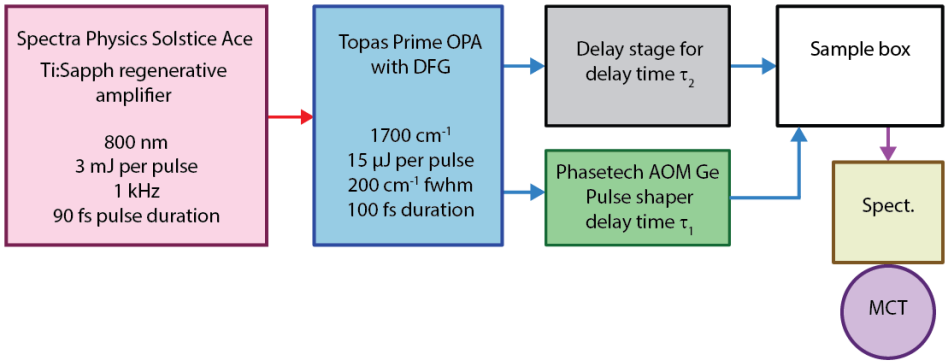

Figure 2.9: Schematic of the main components in the 2D spectrometer.

In this section an overview of the components and general principles of the 2D spectrometer are described. In practice, measuring a 2D IR spectrum requires intense mid-IR pulses that are spectrally broad and temporally short. This starts with the generation of broad bandwidth 800 nm pulses generated in a commercial mode-locked oscillator with mJ pulse energies, with repetition rate of 1 kHz and 90 fs pulse duration.

The 800 nm pulses are then sent into a commercial optical parametric amplifier (OPA) that is equipped with non-collinear difference frequency generation (NDFG). The OPA outputs two frequencies called the signal and idler, and the frequency of the signal and idler determines the NDFG output frequency, providing IR pulses that are tunable across a large range in the mid-IR and have approximately 200 cm^{-1} bandwidth (depending on the tuned frequency). After NDFG, a CaF_2 wedge picks off a small portion of the mid-IR pulse (probe, E_3) and sends it through a delay stage to generate τ_2 waiting times. The rest of the pulse (pump, E_1 and E_2) is sent through a pulse shaper that generates two pump pulses with controllable time delay τ_1, and phase control.

The pump and probe pulses are then sent into the sample box where they are focused and overlapped in the sample. The probe (which is collinear with the signal) is then sent into a spectrograph which spreads the pulse out in frequency and is detected by an MCT array detector, so that the detection axis is measured in the frequency domain.

Generation and amplification of 800 nm pulses

The 800 nm pulses are generated and amplified in a Spectra Physics Solstice laser system. The first step is the generation of an 800 nm seed pulse, which is generated by pumping Ti:Sapph in a mode-locked cavity with a 532 green laser (MaiTai SP). The output from the MaiTai is 700 mW with a 13 nm bandwidth and 80 MHz rep rate. The seed pulses from the MaiTai are then stretched before combined with a pump pulse in a regenerative amplifier where they are amplified in another Ti:Sapph crystal. The pump pulse comes from a Millenia eV green laser with a 527 nm output, 5 W of power, at a 1 kHz rep rate. Pockels cells are used to control the entrance and exit of the seed and amplified pulses in to the regenerative amplifier cavity. The timing of the cells can be adjusted to control the

number of round trips in the cavity, and are synced to the 1 kHz rep rate of the Millenia. After exiting the cavity, the pulses are re-compressed and the final output of the Solstice is approximately 3 W of power with 1 kHz rep rate, with pulse duration of 90 fs that are peaked around 800 nm.

Generation of mid-IR pulses

After the generation of the 800 nm pulses, they are sent through a TOPAS optical parametric amplifier (OPA). The pulses are first split into a "pump" which takes about 80% of the pulse energy, and the rest is used to generate a "seed" pulse. To generate the seed pulse, the beam split off from the pump is further split into a second pump, and the other part is focused into a sapphire plate to generate a white light continuum (WLC). The WLC is then amplified by combining noncollinearly with the second pump in a nonlinear beta barium borate (BBO) crystal. The desired wavelength is then picked off and used as the signal in a second amplifier stage in a second BBO where it is amplified by the bulk of the incoming 800 nm pulse that was split off in the first step, and the idler is also generated. The signal and idler output can be tuned by tuning the angles of the BBO which modifies the phase-matching condition. For the TOPAS OPA, this tuning range is 1160-1600 nm for the signal and 1600-2600 nm for the idler.

To reach the mid-IR, a second nonlinear process, NDFG, is used to generate the difference frequency between the signal and idler. This is done by combining them in a noncollinear geometry in another nonlinear crystal ($AgGaS_2$). The output from the TOPAS OPA and NDFG combo is mid-IR pulses tunable from 2600-11000 nm (900-3800 cm^{-1}). The pulses used in this thesis where generally centered near 1650 cm^{-1} with a pulse width of 200 cm^{-1}.

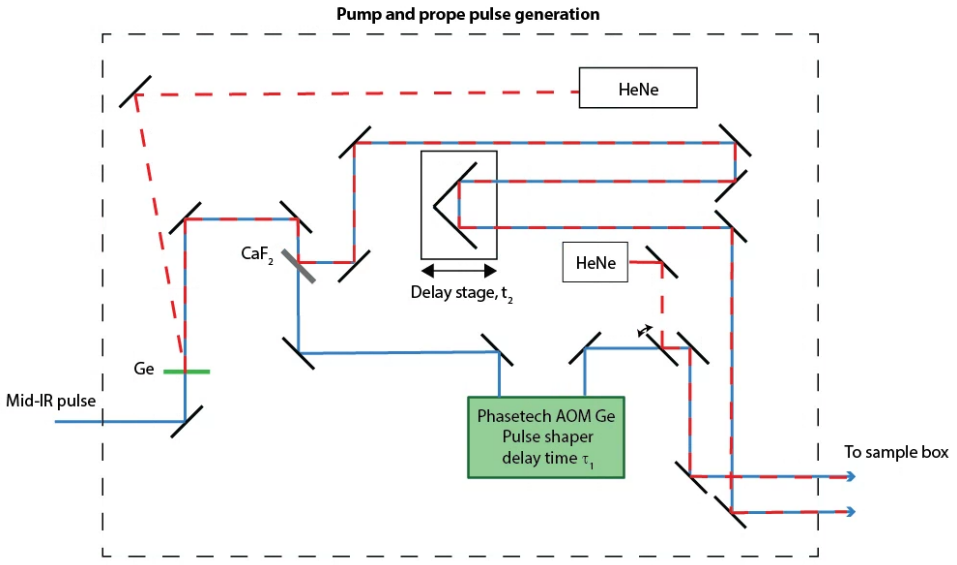

Figure 2.10: Schematic showing how the generated mid-IR pulse is split into a probe beam that is sent to a delay stage to generate τ_2 timing, and the pump which is sent through a pulse shaper to generate two pump pulses. HeNe lasers are aligning collinear with the IR beams to provide alignment guides.

IR pulse shaping and phase cycling

Once a mid-IR pulse is generated, a small section is reflected off a CaF_2 wedge and sent to a delay stage to act as the probe pulse in our experiment. The rest of the pulse is sent through an acousto-optic modulator (AOM) Germanium (Ge) pulse shaper (PhaseTech) that generates two pump pulses with controllable time delay and phase (illustrated in Figure 2.10). The Ge crystal acts as a diffraction grating when an RF signal (mask) is applied, and by applying two different masks with controlled time delay, two different pulses with independent phase can be generated.

The pulse shaper is also used to compensate for any temporal distortion in the pump pulses, up to the 6th order. For the data collected in this thesis, the pulse shaper is also used to generate a 2x2 or 2x4 phase cycling scheme. Phase cycling consists of varying the

phases of the pump pulses to reduce background noise and enhance signal, since scattered light should not have a sign dependence on the phase of the pump or probe beams, but with each π phase shift, the signal field will acquire a negative sign.[62]
An example 2x2 phase cycling scheme consists of varying the phase between the pump pulses in two discrete steps between 0 and π. This results in four phase combinations.

$$(\phi_1, \phi_2) = (0,0), (0,\pi), (\pi,0), (\pi,\pi) \tag{2.35}$$

When the phases are the same (0,0) and (π,π), the signal will a positive sign, however for different phases the signal will be negative. By subtracting the appropriate signals, the overall signal will be doubled while scatter will be suppressed since the sign will not depend on the relative phase like the signal does.

$$S_{2x2} = S(0,0) + S(\pi,\pi) - S(0,\pi) - S(\pi,0) \tag{2.36}$$

The other phase cycling scheme used to collect data in this thesis is the 2x4 phase cycling scheme. This iterates over multiple phases in between 0 and π such that there are eight combinations.

$$(\phi_1, \phi_2) = (0,0), (0,\frac{1}{3}\pi), (\frac{1}{3}\pi,0), (0,\frac{2}{3}\pi), (\frac{2}{3}\pi,0), (0,\pi), (\pi,0), (\pi,\pi) \tag{2.37}$$

2.4.2 Data Collection and Processing

To collect a spectrum, the pump and probe pulses are focused and overlapped in the sample using a pair of parabolics in either transmission or ATR geometry, as illustrated in Figure 2.11. After going through the sample, the pump pulses are blocked by an iris to

reduce artifacts coming from the pump. The signal and probe pulse (that additionally acts as the local oscillator) are sent through a Horiba spectrograph and the resulting pulse is spread out in frequency and detected on a 64-array MCT detector. The probe spectrum is collected every other shot and subtracted from the pump + probe spectrum to isolate the signal.

As mentioned in the last section, the pulse shaper is used to generate a controllable τ_1 delay time between the two pump pulses. The excitation frequency axis, ω_1, is collected in the time domain by scanning over τ_1 and Fourier transformed to provide the frequency axis at each τ_2 waiting time.

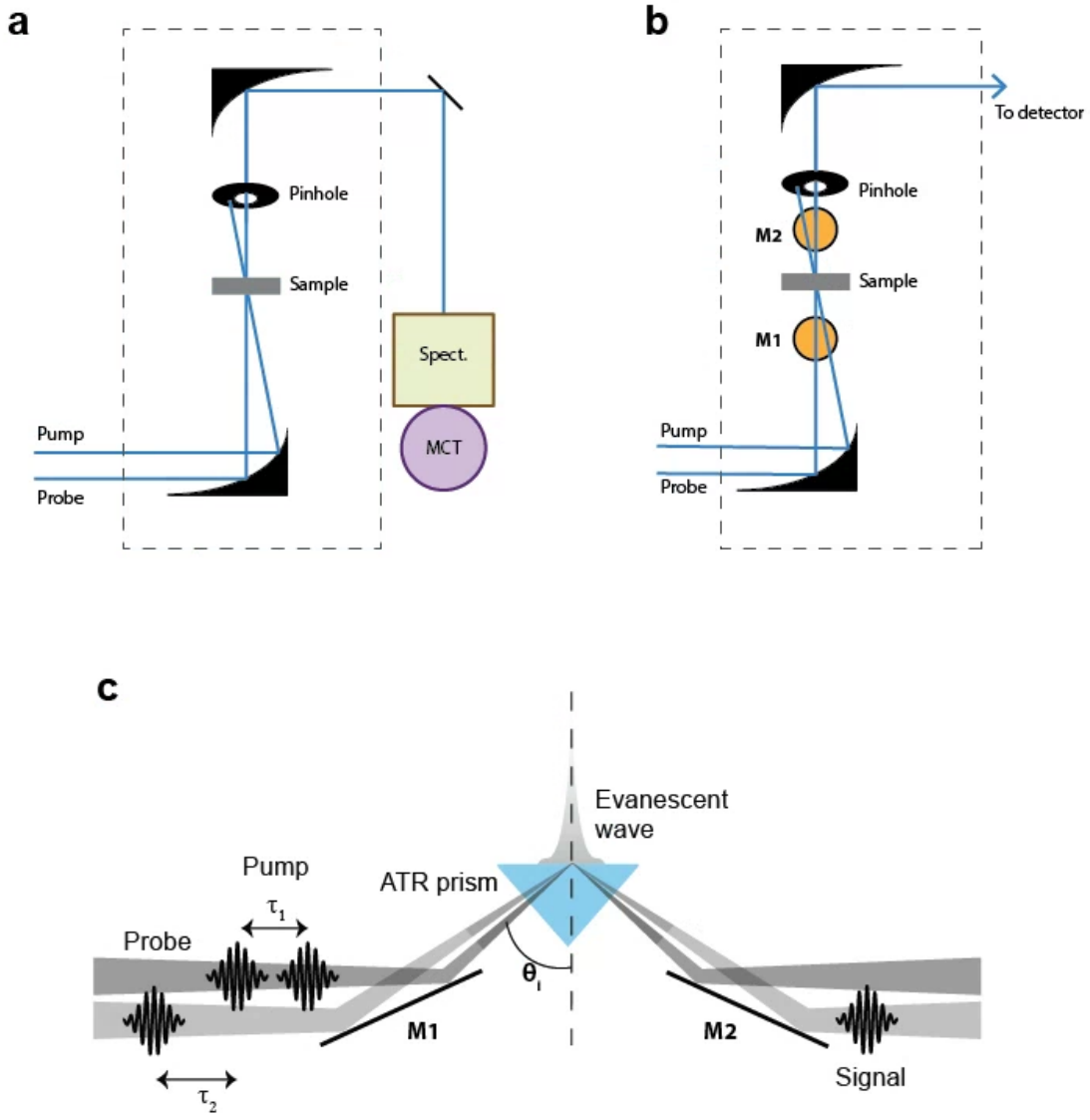

Figure 2.11: Schematic showing both the (a) transmission geometry and (b) ATR geometry from a top-down view. (c) shows the ATR geometry from a side view, demonstrating the angle of incidence θ_i.

Chapter 3

Vibrational Probes in Aqueous Solution

3.1 Introduction

An integral part of surface sensitivity in IR experiments is the use of vibrational probe reporters that are sensitive and localized to the changes being studied. For example, the vibrational modes can change because the molecule itself is part of a reaction, or they can be sensitive to changes in the local environment even though they do not directly interact with the system of interest.[63–65] Both cases require an understanding of the relationship between the changes in the vibrational probes and the changes in the system. There has been a lot of previous work that has explored vibrational modes and their usefulness as reporters, as well as understanding the origin of the vibrational changes with changes in external environment such as solvent and electric field.[13,66–68]

Vibrational electrochromism can be used to model a vibrational probe's frequency shift, where perturbation theory is used to describe the interaction between the local environment and the probe. The results from first-order perturbation theory are a linear equation that predicts that the change in frequency of a probe is dependent on the local electric field and the transition dipole moment of the vibrational probe.[13]

$$\Delta\nu = \nu_o - \Delta\mu \cdot F_{ons} \tag{3.1}$$

The local electric field can be modeled using the Onsager reaction field.[14] This models the space outside of a sphere determined by the molecular radius as a continuum based on the dielectric constant of the solution. The magnitude of the field felt by any given vibrational mode will be dependent on the magnitude of the transition dipole moment of the vibration, also called the electrochromatic tuning rate. Taken for an isotropic solution, the Onsager field, F_{ons} is shown in Equation 3.2.

$$F_{ons} = \frac{2\Delta\mu}{4\pi\varepsilon_o a^3}\frac{(\varepsilon - 1)}{(2\varepsilon + 1)} \tag{3.2}$$

The resulting Onsager field and relevant parameters are illustrated in Figure 3.1 for the two vibrational probes that will be investigated in this chapter, acetone and dimethyl ammonium, shown in a and b, respectively. Boxer et. al. and others have shown that this works reasonably well for vibrational probes such as carbonyls in different solvents, although in comparison to AMOEBA simulations the Onsager field is shown to underestimate the field imparted from the solvent, especially in the case of water. It is also important to note that the molecular dipoles are shown rather than the normal mode dipoles. For acetone, the carbonyl mode dipole is aligned with the molecular dipole, but it is important to recognize that the normal mode dipoles of the DMA^+ are perpendicular to the molecular dipole. Onsager predicts that as the dielectric decreases we will see a decrease in the field and a redshift in comparison to pure water.[14]

We have previously looked at the different contributions to the field imparted on the carbonyl bond of acetone, and found that the calculated field from MD simulations was

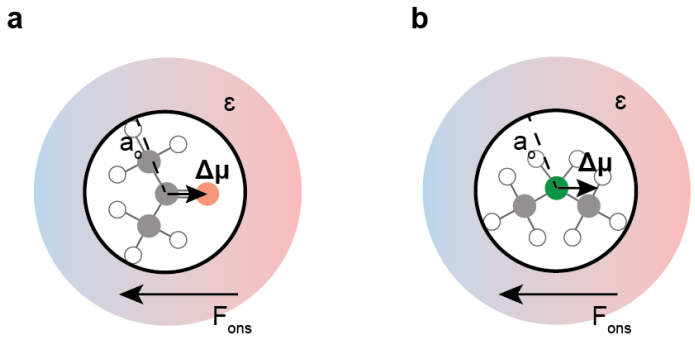

Figure 3.1: Onsager model for (a) acetone and (b) dimethyl ammonium in a dielectric medium with index of refraction ϵ, transition dipole $\Delta\mu$, and induced field F_{ons}.

insufficient to account for specific ion effects.[3] Instead, the important contributors when looking at molecular dynamics simulations of different chloride salts was the field imparted when a cation was in the first solvation shell of acetone (which increases with increasing charge density or polarizing capability of the cation) and the solvent organization around the cation which in some cases organized the solvent at the expense of the carbonyl leading to a change in the sign of the field and unexpected shifts. The second contributor leads to a discussion on the changing nature of the hydrogen bond (HB) network around the probe. Tightly bound cation solvation shells create stronger HB donors of the water in the solvation shell. However, it also imparts more structure on the surrounding water which as mentioned previously can lead to a change in the sign of the field around the probe. Overall, the molecular details of the system and orientations of the solvent, probe, and electrolyte were needed to describe the observed solvatochromism. In this chapter, we look at vibrational probes that are either HB acceptors or donators in a variety of electrolyte solutions, including the CNC asymmetric stretch and CH_3 bend of dimethyl ammonium (DMA^+), the carbonyl stretch of 3-mercapto-2-butanone (MCB), and the carbonyl stretch of acetone. We observe again that continuum models are not sufficient to describe

vibrational shifts, and the ion identity plays a key role. We show that even positively charged probes like DMA^+ are sensitive to same-charge ions. However, further MD work is required to understand the molecular reason behind the observed specific ion effects, and the results in this chapter should be used as a guide when selecting an appropriate vibrational probe for a specific system.

3.2 Methods

We evaluated the sensitivity of four different molecules and five different vibrational modes to aqueous electrolyte conditions that varied in both concentration and ion identity. 3-mercapto-2-butanone (MCB), acetone, dimethyl ammonium chloride, and salts used were purchased from Sigma-Aldrich and used as received. D_2O (99.9%) was purchased from Cambridge Isotope Laboratories. MCB and acetone solutions were made with D_2O, while DMA^+ solutions were made in H_2O.

FTIR spectra were taken in transmission mode on a Bruker Tensor 27 spectrometer. Transmission cell windows for FTIR were 25 mm $\varnothing \times 1$ mm thick CaF_2 windows (Crystran), with a 50 μm Teflon spacer. Spectra of salt solutions without the probe molecules were taken and used to subtract off the D_2O spectrum.

3.3 Results and Discussion

3.3.1 Vibrational shift with concentration

To investigate the relationship between the vibrational probe used and specific ion effects, we looked at several vibrational probes in 16 different salt solutions at a range of

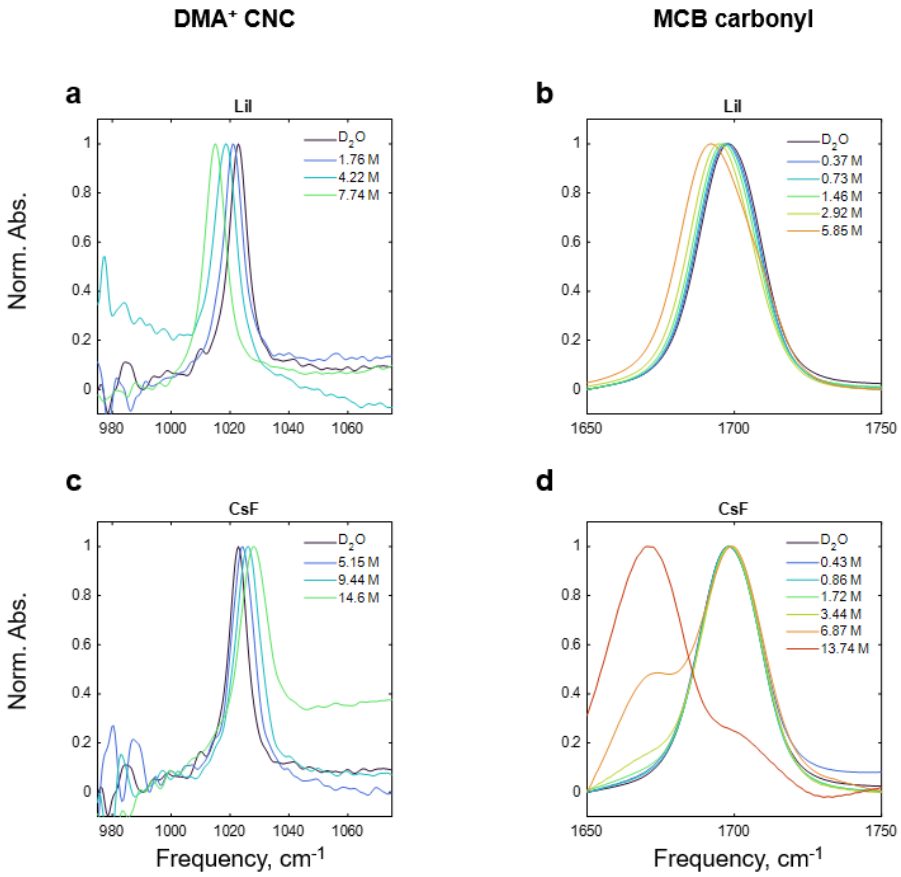

Figure 3.2: Example FTIR spectra background subtracted with the corresponding solutions spectra. Each spectrum is normalized to the maximum of the observed vibrational mode. Solutions shown are LiI at multiple concentrations, including pure D_2O, with (a) DMA^+ and (b) MCB, and CsF at multiple concentrations, for (c) DMA^+ and (d) MCB.

concentrations. We chose all available and soluble monovalent salts to look at both cation and anion effects. The resulting FTIR spectra of each probe for every condition was background subtracted by taking the corresponding solution spectra without the probe. The FTIR of the MCB carbonyl and DMA^+ CNC asymmetric stretch are shown in Figure 3.2.

LiI was chosen to show a case where there is a large, linear response to the salt

concentration.For DMA^+, we see that in LiI, the peak shifts clearly with little change in the peak width. MCB carbonyl in LiI also shows larger peak shifts than in other salts. CsF was chosen to show the more interesting behaivor of MCB and DMA^+, where there is a large blushift in DMA^+, and an interesting peak that grows in for the MCB case with higher CsF concentrations that is not seen in the acetone case (see Figure A.1). We only see this behavior for fluoride salts, and attribute it to an interaction between the fluoride anion and the thiol group of MCB. Thiol groups are known hydrogen bond donors[69], which could lead to attractive electrostatic interactions between the thiol and negatively charged fluoride anion.

For the peak maximum, the peaks were fit with a Gaussian accurately determine the peak frequency, and the maximum of the Gaussian fit is plotted as a function of salt concentration. The results are shown in Figure 3.3, where we can see that the vibrational shift DMA^+ displays is organized first by anion identity (designated by color), and then to a lesser extent cation identity (designated by marker shape). Acetone shows a dependence on both, but is organized by the cation identity more so than the anion. This preference towards anion or cation identity is expected due to the positive charge on the DMA^+ and the partial negative charge on the carbonyl oxygen creating a stronger likelihood of carbonyl-cation interaction and DMA^+-anion interaction in solution. This highlights the influence of the probe molecule choice on the sensitivity to various different factors, here the anion or cation, but also can provide guidance on the correct selection of a vibrational probe depending on the problem at hand. Later in this chapter we will analyze the relative slopes to quantify the sensitivity of each probe to either anion or cation identity.

The vibrational shift is also linear in concentration, which already deviates from the behavior predicted by using the Onsager field in Equation 3.1. We can show this clearly by

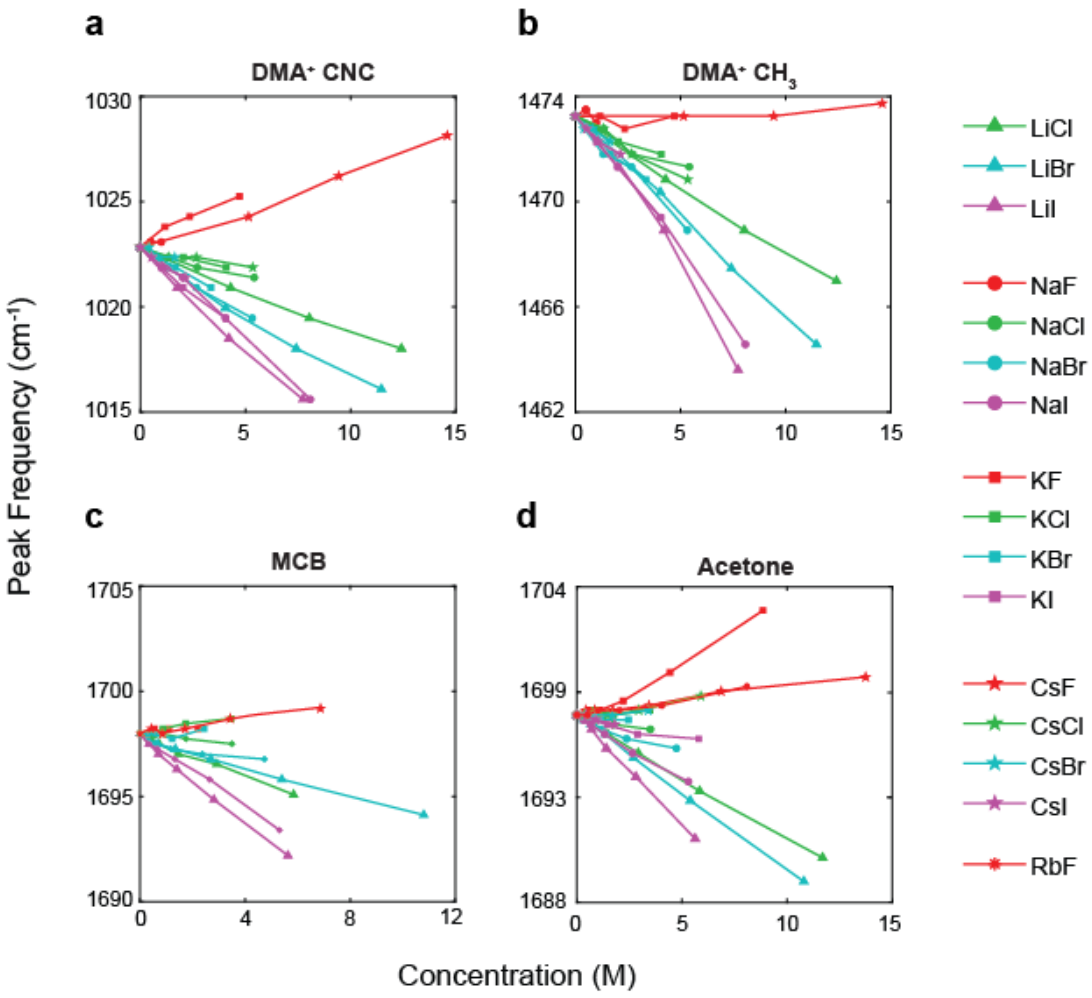

Figure 3.3: Frequency of peak maximum from Gaussian fit plotted for all probes against concentration, including (a) DMA^+ CNC asymmetric stretch, (b) DMA^+ CH_3 bending, (c) MCB carbonyl stretch, and (d) acetone carbonyl stretch. Anions are differentiated by different colors, and cations are differentiated by different marker shapes as shown in the figure legend.

calculating the Onsager field with Equation 3.2 for each salt solution as a function of concentration. For the dielectric constant we use a numerical model shown to have excellent agreement with experimental measurements to extrapolate the dielectric at a given concentration of salt.[70] In order to predict a linear frequency shift, the Onsager field

should also be linear with concentration. However, we see in Figure 3.4 that at higher salt concentrations the Onsager field is non-linear even through we see a linear shift with concentration in the experimental data.

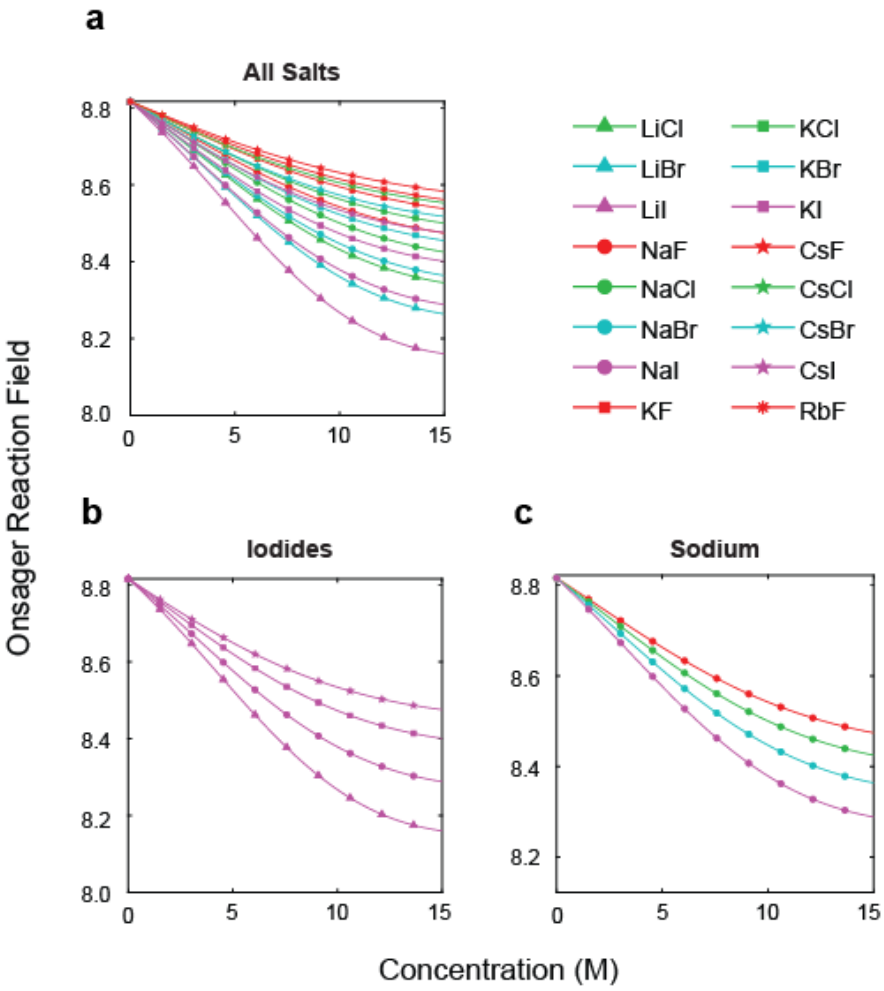

Figure 3.4: F_{ons} calculated for (a) all salts from the calculated dielectric constants. (b) Only iodide salts and (b) only sodium salts are plotted to illustrate the specific effect of cations and anions.

There are some similarities between the calculated Onsager field and the amount of frequency shifting seen in the vibrational probes. The calculated Onsager field follows the

same general trend seen for the vibrational shift of the probes, where for a given cation the anion determines the magnitude of the shift, with fluorides leading to the smallest change in field and iodides contributing to the largest. To emphasize the effect of anion and cation on the calculated Onsager field, Figure 3.2 b and c show the field for all the iodide salts (changing cation) and all the sodium salts (changing anion). If we now look at how the cations change an anion response, we see that there is larger field change for an anion paired with Li^+, and the field changes less as we increase the cation size. An example is for lithium salts, the difference between LiCl and LiI is greater than the difference between CsCl and CsI. So for increasing anion size we see a larger change in field, while the opposite is true for the cation size. Despite the general trend being followed, the discrepancies in the order of which salts cause the largest shifts point towards specific interactions between the probe vibration and the solvent that are due to more that just the average solvent electric field.

To further analyze the correlation between the calculated Onsager field and the vibrational frequency, we can look at the experimental frequency shifts against the Onsager field in Figure 3.5. Overall, the ion dependence seems to be slightly less than when plotted against concentration, but there is clearly still a strong ion dependence. The fact that we can see a stronger dependence of vibrational shifts on either the cation or anion identity when the change in electric field of the solvent is accounted for reinforces the need for a better description of the forces acting on a probe when looking at vibrational shifts in electrolyte solutions.

The most striking difference between the experimental and predicted data is the blueshift that occurs for DMA^+ CNC asymmetric stretch in the presence of Fluoride salts and for acetone in the presence of Fluorides and some Cesium salts. The positive change in

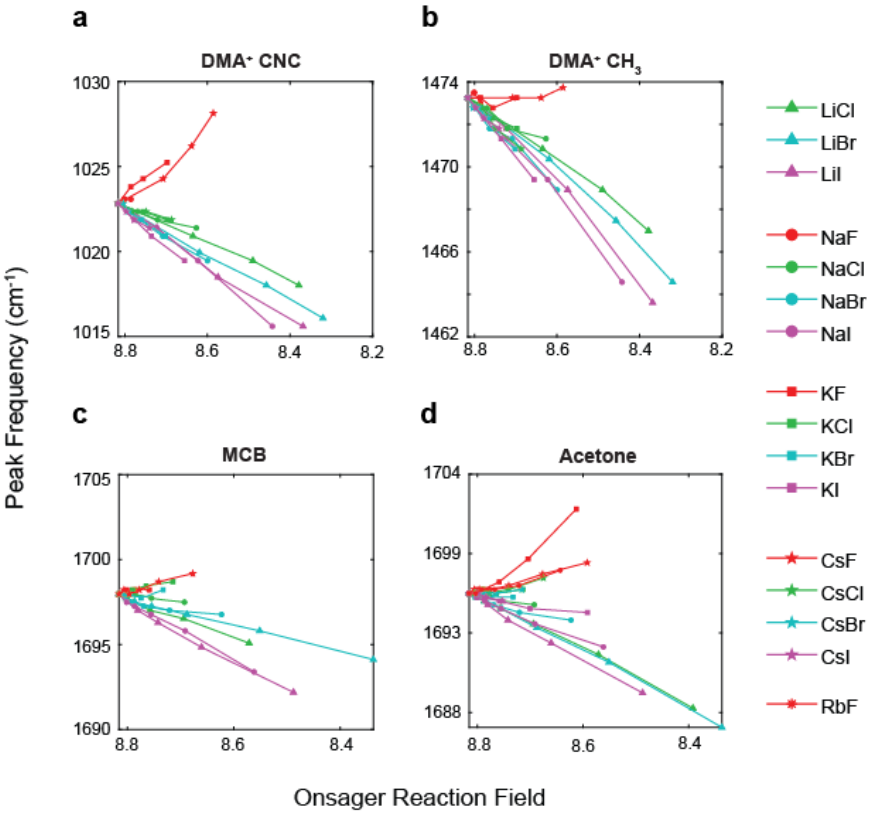

Figure 3.5: Comparison of max frequency to field calculated at that concentration for (a) DMA^+ CNC asymmetric stretch, (b) DMA^+ CH_3 bend, (c) MCB carbonyl stretch, and (d) acetone carbonyl stretch.

frequency with decrease of the average solvent field goes against the prediction made by Equation 3.1, where for aqueous electrolyte solutions the Onsager field only decreases, predicting only redshifting of the frequencies.

3.3.2 Accounting for ionic properties

Although using the Onsager field leads to a slightly better correlation than salt concentration, it does not fully capture the specific ion effects we observe. Ignoring the

salts that cause blueshifts for a moment, we can look at how well the Onsager field describes just the salts that redshift as the dielectric decrement would predict. What we observe is that while the Onsager field is a better descriptor than concentration, it still doesn't remove the ion specificity and in no way captures the blueshifts or competing effects from the different ions, as we saw in the last section in Figure 3.5. This result is not surprising as the Onsager field models the solvent as a continuum and doesn't include the effects of changes in hydrogen bonding environment, polarization of the molecule when in direct contact with ions, or potential charge transfer.

The approach we will take now will use specific ion properties to try and collapse the different slopes for vibrational shift with concentration. We can do this by scaling the concentration by select ion properties to try and determine which ones are important for each probe. The first scaling we use is the anion polarizability for aqueous anions from Li et. al.[71] The polarizability of the anion is a measure of how easily the electron density is distorted. The easier this is, the more likely the anion is to cause other effects such as dipole induced dipoles. Cations on the other hand generally are not very polarizable and thus the polarizability is not a good measure of their specific effects. When looking at the cation polarizability scaled frequency shifts, there was little to no change in the trends seen for any of the probe vibrations. However, as shown in Figure 3.6, when scaling by anion polarizability the slopes for both DMA^+ in all salts (besides the ones that cause blueshifts) fall onto the same line with R^2 values of 0.97 for the CNC asymmetric stretch and 0.98 for the CH_3 bending. This implies that the specific ion effects on the vibrational frequency originate from the anion polarizability.

If we use the same anion polarizability to scale the concentration for our carbonyl probes, there is much less of an effect. For MCB, the R^2 goes from 0.59 to 0.77, but for acetone it

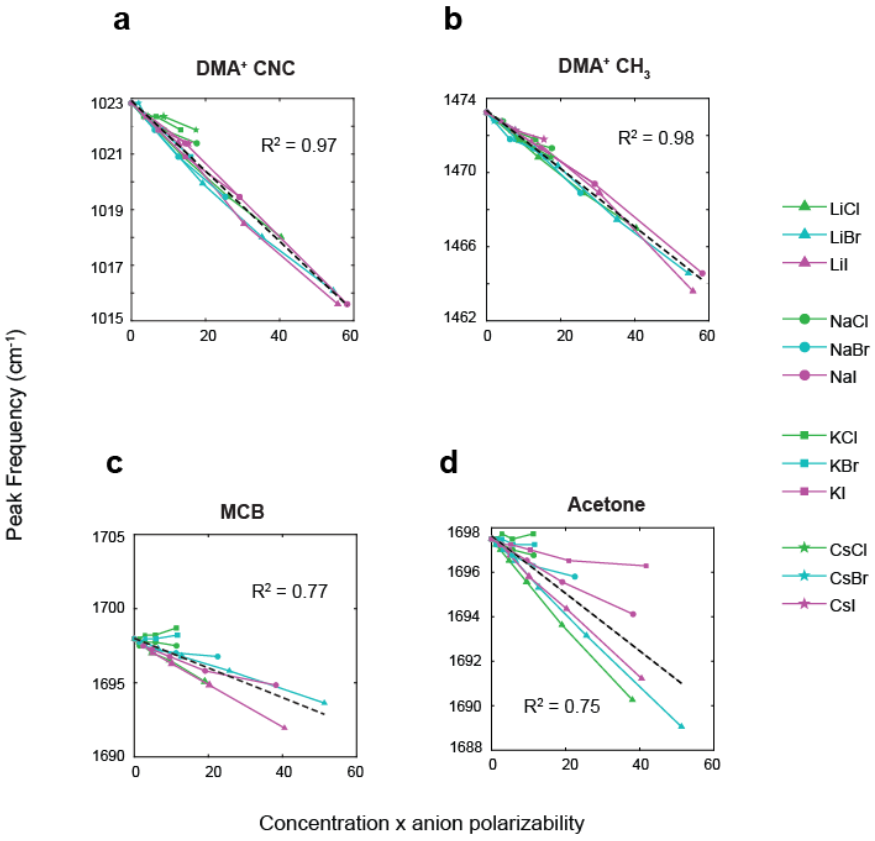

Figure 3.6: Vibrational frequency shifts plotted against the molar concentration multiplied by the anion polarizability, and then fit with a linear fit for (a) DMA^+ CNC asymmetric stretch, (b) DMA^+ CH_3 bending, (c) Acetone carbonyl stretch, and (d) MCB carbonyl stretch.

actually decreases from 0.81 to 0.75 when we account for anion polarizability. The improvement for MCB can be explained by the thiol group that can potentially interact with the anion, leading to an increased sensitivity to anion identity.

Next we want to look at the coulumbic contribution to the field the carbonyls will feel from the cation. If we assume the simple picture of the cations approaching the carbonyl from the same angle, we can approximate the contribution as proportional to the square inverse cation radius. However, we also need to take into account that the coulumbic force will be

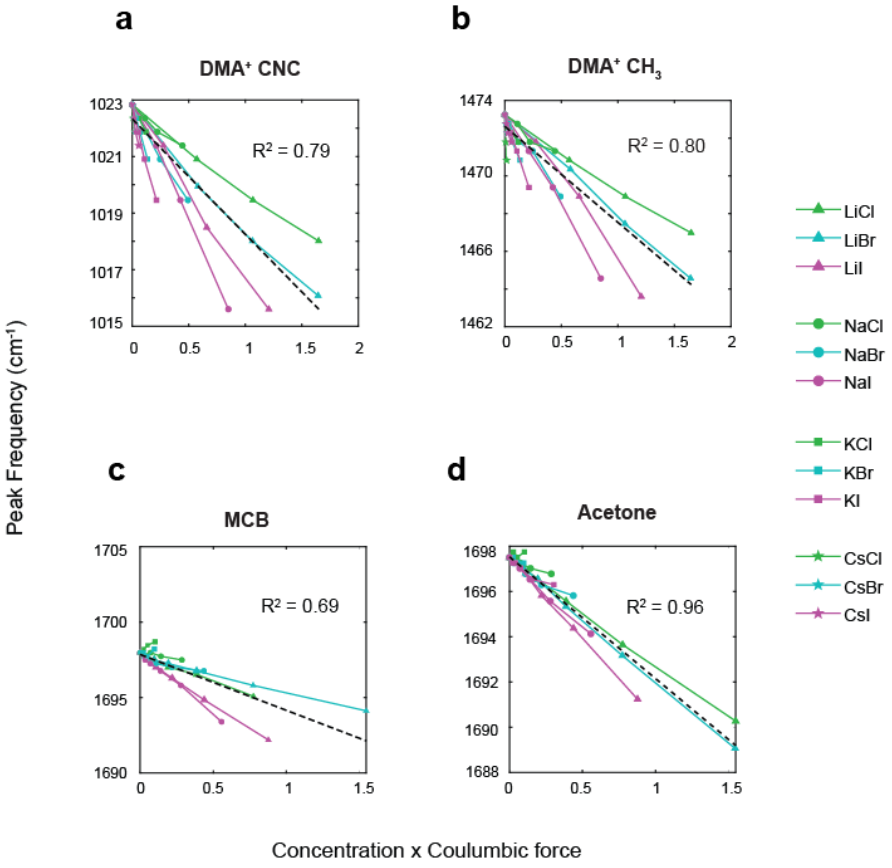

Figure 3.7: Vibrational frequency shifts plotted against the molar concentration multiplied by the Coulumbic force (Equation 3.3, and then fit with a linear fit for (a) DMA^+ CNC asymmetric stretch, (b) DMA^+ CH_3 bending, (c) Acetone carbonyl stretch, and (d) MCB carbonyl stretch.

dampened by the anion present, leading to the scaling factor in Equation 3.3.

$$F_c \propto \frac{1}{r_{cat}^2} - \frac{1}{r_{an}^2} \tag{3.3}$$

The results are shown in Figure 3.7. For DMA^+, this scaling has almost no effect on the distribution of slopes. For MCB there is a slight improvement from R^2 0.59 to 0.69. Acetone has the best improvement, with an R^2 of 0.96. The difference between acetone and

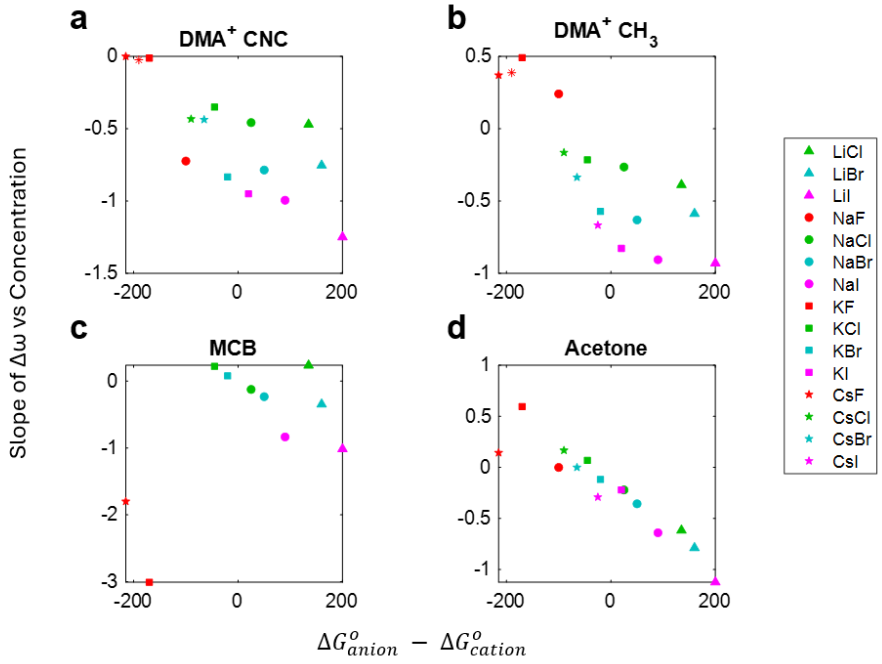

Figure 3.8: Visualizing the spread of slopes against the difference in Gibbs free energy of hydration (ΔG_i^o) between ions, where the slope is of $\Delta\omega$ vs Concentration (Molar) for each probe/salt. (a) DMA^+ CNC asymmetric stretch, (b) DMA^+ CH_3 bending, (c) Acetone carbonyl stretch, and (d) MCB carbonyl stretch.

MCB can again be explained by the presence of the thiol group and potential anion interactions that place it somewhere in the middle of acetone and DMA^+ in terms of sensitivity to anion or cation. In order to test these hypothesis, further work will need to be to model the probes in solution with molecular dynamics in order to relate the microscopic structure to the ion dependent macroscopic observables. However, that work is not presented in this thesis and is instead a ongoing future study.

Additionally, we can look at the Gibbs free energy of hydration of the ions in water, which depends on the specific solvation environment and the energy required to make a cavity in the solvent. The values used for Gibbs free energy of solvation were determined empirically[72] by looking at the dissolution of salts.

$$BA(s) \rightarrow B^{+}(aq) + A^{-}(aq) \tag{3.4}$$

Where B is the cation (Li, Na, K, or Cs) and A is the anion (F, Cl, Br, or I). Different methods were used to measure the enthalpy and entropy and calculate the resulting Gibbs free energy of hydration.

$$\Delta G^{0}_{hyd} = \Delta H^{0}_{hyd} - T\Delta S^{0} \tag{3.5}$$

Where the above equation shows the general relationship between the Gibbs free energy, enthalpy, and entropy. Ion pairing is most likely between ions that have similar hydration free energies, so with increased difference should see an increase in the effect on the probe, which is roughly seen Figure 3.8, where the zero difference between the hydration free energy of the ions is close to the zero slope of the frequency shift, $\Delta\omega$, with concentration. The Gibbs free energy of hydration description also aligns the blue-shifted slopes with the red-shifted ones, with the exception of MCB. In DMA^{+} there is still a lot of spread in the slopes indicating that this is still not a good description for the DMA^{+} probe. However, the Gibbs free energy of hydration appears to correct for most of the specific ion effects seen in acetone.

3.3.3 Quantifying anion and cation sensitivity

There is clearly different levels of cation vs anion sensitivity in the different probes presented in this chapter. In this section we will attempt to quantify the difference in sensitivity. To compare the sensitivity of a probe to the anion and cation identity, we

looked at the spread of $\Delta\omega$ vs concentration slopes for a single anion identity for all the cations, as shown in Figure 3.9.

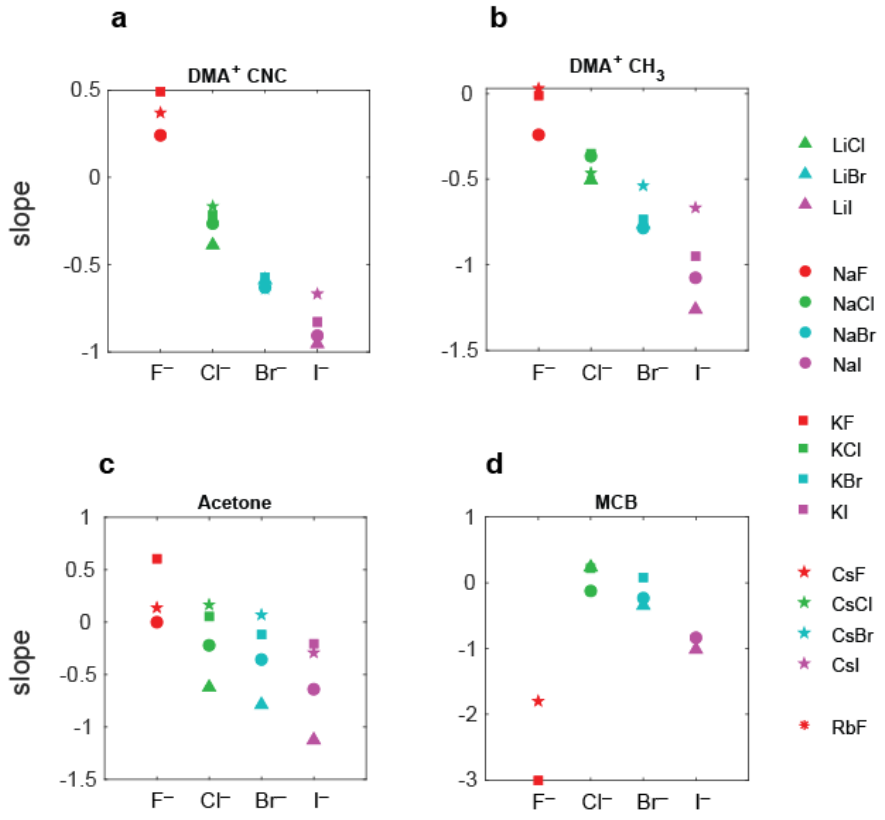

Figure 3.9: Visualizing the spread of slopes for a specific anion, where the slope is of $\Delta\omega$ vs Concentration (Molar) for each probe/salt. (a) DMA^+ CNC asymmetric stretch, (b) DMA^+ CH_3 bending, (c) Acetone carbonyl stretch, and (d) MCB carbonyl stretch.

Here we can see more clearly see the trends from the anion (changes in the slope across the x-axis) separated from the cation trends (spread along y-axis at a single anion point). With this presentation, it is also clear that the anion has a more systematic effect on DMA^+ and acetone, where the slope is always decreasing from F<Cl<Br<I, where the exception is MCB in fluoride salts. In contrast, the cation seems to be less organized except for the case of acetone, where the order of slope decreases is (Cs or K)<Na<Li.

This could be due to more specific interactions between acetone and cations, as opposed to DMA^+ which only exhibits this trend for iodide salts, or MCB which does not show any trend with cation identity.

Next we can quantify the sensitivity overall of the probes to either the cation or anion. In Table 3.1, we introduce a new quantifier, the A/C ration, where for values > 1 the probe is more sensitive to the anion, and for values < 1 it is more sensitive to the cation. We calculate this by looking first at how the cation changes the slope of $\Delta\omega$ vs concentration for a single anion. The difference in the slopes for each anion as a function of the cation is averaged, and used as the cation value in the A/C ratio. The same is done for the anions, by looking at how the anion identity affects the slope for a single cation, and the averaged values are used as the anion value.

$$\frac{A}{C} = \frac{(\sum_a^{N_a} \Delta slope_{a,c})/N_a}{(\sum_c^{N_c} \Delta slope_{c,a})/N_c} \tag{3.6}$$

Where c is the cation identity and a is the anion identity. $N_{a/c}$ is the total number of different anions or cations for a single cation or anion. The value $\Delta slope$ is described by the average difference in slopes when looking changing either cation or anion identity.

$$\Delta slope_{a,c} = \sum_a^{N_a} |max(slopes_{a,c}) - min(slopes_{a,c})|/N_a \tag{3.7}$$

$$\Delta slope_{c,a} = \sum_c^{N_c} |max(slopes_{c,a}) - min(slopes_{c,a})|/N_c \tag{3.8}$$

Where the absolute difference between the slopes for a specific anion or cation is averaged over the total number of anions (for the anion dependence) or cations (for the cation dependence).

Table 3.1: Anion to cation ratios for various vibrational probes.

Probe	Anion	Cation	A/C Ratio
MCB	0.2590	0.1963	1.319
Acetone	0.4100	0.6930	0.5916
DMA^+ CNC	0.8385	0.4951	1.694
DMA^+ CH_3	0.9886	0.6382	1.549

As expected, DMA^+ shows much greater sensitivity to the anion identity, and the CNC asymmetric stretch is slightly more sensitive that the CH_3 bend with A/C ratios of 1.694 and 1.549, respectively. Surprisingly, MCB is also more sensitive to the anion identity (1.319), while acetone is more sensitive to cation (0.5916).

Not only do these results imply that selection of probes is important when considering what you want to be sensitive to, but the sensitivity to specific ion identities also implies that there are molecular level interactions that cannot be accounted for with just the electric field.

3.4 Conclusion

In this chapter we looked at DMA^+, MCB, and acetone as ideal vibrational reporters in aqueous electrolyte solutions. What we found was that a continuum description of the solvent electric field was insufficient to account for specific ion effects, as demonstrated by looking at several different electrolyte solutions and observing ion dependent shifts even after calculating the Onsager reaction field for each solution. To remove the specific ion dependence, we had to factor in specific ion properties such as polarizability and screening effects for each salt. Interestingly, different ion properties worked for each vibrational probe, with anion polarizability being most important for DMA^+, the combined Coulumbic potential being most important for acetone, and MCB being only slightly improved by

either, suggesting more complex interactions with both cations and anions in solution due to having both HB donating and receiving groups. We also quantified the sensitivity of each probes' vibrational mode to both the cation and anion identity by looking at how widely the frequency slope changed for either just anion or just cation changes. What we found was that as expected, DMA^+ was more sensitive to anions in solution, acetone was more sensitive to cations, and MCB was slightly more sensitive to anions. We believe that our results demonstrate the importance of considering specific ion effects for even well-behaved vibrational probes such as acetone's carbonyl stretch.

Chapter 4

Plasmonic Enhancement in the IR

4.1 Introduction

The history of developing surface-enhanced Raman spectroscopy (SERS) and surface-enhanced infrared absorption spectroscopy (SEIRAS) has been closely related to the understanding of the origin of plasmonic enhancement, and the development of nanoscience that allows customization of plasmons.[36,73–75] We have already discussed the importance of selecting a proper ATR 2D IR substrate in terms of the spectroscopy considerations such as band gap, reflectivity, refractive index, and compatibility with experimental conditions in Chapter 2. However, the substrate also plays an important role on the morphology of the plasmonic layer used for enhancement, as we will show in this chapter.

The important properties of both surface plasmons (SPs) and localized surface plasmons (LSPs) can be understood through classical electrodynamics. Many textbooks have derived these properties from Maxwell's equations, and show that the essence of SPs is collective oscillations of the electrons at a metal-dielectric interface.[74,76] These oscillations can be excited with light, and the design of the metal-dielectric interface has a large impact on the specific properties of the SP. While for simple systems such as a planar interface or a

spherical particle, the properties such as the electromagnetic field can be modeled easily, for more complex systems it quickly becomes intractable.[76] For those reasons, there has been a lot of focus on numerically modeling the plasmons of nanoparticle systems to find the magnitude of the enhanced field. The most common numerical methods are the discrete dipole approximation (DDA), and the finite difference time-domain (FDTD) method. The intricacies of the models will not be discussed here, but have been detailed elsewhere if the reader is interested, and may prove useful when designing interfaces, although these methods are not used in this thesis.[77,78] The use of such models has lead to a deeper understanding of the relationship between the shape and size of a nanoparticle, and the expected enhancement for complex systems. However, for rough surfaces there is no well-behaved model that can accurately predict enhancement in the IR.
This Chapter will briefly cover the local surface plasmons (LSPs) that are generated upon excitation with an external source, and how the generated LSPs depends on nanoparticle distance and resonance with the excitation source. Then we will evaluate the viability of several substrates for surface enhanced IR and 2D IR experiments. Finally, we will experimentally determine the sensitivity (or enhancement) as a function of distance from the surface.

4.2 Theoretical Model for Plasmonic Enhancement in Nanomaterials

To begin, we will look at the case of a single gold sphere immersed in water and model the enhanced field using the MNPBEM Matlab toolbox. The general approach for the model is

outlined below. The details and guide to using the toolbox have been published previously.[79]

For a metallic sphere embedded in a dielectric, excitation by an external plane wave will cause polarization of the free electrons in the nanoparticle, which will induce an electromagnetic (EM) field. The MNPBEM toolbox solves for the induced EM fields for a given perturbation by solving Maxwell's equations with boundary conditions placed at the nanoparticle edges. For particles where the diameter is much smaller than the wavelength of the incident plane wave, the quasi static approximation can be made that assumes the electric field varies in time much more slowly than the displacement of electrons in the particle. The simulations shown in this section do not make this approximation, but are shown as simpler case as the general approach remains unchanged. In this approximation, rather than solving the Helmholtz equation, the Poisson equation is solved for the electrostatic potential, where the solution is the electrostatic Green function with position vectors $\mathbf{r}$ and $\mathbf{r}'$.

$$\nabla^2 G(\mathbf{r}, \mathbf{r}') = -4\pi\delta(\mathbf{r}, \mathbf{r}') \tag{4.1}$$

$$G(\mathbf{r}, \mathbf{r}') = \frac{1}{|\mathbf{r} - \mathbf{r}'|} \tag{4.2}$$

For large IR wavelengths and nanoparticles on the order of and below tens of nanometers, this approximation is appropriate and leads to the following solution when considering a homogeneous dielectric particle with sharp boundaries to its external dielectric environment.

$$\phi(\mathbf{r}) = \phi_{ext}(\mathbf{r}) + \oint_{V_i} G(\mathbf{r}, \mathbf{s})\sigma(\mathbf{s})da \tag{4.3}$$

Where ϕ_{ext} is the external dielectric potential, σ is the surface charge distribution along the particle boundary, V_i is the dielectric particle and $r \in V_i$. Now we have to fulfill the boundary conditions and ensure that σ is the same inside and outside the particle for continuity. Additionally we can input the dielectric of the nanoparticle and its surrounding medium. After that, the following boundary integral equation is found.

$$A\sigma(\mathbf{s}) + \oint \frac{\partial G(\mathbf{s}, \mathbf{s}')}{\partial n}\sigma(\mathbf{s})da' = -\frac{\partial \phi_{ext}(\mathbf{s})}{\partial n} \tag{4.4}$$

$$A = 2\pi\frac{\epsilon_{np} + \epsilon_{bulk}}{\epsilon_{np} - \epsilon_{bulk}} \tag{4.5}$$

The solutions to equation 4.4 determine the surface charge. The partial derivatives taken with respect to n is taken along the direction normal to the outer surface, and ϵ_{np} and ϵ_{bulk} are the dielectric constants for the nanoparticle and surrounding medium, respectively. The integral is then approximated by taking the sum over j surface elements and equation 4.4 can be rewritten as follows, which is representative of the boundary element method (BEM).

$$A\sigma_i + \sum_j \left(\frac{\partial G}{\partial n}\right)_{ij}\sigma_j = -\left(\frac{\partial \phi_{ext}}{\partial n}\right)_i \tag{4.6}$$

The first term $A\sigma_i$ is governed by the dielectric function of the particle and surrounding medium. The second summation term contains $\left(\frac{\partial G}{\partial n}\right)_{ij}$, which connects the inside of the particle to the ouside over the boundary. The last term $\left(\frac{\partial \phi_{ext}}{\partial n}\right)_i$ is the surface derivation of the external potential. Once equation 4.6 is solved for a particular system, the induced electric field can be calculated easily from the gradient of the potential $\mathbf{E} = -\nabla\phi$. The enhancement in the field is then plotted as the normalized field by taking the square of the

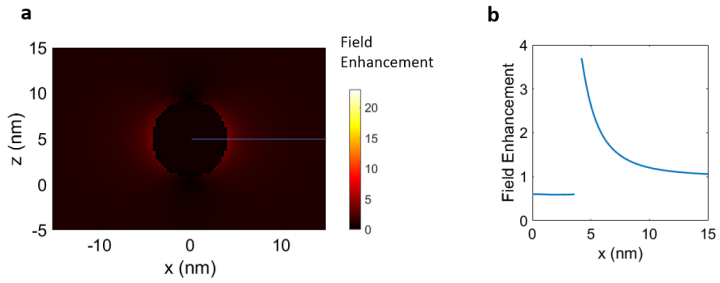

Figure 4.1: (a) BEM simulation using MNPBEM toolbox for a gold nanoparticle with a 8 nm diameter in water. The blue line indicates the slice that is plotted in (b), which shows the field enhancement decay away from the nanoparticle.

dot product of the sum of the incident and excited fields.

$$E_{enhanced} = \sqrt{(\mathbf{E_{inc}} + \mathbf{E_{ex}}) \cdot (\mathbf{E_{inc}} + \mathbf{E_{ex}})} \tag{4.7}$$

The general result using the BEM approach with the full Maxwell's equations is shown for a single gold nanoparticle in water in Figure 4.1, where the excitation source is a plane wave resonant with the plasmon frequency set at 600 nm and traveling in the y direction (excitation from below). The enhanced field can be seen in the lane of the polarization of the field, where orthogonal there is no field enhancement. This is a consequence of exciting the electron oscillations along the plane of polarization in the nanoparticle. The decay of the field enhancement away from the surface is plotted in Figure 4.1 b, which is a slice from Figure 4.1 a. The enhanced field quickly decays away from the interface, and a question that will be addressed in the next section is how far from the surface do we retain monolayer sensitivity?

For the case of two nanoparticles in close proximity, we can see in Figure 4.2 that the the enhancement is greatest for the case where the nanoparticles have only 1 nm of separation. As the distance increases between the nanoparticles there is a significant drop in the

amount of enhancement. This has been shown experimentally as well, and many SEIRAS and SERS approaches take advantage of the "hot spots" in nanoparticle arrays to gain high monolayer sensitivity.[80] These hot spots can also be introduced by roughening gold surfaces, such as through electrochemical roughening, or depositing rough gold in the first place, through methods such as sputtering.[81]

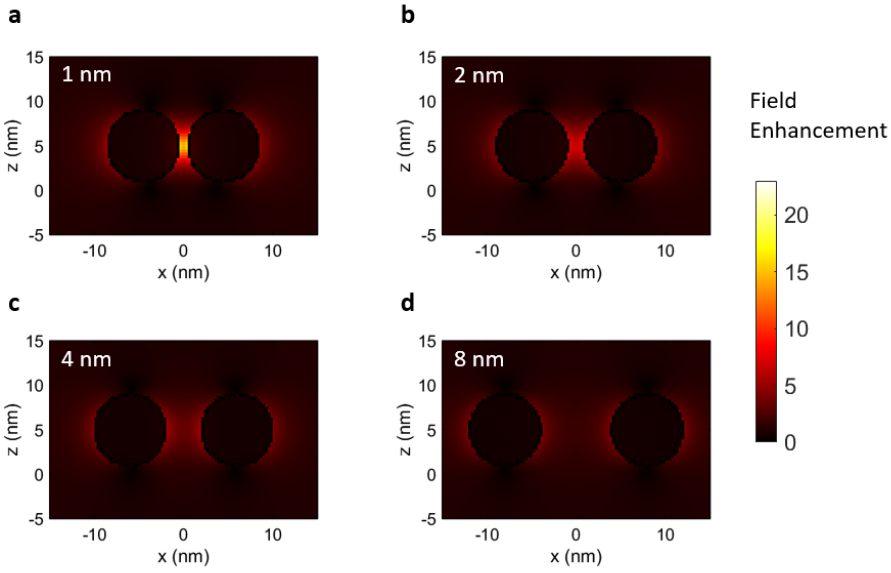

Figure 4.2: Field enhancement plotted for various nanoparticle distances for (a) 1 nm, (b) 2nm, (c) 4nm, and (d) 8nm. Nanoparticle diameter is 8 nm and modeled using the dielectric of gold. Surrounding medium is modeled as water.

Additionally, the resonance overlap between the excitation source and the plasmon frequency will play a large role in the field enhancement.[82] This can be seen by exciting the 1 nm separated nanoparticles first on resonance and then 200 nm off resonance. The results are shown in Figure 4.3. For the resonant excitation the field enhancement is much larger then when the excitation frequency is shifted.

For spectroscopy methods, the excitation source used also acts as the probe of the

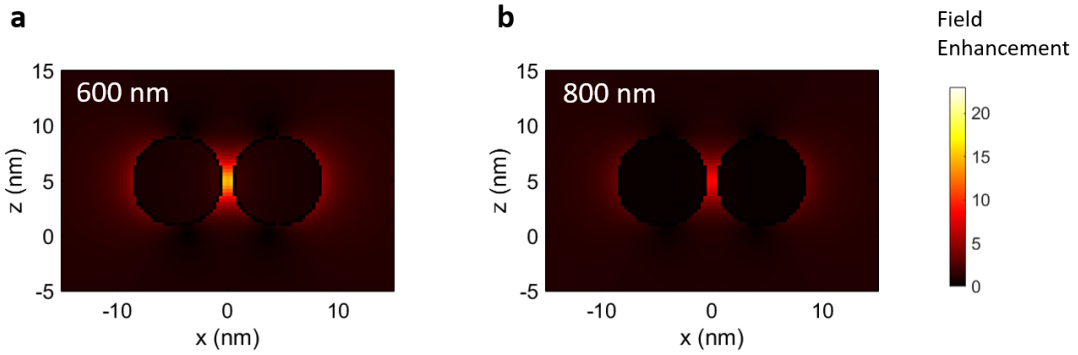

Figure 4.3: Field enhancement at 1 nm seperation distance for (a) resonant excitation with 600 nm light, and (b) off-resonant excitation at 800 nm.

monolayer, which means being able to tune the plasmon frequency to overlap with the frequency of interest will lead to much higher sensitivity. However, this comes at the cost of more complicated experimental procedures. A more general trend that can be taken advantage of is the observed relationship between the plasmon resonance and nanoparticle size. When working with metals like gold or silver, an increase in particle size leads to a corresponding redshift in the plasmon frequency, increasing the overlap into the IR and therefore also increasing the enhancement. The rest of this chapter will be dedicated to choosing a substrate for 2D IR ATR spectroelectrochemistry experiments, and experimentally determining the optimal balance between redshifting the plasmon resonance and decreasing the number of hot spots as the particle size grows and individual nanoparticles begin to merge.

4.3 Evaluation of IR Substrates

The selection of ATR substrate material is important when moving to 2D IR because there are additional considerations that are not present in linear IR measurements. With 2D IR

it is important to reduce dispersion through the ATR element, as well as avoid exciting free carriers in the material. We tested three potential ATR substrates: ZrO_2, CaF_2, and Si. ZrO_2 has the advantage of a high index of refraction, and in comparison to Si has a much larger band gap which reduces the probability of exciting free carriers in the substrate through multiphoton excitation. This is advantageous because the excitation of free carriers leads to large background signals. ATR prisms made from ZrO_2 are also durable and can be reused extensively. However, ZrO_2 is an uncommon optical material, necessitating custom manufacture of ATR elements. The absorption edge of ZrO_2 also rises steeply below 1600 cm^{-1}, which can lead to challenging signal isolation for carbonyl vibrational probes and large dispersion in this region of the spectrum, which must be carefully compensated with germanium.[83] CaF_2 avoids the problem of large dispersion in this frequency range, but has a low index of refraction which is problematic for ATR measurements, particularly with aqueous solutions. The CaF_2 spectra measured in this study are therefore in transmission mode, although we note that for certain solvents with lower indexes of refraction such as acetonitrile, or systems studied under air, CaF_2 may be a good choice as an ATR substrate. The last ATR substrate we used was a commercial IRUBIS Si ATR wafer that is compatible with the Jackfish J2 Spectroelectrochemical cell and ATR FTIR attachment. The main concern for Si is the possible excitation of free carriers, and potentially large reflective losses due to the high index of refraction, but with thin micromachined Si ATR wafers the reflective losses and dispersion are minimal. With the addition of a plasmonic layer, we are also able to obtain surface sensitivity with pump intensities as low as 100-200 nJ per pump pulse (100 fs pulse duration), which is below the threshold for multiphoton excitation of free carriers in Si.

To achieve surface enhancement, we sputtered Au thin films onto the substrates. A cartoon

illustrating the sample morphology is shown in Figure 4.4a, and a comparison spectrum of MCB in a solution of D_2O is shown in Figure 4.4b. Sputtered surfaces have the advantage of facile fabrication as compared to more highly enhancing plasmonic nanoarrays,[84–87] as well as an increased surface roughness in comparison to other deposition methods.[81] To optimize the signal from the molecular monolayer, we sputtered Au at several thickness ranging from 4 to 30 nm average thickness on each of the substrates and then functionalized the Au with MCB. We also investigated annealing and re-sputtering the Au films[88], but found that there was no difference in the enhancement. To determine the magnitude of the absorbance by the vibrational probe with respect to Au film thickness we measured the FTIR spectra of the MCB carbonyl stretch for each substrate and film thickness, shown in Figure 4.4c-e. The FTIR spectra were fit with a smooth polynomial baseline that excluded the carbonyl peak and then the fit was subtracted to isolate the molecular response. For the Si FTIR spectra shown in Figure 4.4e, the overlapping peaks around 1600-1650 cm^{-1}, which we assign to water adsorbed in the electrode material,[89,90] complicate the fitting, and thus are not included in background subtraction and the background is fit excluding a wider range from 1500-1850 cm^{-1}. Examples of the fitting and background subtraction for each substrate are shown in Figure B.1.

For the MCB monolayers, the carbonyl resonance frequency is not greatly different from the MCB in aqueous solution, but the MCB spectra have distinct variations by substrate. As expected from previous studies[91–94], there are obvious Fano distortions to the lineshape of the carbonyl peak and changes in intensity that vary as a function of Au thickness. We note that for sputtering, where the thickness of the film is the average thickness and the microscopic structure is highly inhomogeneous, there can be variations between samples prepared even when using the same method. This leads to changes in the enhancement and

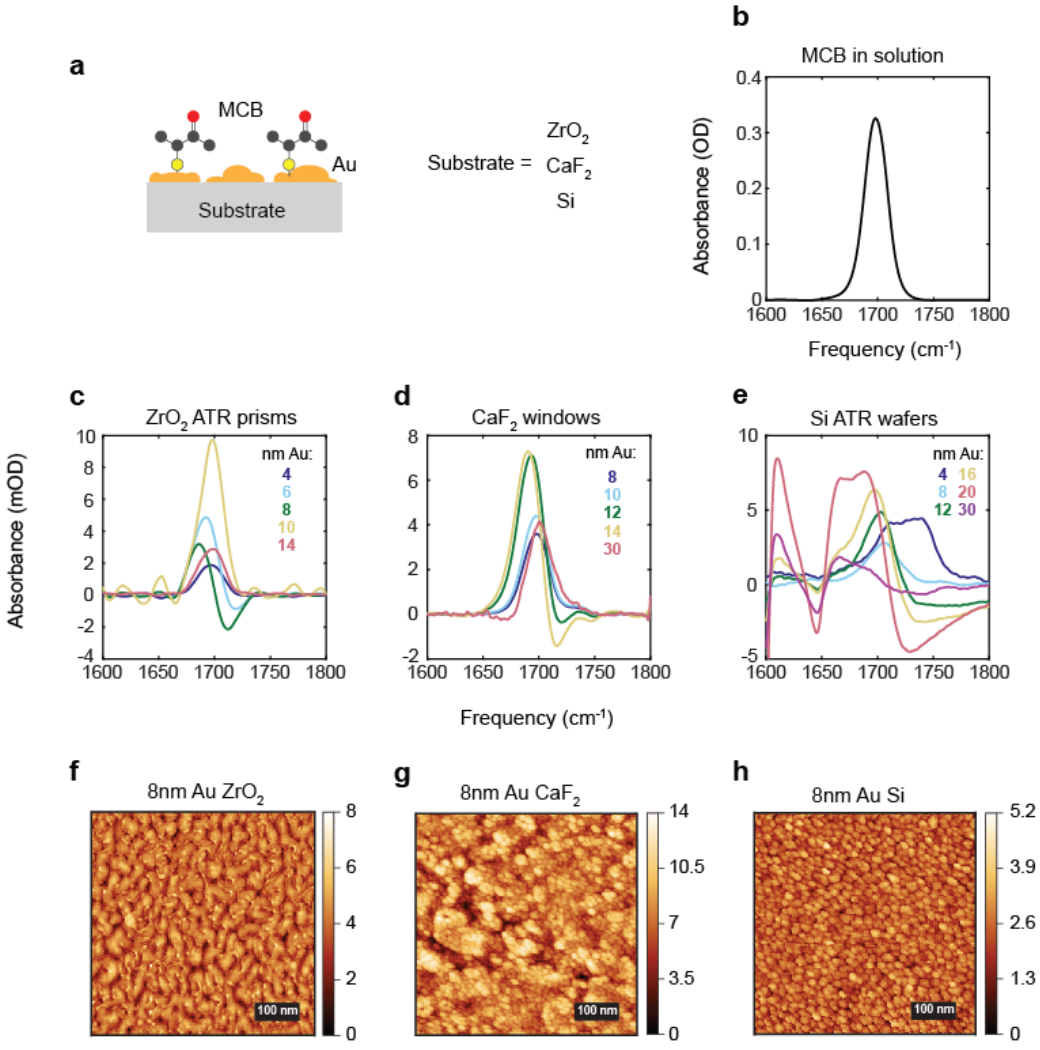

Figure 4.4: (a) Illustration of nanometer gold surfaces functionalized with MCB. (b) Bulk spectrum of MCB in D_2O solution. (c-e) The background subtracted FTIR spectra of MCB on different sputtered thickness of Au (gold film thickness values (nm) are indicated in the inset) on ZrO_2 ATR prisms, CaF_2 windows and IRUBIS Si ATR wafers with air (no solvent) above the sample. The FTIR with CaF_2 substrate is measured in transmission geometry, while all other spectra are ATR mode. (f-h) AFM images of 8 nm Au sputtered on ZrO_2, CaF_2, and Si, respectively.

lineshape between samples even when using the same preparation and film thickness. The Fano distortion appears as a redshift in the maximum frequency and the appearance of a

negative absorption dip on the blue side of the spectrum. For the Si substrates, as the Fano distortion increases the peak is shifted closer to the overlapping peaks from adsorbed water, but the same negative absorption on the blue side and increasing/redshifting peak absorbance is observed. The relationship between the lineshape and Au thickness is dependent on multiple factors, but most importantly the coupling between the broad plasmon and the narrow vibrational mode.[95] We provide more detailed discussion on the complexity of the lineshape changes and its origin in the vibration/plasmon coupling elsewhere. (unpublished results)

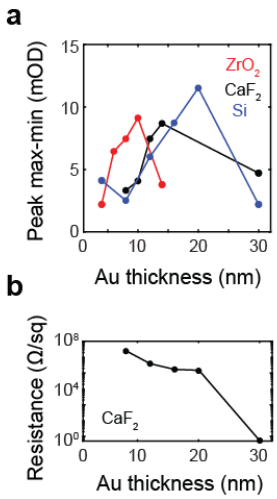

Figure 4.5: (a) Difference between maximum and minimum peak absorbance for MCB as a function of sputtered Au film thickness for three substrates: ZrO_2, CaF_2, and Si ATR wafers. (b) Sheet resistance as a function of sputtered Au film thickness on CaF_2 windows.

We quantify the enhancement of the carbonyl peak by taking the difference between the maximum and minimum peak absorbance of MCB. We see in Figure 4.5a that the enhancement initially grows with Au thickness, but reaches a maximum value between

10-20 nm before decreasing at higher Au coverage. The optimal Au thickness for maximizing the carbonyl peak enhancement is dependent on the substrate, with the ZrO_2 showing a maximum response at 10 nm Au, 16 nm for the CaF_2 and 20 nm for the Si. The decrease in carbonyl enhancement at high Au coverage is correlated to the sharp drop in resistance of the Au films, shown in Figure 4.5b, which become substantially more conductive with the increasing average thickness of the Au as the nanoislands percolate to form a connected surface.

The variation in the optimal Au thickness between the different substrates is likely due to the different percolation threshold for Au for the various substrates, which results in differences in the morphology as a function of average thickness. This is illustrated in in Figure 4.4f-h, where we show AFM images of the Au films with 8 nm average thickness on each substrate. On ZrO_2, the percolation threshold for the Au occurs at lower average thicknesses than the other two substrates, and at 8 nm already shows merging of the nanoislands. In contrast, 8 nm of Au on CaF_2 and Si shows a distinct pattern of spherical nanoislands. The two competing factors that lead to the greatest enhancement are the overlap of the plasmon resonance into the IR region, which increases with the size of the particles and is maximized for bulk Au, and the presence and density of nanogaps where the field is greatly enhanced. When the percolation threshold is reached, the plasmon resonance overlap into the IR is greater than that of nano-structured Au films, but the presence of nanogaps is greatly reduced, resulting in a reduction in the signal from the monolayer.[92,96] Because the enhancement of the monolayer signal is dependent on the coupling of the vibration to the plasmon, which is also the origin of changes to the carbonyl lineshape, there will always be a trade-off between signal enhancement and carbonyl lineshape changes. In this study we ultimately chose to use 12 nm thick films of

sputtered Au for our electrochemical experiments because it provides significant enhancement without the extreme distortions seen in the 20 nm thick Au films, but we recognize that this may not always be the best choice and expect that our results will help future researchers make informed decisions when designing interfacial IR experiments that rely on signal enhancement.

We can further demonstrate the impact of the Au thickness by observing the effect on the 2D IR lineshape, as well as the changes on the surface as compared to the spectrum in aqueous solution, shown in Figure 4.6. In panel (a) we show the spectrum of MCB in D_2O, where we see the usual form of a 2D IR spectrum with the $0 \rightarrow 1$ bleach transition appears as the positive (yellow-red) band and the $1 \rightarrow 2$ induced absorption appears as the negative (blue) band, shifted to lower frequency along the detection axis by the vibrational anharmonicity. These bands are elongated along the diagonal of the spectrum due to the transient heterogeneity in solution at early waiting time. In panels (b-d) we show the spectra for MCB functionalized on Au surfaces of increasing average thickness, which illustrate several differences in lineshape relative to the solution spectrum. Compared to the solution spectrum we see an increase in the diagonal linewidth with increasing Au coverage and a decrease in the antidiagonal homogeneous linewidth. One explanation is that this would indicate that the carbonyl groups of the MCB on the surface do not experience the same fluctuations as in solution, together with a larger degree of inhomogeneity due to local surface environments. For the 6 nm Au layer the spectrum is minimally phase-twisted showing equal intensity positive and negative peaks, whereas increasing Au coverage leads to a decrease of the negative intensity below the diagonal and growth of a negative feature above the diagonal. This is in tandem with changes in the signal intensity, with the 6 nm layer providing the least enhancement and the 12 nm layer

the greatest, comparable to the effect on the FTIR spectrum. Clearly, the impact of plasmon-vibration coupling needs to be explicitly addressed in interpreting the origin on the functionalized Au spectra. In a separate study we have developed a model that explains the essential features of these plasmonically-enhanced 2D IR spectra as arising from mixed character between the vibrational and plasmonic states.[97]

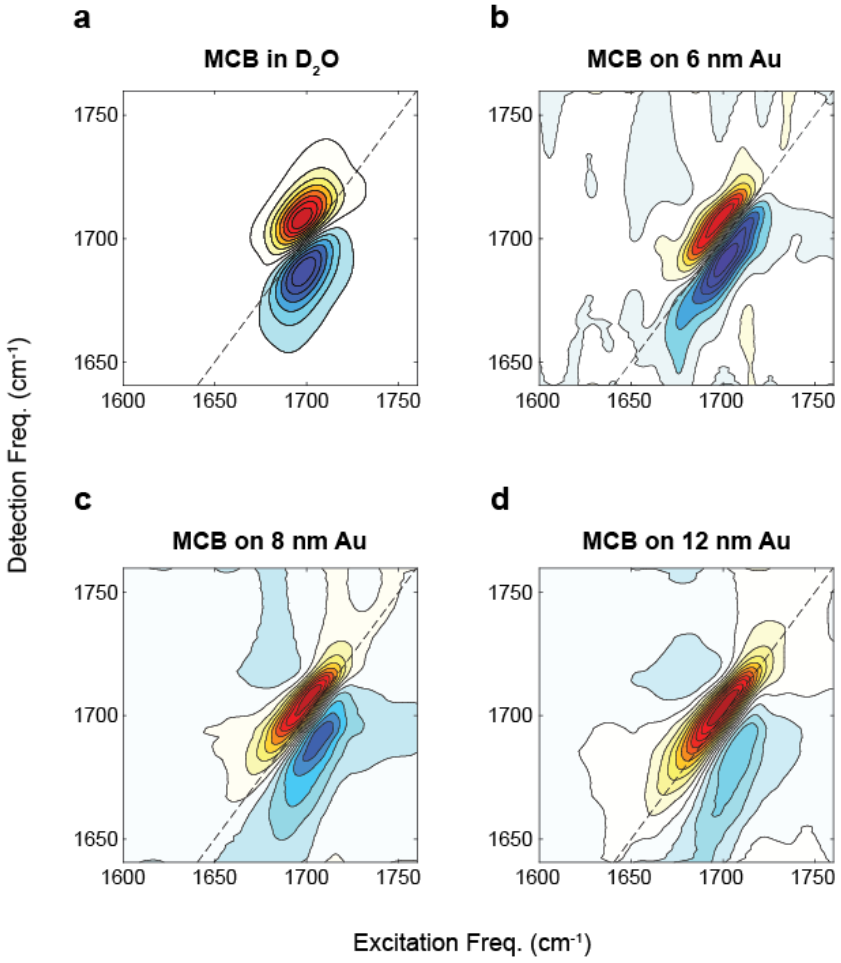

Figure 4.6: 2D IR spectra of carbonyl stretching vibration of MCB acquired at $t_2 = 300$ fs. (a) Bulk solution spectrum of 250 mM MCB in D_2O. (b-d) Spectra of MCB functionalized on Au layers of various thickness on CaF_2 at the interface with D_2O: (b) 6 nm, (c) 8 nm, (d) 12 nm. Each spectrum is individually normalize.

We also show the 2D IR spectra for MCB on each substrate in Figure 4.7a-c with Au film thicknesses of 8 nm for ZrO_2, 10 nm for CaF_2, and 12 nm for Si, to illustrate the impact of the substrate. The different thicknesses of Au films for each substrate reflect the film thickness that maximized the enhancement of the spectra. Similar to the FTIR measurements, the differences in morphology of the Au film on each substrate influences the degree of Fano phase twist in the 2D IR spectra, although here the variation is further emphasized. The effect of the Au film on the 2D IR lineshape is greatest for the example spectrum on Si in Figure 4.7c, where the ground state bleach/stimulated emission and excited state absorption peaks appear to be almost completely inverted. For ZrO_2 (Figure 4.7b) and CaF_2 (Figure 4.7c), the 2D IR spectra show a lesser amount of phase twisting, resulting in a negative-positive-negative pattern along the detection frequency axis rather than the conventional positive-negative pattern seen in solution spectra. This demonstrates that both the average Au thickness and the properties of the substrate are important for determining the appearance of the final spectrum. Comparing the FTIR of all three substrates, we observe that the center frequencies and line widths are similar, except for the ZrO_2 FTIR which shows a large phase twist at the same average Au film thickness that can be attributed to the different morphology of the Au on ZrO_2.

We can compare for each substrate the FTIR and the 2D IR by overlapping the pump slice amplitude[98] (PSA) and FTIR as shown in 4.7d-f. We see that while the PSA spectra for CaF_2 and Si are similar to the FTIR, ZrO_2 shows an extremely broadened diagonal line width and a large redshift in the peak frequency. This is in contrast to the FTIR of the ZrO_2 system, which is not dramatically dissimilar from the other substrates. We have previously used ZrO_2 successfully for 2D IR ATR measurements of bulk solutions,[99] so these unusual results on ZrO_2 seem to be related in some way to the surface preparation.

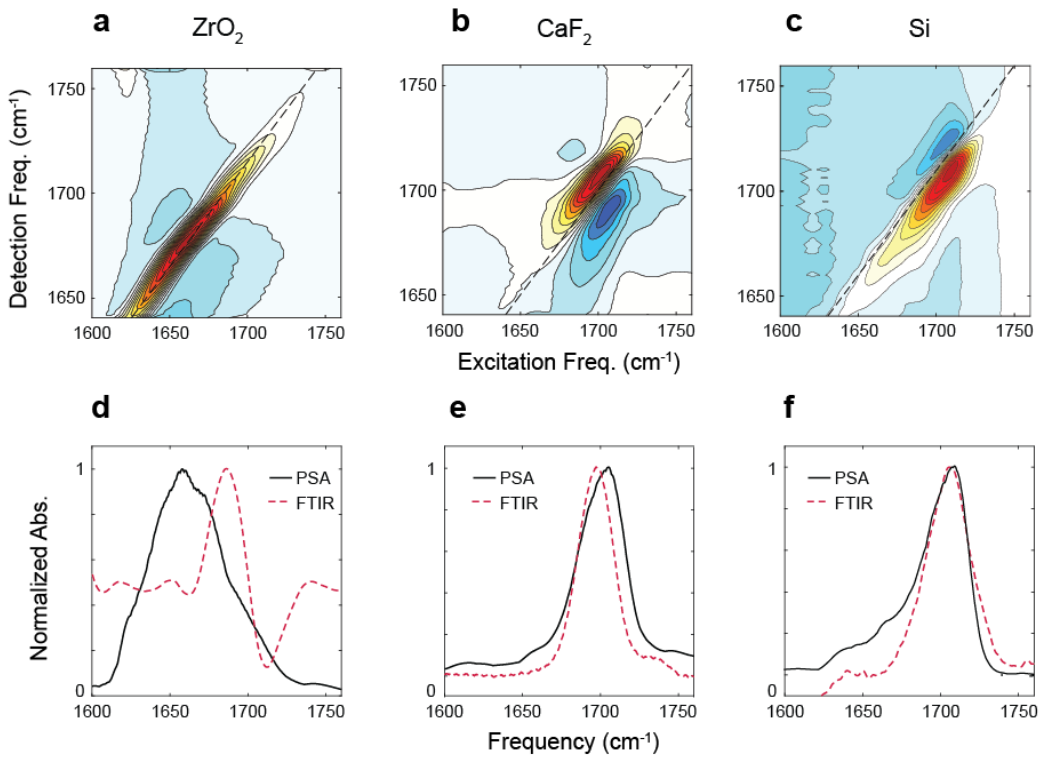

Figure 4.7: 2D IR spectra of MCB-functionalized Au films on different substrates is shown in panels (a-c) for ZrO_2, CaF_2, and Si, respectively. The Au film thickness is 8 nm on ZrO_2, 10 nm on CaF_2, and 12 nm on Si. The lower panels (d-f)show the corresponding pump slice amplitudes (PSA) overlaid with the FTIR spectra for the corresponding system.

While the origin of the distortion of the 2D IR spectrum on ZrO_2 is not entirely clear, it precludes the use of this substrate for 2D IR measurements of surface bound species. While CaF_2 substrates show comparable results with the Si substrates, Si has the major advantage of being a universal substrate for many surface studies, and therefore there are a large range of functionalization and characterization techniques that have been developed for Si substrates. In this study we focus on developing one specific method that integrates ITO electrodes grown on Si and 2D IR, and expect the principles used in this study to design the 2D IR compatible electrodes can be applied to the 2D IR studies of other

Si-based interfacial systems which may require alternative electrode design. Therefore, we focus on the Si substrates for further spectroelectrochemical application in Chapter 5

4.4 Experimental Enhancement Factors and Penetration Depth

In order to investigate the entirety of the EDL, vibrational probes can be placed a specific distance from the interface by adjusting the length of the tether. Since sensitivity to monolayers relies on plasmonic enhancement, it becomes important to understand how this enhancement might change as we place our probe further from the surface. It is well known that the electric field generated by surface plasmons drops off rapidly as a function of distance from the plasmonic particle.[73,74] However, when looking at a real surface the heterogeneity of the system quickly introduces difficulty when trying to model the plasmon. We can experimentally determine the practical limit for how far from the surface we can tether vibrational probes by using a model film grown on top of the plasmonic layer and looking at absorbance as a function of the model film thickness. This approach has previously been used by depositing varied thicknesses of PMMA on gold and silver thin films (Schatz, check for more references or methods). Here we use ALD grown Al_2O_3 and integrate over some of the Al-O modes that absorb below 1000 cm^{-1} on gold thin films (referenced to the growth on bare Si) as a function of cycles to determine the change in enhancement factor as a function of distance from the plasmonic layer. The results of this experiment is shown in Figure 4.8. While the growth per cycle of ALD can theoretically be predicted for ideal film growth (one atomic layer per cycle, approximately 0.12 nm), experimentally the growth per cycle depends on the experimental conditions such as pulse

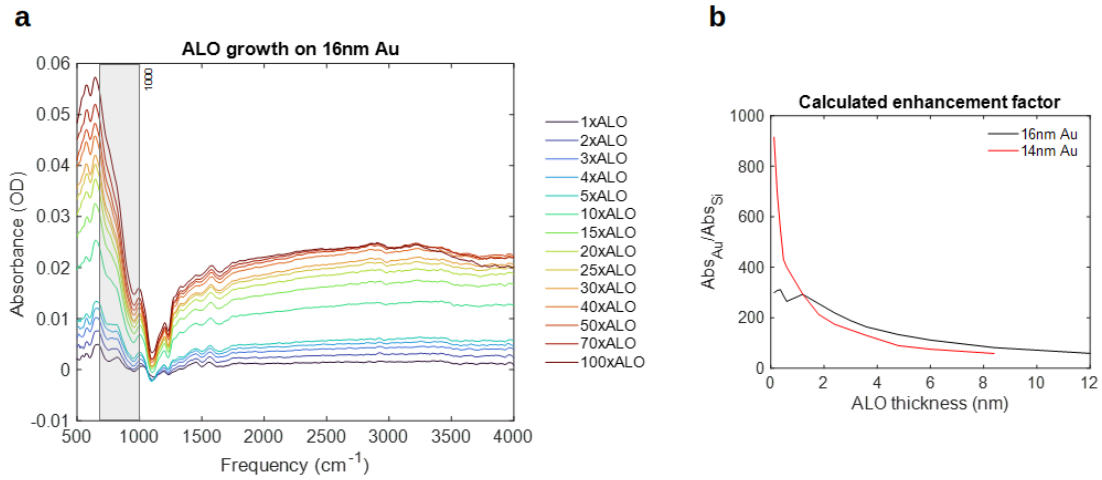

Figure 4.8: (a) Transmission FTIR spectra as a function of Al_2O_3 (ALO) cycles grown on a 16 nm sputtered gold film. The gold film was sputtered on a si wafer with 2 nm of ALD Al_2O_3 on top to minimize morphological differences between the gold films used in this study and the ones used in electrochemical experiments in Chapter 5. The highlighted region of the spectra in (a) was integrated and then divided by the amount of absorbance seen in the Al_2O_3 on Si case to provide the estimated enhancement factor, and the Al_2O_3 thickness was estimated by using the theoretical growth per cycle in nms.

and purge times, reactivity of the precursors with the substrate, concentration of precursors, and temperature of the substrate. The major assumption made when estimating the enhancement factor using Al_2O_3 grown on gold vs Si is that the early growth rate will be the same for both substrates. However, for experiment it is still useful to determine how quickly the relative enhancement decays in order to have an upper bound on the maximum distance a vibrational probe can be placed from the interface.

Figure 4.8 a shows the region of integration for determining the enhancement factors, while b shows the calculated enhancement factors for both a 14 nm and 16 nm thick sputtered gold film. The enhancement factor is shown as the integrated absorbance from the Al_2O_3 grown on gold films (Abs_{Au}) divided by the integrated absorbance of Al_2O_3 grown on plain Si (Abs_{Si}). The difference in absorption between the Al_2O_3 grown on gold and the Al_2O_3

grown without gold should correlate to the amount of enhancement from the presence of the gold layer. This can be measured as a function of the thickness of the Al_2O_3 layer by measuring the FTIR spectra at various different Al_2O_3 growth cycles. The Al_2O_3 thickness is estimated by taking the number of cycles multiplied by the theoretical growth per cycle of 0.12 nm. For the 14 nm Au film, there is initially a huge enhancement factor close to 900, but that quickly drops off. The 16 nm film shows initially smaller enhancement, but the enhancement drops off slower than the 14 nm film. This difference in loss of enhancement can be explained by the different particle sizes, where for larger and larger particles we expect the enhanced field to be maintained further from the surface. The difference in initial enhancement can be attributed to the presence of more "hot spots" in the 14 nm film case. For our experiments, the critical enhancement factor is not known, but since we do see signal for a monolayer of mercaptobutanone with a 16 nm Au film on Si, we can conclude that an enhancement of approximately 300 is enough for monolayer sensitivity. Therefore with a 14 nm sputtered Au film we should be able to maintain sensitivity up to 1-2 nm from the surface.

Chapter 5

Electrode Development

5.1 Introduction

In this chapter we present a novel electrode design for 2D IR studies of the electrochemical interface, which is a challenging experiment for several reasons intrinsic to IR spectroscopy, including the intrinsically low oscillator strength of IR active molecules, and lack of specificity to the interface. One of the major approaches for overcoming these challenges is through the use of tethered or adsorbed molecules at the interface, which provides surface specificity, and the inclusion of a plasmonic metal, usually Au or Ag, to provide local electric field enhancement, which enhances the magnitude of the signal.[36,92,100] The highest enhancement factors for IR absorption are found in small nanogaps between the nanostructures where the electric field is magnified greatly.[84–87] One of the difficulties of plasmonic enhancement is the possibility of phase-twisted Fano lineshapes that can complicate the interpretation of the surface-enhanced spectra in both linear and 2D IR spectra. Additionally, experimentally investigating solid-liquid interfaces with 2D IR remains a difficult task due to complications that arise when using ultrafast pulses in conjunction with traditional substrates for SEIRAS. This is especially a concern for 2D IR

experiments of electrochemical interfaces because typical bulk conductors and semiconductors can give rise to large transient reflection background signals from excited free carriers.

The Kretschmann configuration, whereby the working electrode is deposited as a thin film on the surface of the optical element for attenuated total internal reflection (ATR), is preferred when integrating FTIR and electrochemical studies because of the advantages in the design of the electrochemical cell.[35,50] In addition to simplifying the inclusion of the electrodes necessary for electrochemical measurements, one of the main advantages of this experimental geometry when working with small signals from monolayers of vibrational probes is to reduce the solvent background absorption by restricting it to the micron-scale penetration depth of the evanescent wave rather than the full path length through a transmission cell. For these reasons we focus our discussion primarily on substrate materials that can be used as ATR elements, although we also provide comparison with transmission measurements. The choice of materials used are based off the discussion in Chapter 2.3. To summarize, the additional concerns with 2D IR spectroelectrochemistry is the dispersion of the ATR material, the potential for multi-photon excitation of materials like Si and Ge, and robustness of the ATR material when exposed to harsh electrochemical conditions.

To address these concerns, in Chapter 2 we tested multiple potential ATR substrates —ZrO_2, CaF_2, and Si —for viability by sputtering thin films of Au onto the substrates that are used both for plasmonic enhancement and as the reactive layer to functionalize the surface with 3-mercapto-2-butanone (MCB), which acts as a local vibrational probe of the interface. The linear and 2D IR spectra are measured to compare the relative performance of the different substrates. We furthermore measured the linear IR spectra as a function of Au film thickness to determine the relationship between the film thickness intensity of the

signal of the MCB carbonyl stretch mode. Previous studies have shown that vibrational probes such as CO and nitriles are sensitive to the interfacial electric field, and demonstrated their utility in studying the properties of electrochemical interfaces.[41,64,101–103] We choose a carbonyl as our vibrational probe because the frequency can be correlated to the local electrostatic field[7,13,104], and does not suffer from the same complications as nitriles in hydrogen-bonding solvents where there are contributions from both the π and σ hydrogen bonding interactions.[2,105]

For the final electrode design for our experiments we have developed a layered electrode that can be used in the Kretschmann ATR geometry and takes into account all of the challenges of performing 2D IR spectroelectrochemistry at the electrode-electrolyte interface. We choose Si as a substrate because of its versatility as a universal substrate for surface studies which makes it a good base for fabricating many types of electrodes. ITO is used as a conductive layer, with a thin layer of Al_2O_3 acting as an adhesion layer for nanostructured Au which is functionalized with MCB. We evaluate the electrochemical performance of the electrodes, demonstrate the changes in the linear IR and 2D IR spectra as a function of applied potential, and determine the potential of zero charge to provide a meaningful reference potential for measured IR spectra.

5.2 Methods

5.2.1 Materials

We evaluated three IR compatible materials to serve as substrates for our experiments. Cubic zirconia (ZrO_2) ATR prisms (10mm $\times$ 10mm prisms with an 80° apex angle) were obtained from Supply Chain Optics. Undoped Si wafers micromachined for use as ATR IR

substrates (Universal ATR Crystal, 11mm × 9mm × 0.5mm) were obtained from IRUBIS. Throughout this study, we refer to these as Si wafers. 25 mm ∅×1 mm thick CaF_2 windows were obtained from Crystran. Prior to deposition of Au or electrode materials, the substrates were cleaned by rinsing in DI water and then submerging in methanol for 15 minutes and dried under a stream of nitrogen.

3-mercapto-2-butanone (MCB), NaCl, and solvents were purchased from Sigma-Aldrich and used as received. D_2O (99.9%) was purchased from Cambridge Isotope Laboratories. Sulfuric acid, hydrochloric acid (36.5 to 38%) and nitric acid were purchased from Fisher Scientific. Atomic layer deposition (ALD) reactants, including Cyclopentadienylindium(I) (InCp), Tetrakis(dimethylamino)tin(IV) (TDMASn) and trimethylaluminum (TMA), were purchased from Strem and used as received.

5.2.2 Surface Fabrication

In addition to measurements using the full layered electrode that we have developed, we performed a series of tests using only Au deposited directly onto the substrates. Gold was deposited with a Cressington 208HR sputter coater equipped with a quartz crystal microbalance to control average film thickness. A 99.99% Au target (Ted Pella) was used with a 40 mA current for an average deposition rate of 3.7 nm per minute. Following sputter coating, samples were submerged overnight in an ethanol solution of 50mM MCB to functionalize the Au, and subsequently rinsed gently in DI water and ethanol and dried under a stream of nitrogen.

For the full layered electrode fabrication, indium tin oxide (ITO) and Al_2O_3 thin films were grown by atomic layer deposition (ALD) in a custom viscous flow reactor, the details of which have been described previously.[106] ALD films were grown at 0.7 torrs under constant

vacuum with ultrahigh pure nitrogen gas flow of 225 sccm mass flow rate, and at a constant reactor temperature of 250°C. For ITO deposition, InCp and TDMASn were reduced with ozone with pulse/purge times of InCp:Ozone 3s/5s:5s/10s and TDMASn:Ozone 2s/10s:2s/10s.[107,108] During the reaction InCp and TDMASn precursors were held in stainless steel bubblers at 45°C to achieve sufficient vapor pressure for ALD reactions. For every 19 cycles of InCp:Ozone there was one cycle of TDMASn:Ozone, to obtain 3.3% Sn-doping, confirmed by XPS. A total of 130 ALD cycles of ITO (In + Sn) was performed to deposit 20 nm of film, confirmed by ellipsometry measurements (J. A. Woolam Co. M2000V Vase). Al_2O_3 films were grown directly on top of the ITO layer in the ALD reactor using TMA and H_2O as precursors with pulse/purge times of 1s/10s for both reagents. After ALD of ITO and Al_2O_3, the surfaces were cleaned as described above and Au was sputtered on top of the Al_2O_3 layer and functionalized with MCB.
To remove the electrode materials from Si ATR wafers for reuse, the Au was wiped off and then the oxide layers were removed by first submerging in 2% sulfuric acid on a 100°C hot plate for 5 min and subsequently in aqua regia on a 60°C hot plate for 15 minutes.

5.2.3 Surface Characterization

Atomic force microscopy (AFM) images were obtained with a Bruker Multimode 5 AFM with BudgetSensor Tap300-G probes (Ted Pella). The images were processed with Gwyddion v2.61.[109] Conductivity was measured with a Jandel 4-point probe.
XPS measurements of the Au4f peaks at 84 and 88 eV were performed using a Thermo Fisher K-Alpha+ spectrometer. The data were analyzed using Avantage software (Thermo Fisher) and the spectra were referenced to the adventitious C1s peak at 284.8 eV. An average of five scans was presented for each reported spectrum. The X-ray source was a

microfocused monochromatic Al Kα (1487 eV) beam with a spot size of 400 μm. For the survey scans, 200.0 eV with a step size of 1.000 eV of pass energy was utilized. When performing the high-resolution XPS measurements, 50.0 eV with a step size of 0.100 eV of pass energy was used.

5.2.4 Electrochemistry

For electrochemical measurements, the ITO/Al_2O_3/Au/thiol monolayer samples on top of the Si ATR wafers were used as the working electrode in a Jackfish J2 Spectroelectrochemical cell with a Ag/AgCl (3 M KCl) reference electrode and Pt wire counter electrode. The Si ATR wafers are designed to be compatible with the Jackfish cell and are assembled as per the manual. A potentiostat (Gamry, Interface 1010E) was used to control the electrochemical potential of the sample.

Cyclic volammetry (CV) measurements were scanned between -300 and 500 mV, starting at -300 mV, with a scan rate of 1 V/s, and were repeated 10 times sequentially. FTIR spectroelectrochemical measurements were performed by taking the background at 0 mV vs Ag/AgCl and stepping the potential sequentially between 500 and -500 mV in 50 mV steps, and 2DIR spectroelectrochemical measurements were performed by measuring spectra at 300, 0, and -300 mV. For CV and spectroelectrochemical measurements, the supporting electrolyte was 100 mM KCl in D_2O that had been purged with N_2.

For potentiostatic electrochemical impedance spectroscopy (EIS) measurements, the applied AC voltage frequency f was scanned from 0.2 to 300000 Hz with 10 points taken per decade. The AC amplitude was set to 14.1 mV and the default number of cycles per frequency step was used. The DC offset was scanned from 0.5 to -1 V in steps of 10 mV.

The supporting electrolyte for EIS measurements was 10 mM KCl in H_2O that had been purged with N_2.

5.2.5 IR and 2D IR Spectroscopy

Linear absorption spectra were measured with a Bruker Tensor 70 Fourier transform IR spectrometer with a variable angle attachment for the ATR measurements (Pike, VeeMax III), set to 50° angle of incidence.

For CaF_2 substrates, all spectra were measured in transmission mode using two CaF_2 windows with a 6 μm spacer to reduce the solvent background from D_2O while keeping the windows from incidental contact that could damage the Au thin film. Only the first CaF_2 window in the beam path was coated to reduce reflection losses and interference from back-reflection off of a second Au film. For CaF_2 FTIR measurements the background spectra were collected of air with the cell removed. ZrO_2 prism and Si wafer FTIR spectra were measured in ATR mode using a clean substrate as the background. For FTIR measurements with an applied potential, the background was taken at 0 mV vs Ag/AgCl. For Si ATR wafers, the micromachined grooves were oriented parallel to the beam path for the FTIR according to the manufacturer guidelines. For 2D IR measurements the micromachined grooves were oriented perpendicular to the beam path so that the beams were incident on only one face of the Si ATR wafer to reduce scatter.

Ultrafast 2D IR measurements were taken in the pump-probe geometry with a custom built spectrometer described in detail elsewhere[99] using mid-IR pulses centered at 1700 cm^{-1} with a full-width half maximum bandwidth of 200 cm^{-1}, 15 μJ per pulse, and 100 fs pulse duration. Briefly, the probe pulse is split from the pump using the front face reflection of an uncoated wedged CaF_2 window. The waiting time τ_2 between the pump

and the probe is controlled by a delay stage (Aerotech) in the probe beam path. The pump beam is sent through a pulse shaper (Phasetech, Quickshape) which generates a phase-locked pulse pair with controllable delay τ_1 and is used to compensate for dispersion. The probe and pump beams were focused into the sample with 90° off-axis parabolic mirrors. For transmission measurements, the sample was placed directly in the beam focus of a 4 inch focal length mirror (150 μm spot size). For ATR measurements, we used 6 inch focal length mirror (200 μm spot size at normal incidence) with the addition of two gold mirrors to create a 50° angle of incidence onto the ATR prisms. The pump intensity was attenuated ($100 - 200$ nJ per pump pulse) to prevent damage of the gold film and to mitigate the nonresonant response from the ATR element. The change in probe intensity induced by the pump is measured using a spectrograph (Horiba, Triax 190) equipped with a 64 element HgCdTe detector (IR Associates) to obtain the detection frequency axis. For the transmission 2D IR measurements the pump and probe were set to the *ssss* polarization. To minimize pump scatter contamination of the signal, all 2D IR ATR measurements shown were measured in the cross-polarized *ppss* configuration with the pump *p*-polarized and the probe *s*-polarized with respect to the interface. The polarization of the pump and probe beams were set by $\frac{\lambda}{2}$ waveplates (Alphalas) and wire grid polarizers (Thorlabs). The polarization of the detected signal is set to *s* with a wire-grid analyzer placed immediately before the spectrograph.

5.3 Results and Discussion

5.3.1 Electrode Fabrication on Si ATR Wafers

A conductive substrate is a requirement for electrochemical experiments. Because the MCB signal also decreases significantly on conductive Au films, we use a layered approach to decouple the plasmonic enhancement from the conductivity of the electrode. Specifically, we incorporate a conductive layer of indium tin oxide (ITO), beneath the thin plasmonic Au. This approach has previously been demonstrated for FTIR applications[110–112] and more recently for 2D IR.[64,102] We choose to use ALD to fabricate the ITO layer due the atomic level control that it provides via self-limiting growth, and its ability to grow high quality, low resistivity thin films.[107] By separating the plasmonic material from the bulk conductor of the electrode, we are able to separately optimize each layer. However, this flexibility in the design comes at the cost of the additional complexity in the fabrication, and additional considerations such as the quality of adhesion between the layers.

To improve the adhesion of the Au layer to the ITO, we incorporate a thin (1-2 nm) Al_2O_3 layer on top of the ITO, also grown through ALD, which covalently binds to the ITO and serves to increase the adhesion of the Au layer as compared to bare ITO.[113,114] A cartoon illustration of the layered electrode construction is shown in Figure 5.1a-c. We tested the adhesion strength of Au to ITO vs Al_2O_3 and the bare Si substrate by sonicating a sample with a 14 nm layer of Au for 25 minutes in methanol, acetone, or a saturated aqueous NaCl solution. We then determined the subsequent loss of Au coverage with XPS, using the area of the Au4f peak before and after sonication (Figure B.2). This test was designed to simulate conditions harsher than spectroelectrochemical experiments, which are performed without sonication in a static 0.10 M KCl solution, and should represent a worst case

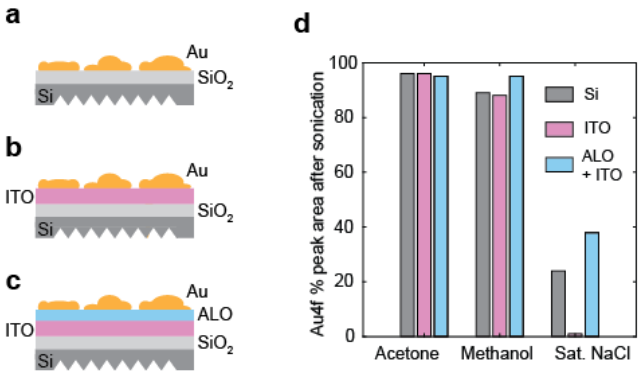

Figure 5.1: Adhesion of 14 nm sputtered Au on different fabricated substrates as quantified by XPS. Results for adhesion test shown are shown for (a) 14 nm of sputtered Au on bare Si, (b) ALD grown ITO on Si, and (c) ALD grown Al_2O_3 on ITO/Si. (d) XPS peak area normalized to the unsonicated case for three solvents: acetone, methanol, and saturated aqueous NaCl solution.

scenario for the loss of Au under normal operation. The results of this test are shown in Figure 5.1d. For organic solvents that are commonly used to clean surfaces or as the medium for functionalization of Au with thiols, there is very little loss of Au after sonication. For the concentrated NaCl solution, the Au is completely removed after sonication when it was sputtered directly onto the ITO layer, as compared to 24% remaining on the bare Si and 38% with the thin layer of Al_2O_3. The AFM images showing the morphology of the different surfaces (ITO, Al_2O_3, and Si) as well as the images of the Au coated surfaces before sonication are shown in Figure B.3. Although we cannot determine if the Au film is being dissolved in solution or the mechanical perturbation from sonication is leading to removal of the film, this test provides us with confidence that the inclusion of ITO and Al_2O_3 layers between the Si substrate and the plasmonic Au layer will result in a sufficiently robust electrode for our purposes. We also verified that the

insulating Al_2O_3 layer was sufficiently thin to maintain low resistivity. When testing the resistivity of the full electrode (layered ITO and 12 nm Au) with and without the Al_2O_3 layer, the increase in sheet resistance was minimal (from 16 to 58 Ohms/sq). Common alternative adhesion layers for Au on oxides include thin films of Ti or Cr, which should be investigated, but may cause problems by reducing IR transmission through the electrode.

5.3.2 IR and 2D IR Spectroelectrochemistry

In Figure 5.2 we characterize the electrochemical performance of our MCB functionalized electrodes before measuring the FTIR spectra as a function of electrochemical potential. All experiments and spectra measured with an applied voltage are performed with a layered electrode fabricated on an Si ATR wafer with 20 nm ITO, 1.2 nm Al_2O_3, 12 nm Au, and functionalized with MCB. The CV, shown in Figure 5.2a, demonstrates a stability window from -300 to 500 mV where minimal electron transfer processes are taking place, and a stable response over 10 cycles, demonstrating the electrochemical stability of the electrode and electrolyte over this potential window. The dominant response in the CV in this window comes from the charging and discharging of the EDL. We attribute the small redox wave centered at 0.25 V to chloride adsorption and desorption, as they are not present when $KClO_4$ is used as the electrolyte (Figure B.5).

To choose a physically meaningful reference potential, we used electrochemical impedance spectroscopy (EIS) to determine the potential of zero charge (E_{pzc}), the potential at which the electrode has on average no net surface free charge.[115,116] To determine E_{pzc} from EIS measurements, the modulus of the impedance $|Z(E, f)|$ was modeled and fit to a Simplified Randles equivalent circuit, shown in equation 5.1:

$$Z(E,f) = R_s(E) + \frac{1}{\frac{1}{R_F(E)} + 2\pi i f C_{DL}(E)} \tag{5.1}$$

Here, E represents the DC potential and f is the AC frequency of the potential, R_s is the uncompensated resistance of the solution, R_F is the Faradaic resistance and C_{DL} is the double layer capacitance of the working electrode. E_{pzc} is then identified as the potential at which C_{DL} is minimized. An example fit for the impedance is shown in Figure B.4. As shown in 5.2b, E_{pzc} is observed at -410 mV. E_{pzc} serves as a meaningful reference due to the influence that the surface charge has on the interfacial properties of the electrode, particularly the state of the EDL. It has been associated with a change in the water orientation at the interface that has been probed with both IR and VSFG spectroscopy.[48,117]

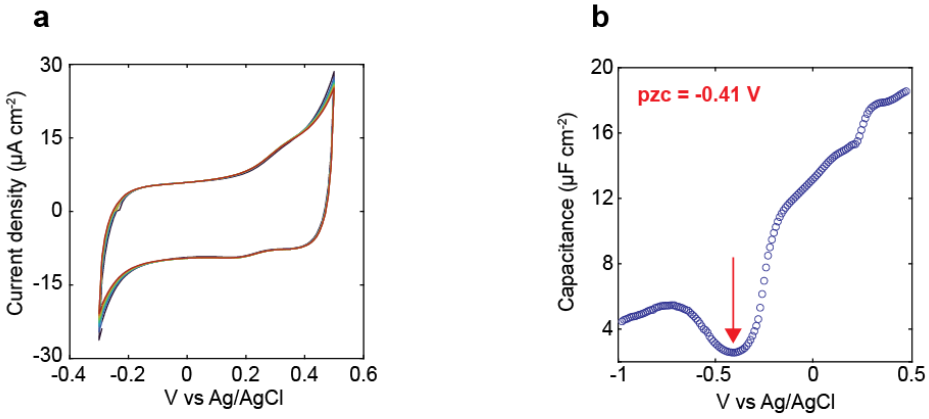

Figure 5.2: (a) Cyclic voltammogram of the layered electrode (12 nm Au/1.2 nm Al_2O_3/20 nm ITO on Si ATR wafers) functionalized with MCB which is shown to be stable over 10 cycles. (b) capacitance determined from EIS measurements as a function of potential, where we assign the minimum in capacitance at -0.41 V vs Ag/AgCl to coincide with E_{pzc}.

For these reasons, the FTIR difference spectra in Figure 5.3a are shown in reference to the -400 mV spectra, approximately at E_{pzc}. We can also indirectly measure the MCB

spectrum as a function of potential by holding the potential at -750 mV for 15-20 minutes to desorb the monolayer after cycling the potential. The subsequent bleach feature from the loss of the monolayer can then be subtracted from the difference spectra to recreate the MCB spectrum. Here we see that there are subtle changes to the FTIR around E_{pzc}, and interpret that as sensitivity to the surface charge. The overall blue shift seen in the FTIR difference spectra when scanning the potential to positive values can be interpreted as an electrochromic shift induced in the carbonyl groups oriented perpendicular to the surface, with the more positive potentials giving rise to an electric field oriented towards the surface and contracting the equilibrium bond length, thereby increasing the frequency. There is also the possibility of other effects contributing to the response of the probe, such as the direct polarization effect due to changes in the electron density of the molecule. This effect has been discussed in the case of 4-mercaptobenzonitrile monolayers, where the vibrational probe is directly conjugated to the surface through an aromatic group and is unlikely to be a major effect for the alkyl ketone studied here.[118,119] For the present discussion, in the difference spectra the decrease in absorption is referred to as the negative peak, while the increase in absorption is the positive peak. As illustrated in the plot in Figure 5.3c-d, the negative peak responds to the change in potential with a large shift in maximum frequency and a small change in intensity as shown with the red triangle markers. The positive peak responds in the opposite manner, with a small shift in the maximum frequency but a large change in the intensity, and this is illustrated with the blue triangle markers.

Next we demonstrate the impact of the electrochemical potential on the 2D IR spectrum of the MCB carbonyl. The 2D IR spectra at -300 and 300 mV vs Ag/AgCl are shown in Figure 5.4a and b, and the difference spectrum is shown in panel c. The 2D spectra are collected on the same sample without removing or otherwise changing any parameters

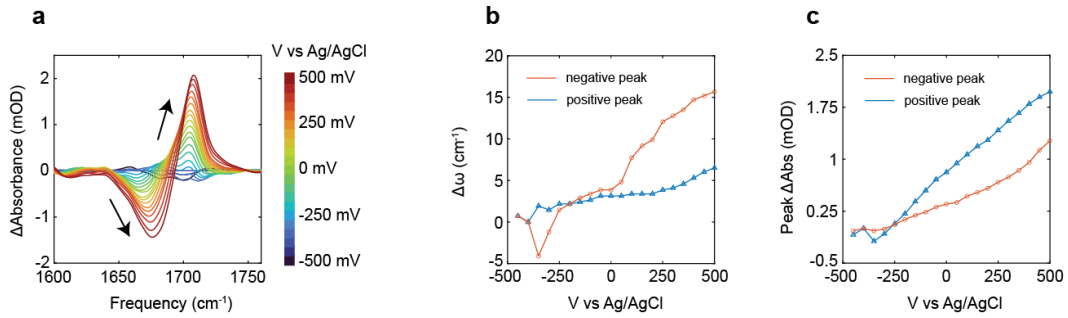

Figure 5.3: (a) FTIR difference spectra of MCB on 12 nm Au sputtered on Al_2O_3/ITO/Si substrates with respect to -400 mV vs Ag/AgCl reference electrode and 100 mM KCl supporting electrolyte in D_2O. Difference spectra are additionally background subtracted to remove baseline shifts due to potential dependent changes in the electrode absorption. The baseline shift as a function of potential for the ITO/ALO and ITO/ALO with 12nm Au is shown in B.6. Before any spectra were measured, the electrode was cycled 10 times from -300 mV to 500 mV. (b-c) Changes in the peak frequency and absorbance vs the applied potential for the loss (negative peak) and gain (positive peak) features of the spectra.

besides cycling the potential and no adjustments to the signal intensities prior to taking the difference are necessary. Due to the longer acquisition time when measuring 2D IR spectra as compared to FTIR, we chose to collect the 2D spectra at potentials no greater than -300 mV or 300 mV vs Ag/AgCl to avoid degradation of the surface that may occur at longer timescales under an applied voltage. In Figure 5.4a and b, there is a clear change in the spectra that corresponds to the center frequency of the peak shifting. The change from more negative to positive potentials can be emphasized by taking the difference spectrum (panel c) of the two spectra measured at -300 mV and 300 mV. Much of the baseline variation of the 2D spectrum is removed with subtraction, indicating that these features (which have also been observed in other potential-dependent 2D IR studies[120]) arise from static features not responsive to the applied voltage. In the difference spectrum it is clear that the magnitude of the response is distinctly different that that shown in the

FTIR, where the absorbance on the blue side was greatly increased when going from negative to positive potentials. In the 2D IR spectra, there is a large decrease in the red side of the difference spectrum, but only a small increase on the blue side. These differences demonstrate that the FTIR and 2D IR spectroelectrochemical measurements highlight different aspects of the changes in the spectrum in response to the potential, the details of which are discussed in the next section.

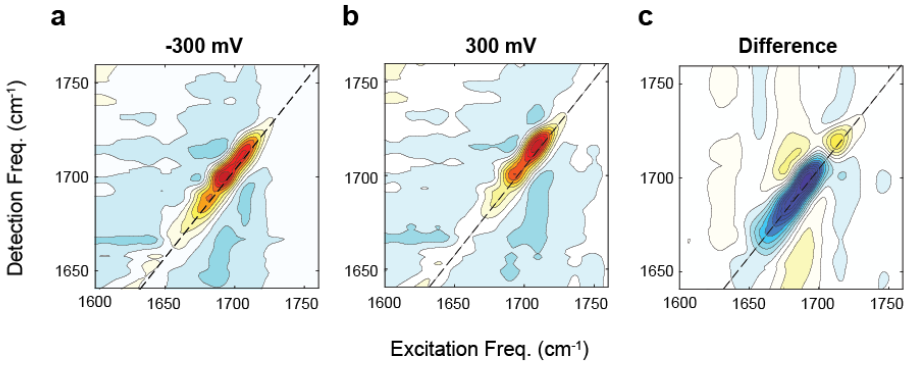

Figure 5.4: 2D IR spectra of MCB on 10 nm Au layered on 1.2 nm Al_2O_3 and 20nm ITO on Si ATR wafers are shown in panels (a) and (b) at -300 mV and 300 mV vs Ag/AgCl reference electrode, respectively, with 100 mM KCl supporting electrolyte in D_2O. The difference spectrum of -300 mV subtracted off 300 mV is shown in panel (c).

5.3.3 Potential and Plasmon Effects on Lineshape

In the previous section we established that there are significant changes in the MCB spectra dependent on the applied potential and the surface morphology of the plasmonic layer. In order to describe these effects qualitatively, we compared the MCB spectra to another monolayer, 4-mercapto-4-methyl-2-pentanone (4MMP). The observed differences in the FTIR spectra as a function of potential could be captured by the phenomenological

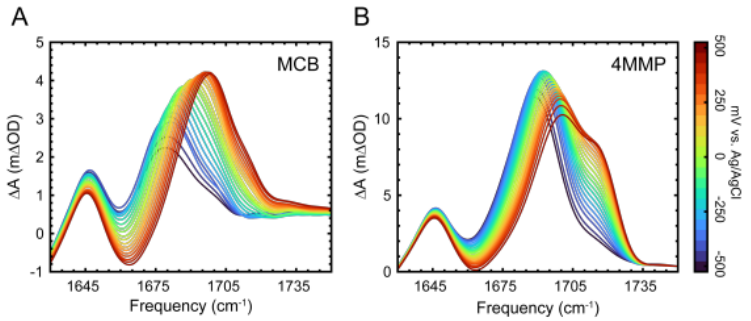

Figure 5.5: FTIR spectra of A. MCB and B. 4MMP monolayers as a function of potential. These spectra were obtained by measuring the FTIR spectra between 500 and 500 mV referenced against 0 mV vs. Ag/AgCl then holding the potential at 750 mV to desorb the monolayers and subtracting the spectra of the bleach of the monolayer subsequent to desorption from the potential dependent difference spectra. We assign the response at 1645 cm^1 to water that is adsorbed into the electrode material which is also removed during the desorption of the monolayers, and note that it does not contribute measurably to the potential dependent difference spectra.

model detailed elsewhere[121], but in summary couples the vibration (Morse potential) to the plasmon (harmonic oscillator) in separate baths, with the electric potential added as a constant offset to the Morse potential, and variable coupling between the vibration and plasmon.

Figure 5.5 shows the difference FTIR of MCB and 4MMP, with 0 mV taken as the background. We see that for MCB there is a broad shoulder in the far blue side of the spectrum, near 1730 cm^{-1} that is not present in the 4MMP case. Additionally, the intensity of the red side is much less than that of the blue side in the MCB case, although this asymmetry is not as pronounced in the 4MMP case. The model qualitatively reproduces these changes, where the more strongly coupled case resembles the MCB experimental spectra, and the lower coupling case more closely resembles the 4MMP case, as shown in Figure 5.6.

We can also compare the MCB 2D IR spectra to the simulated spectra in Figure 5.7, and

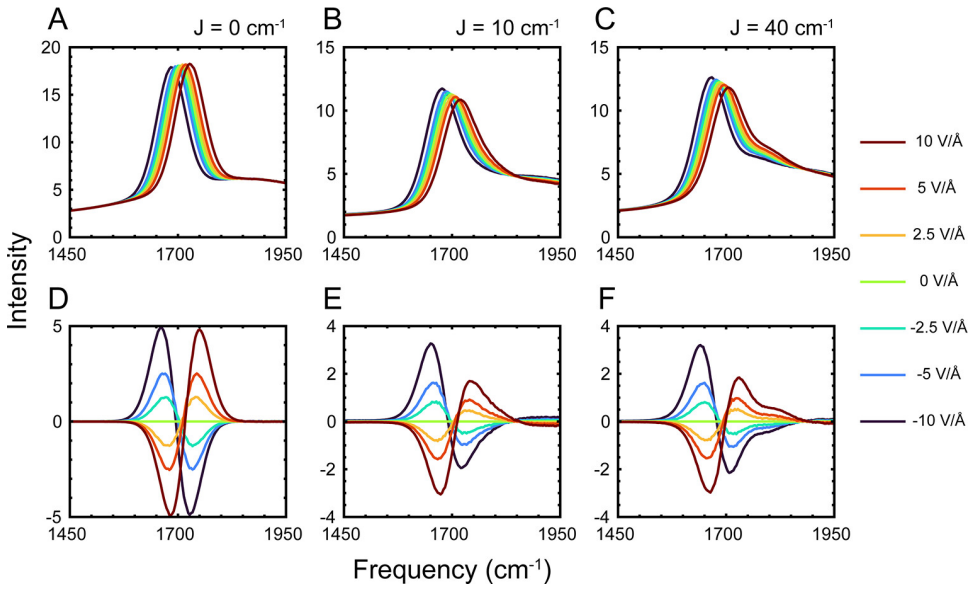

Figure 5.6: Spectral simulation showing the effects of coupling between the vibration and plasmon and the applied field. (A–C) Absorption spectra.(D–F) Difference spectra with respect to E = 0. The unperturbed frequencies are $\omega_{10}^{o} = 1700$ cm^1 for the vibration fundamental transition and $\omega_{p}^{o} = 1850$ cm^1 for the plasmon. The correlation times for the frequency fluctuations are $\tau_v = 1$ ps and $\tau_p = 0.1$ ps.

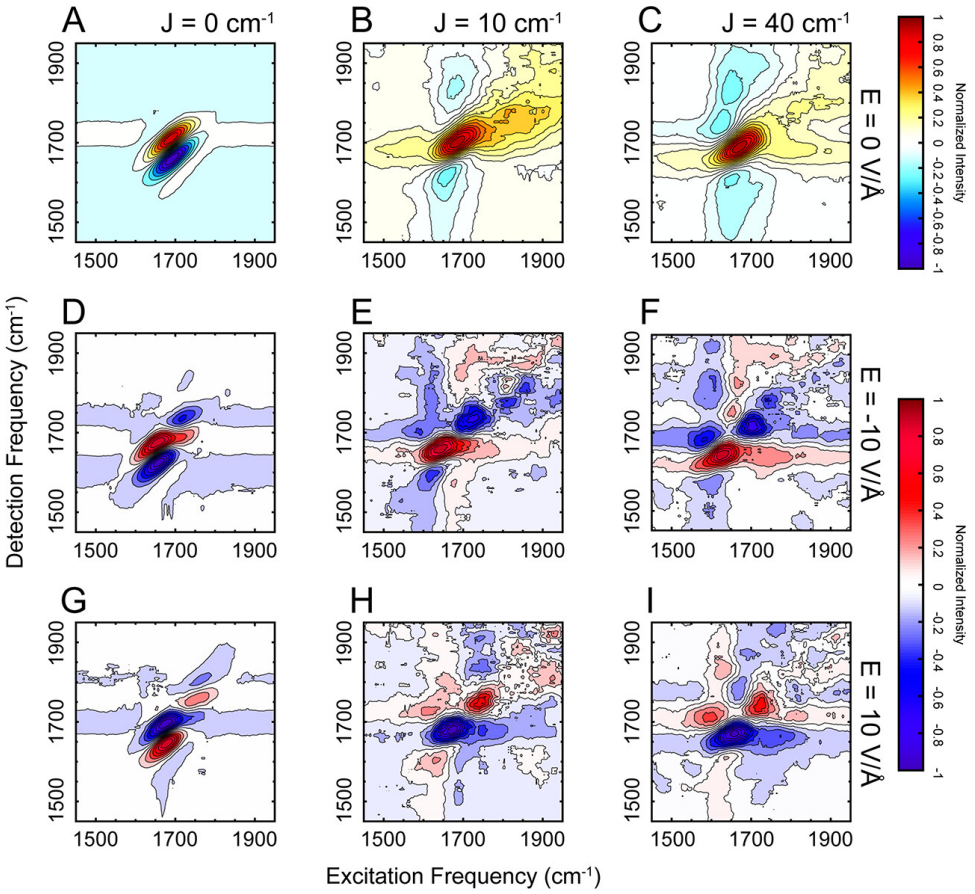

Figure 5.7: Simulated 2D IR spectra as a function of vibration–plasmon coupling and example difference spectra with the applied field. (A–C) 2D IR spectra at E = 0 V/A at J = 0, 10, and 40 cm^1. (D–F) Difference 2D IR spectra at E = – 10 V/A referenced to E = 0 V/A as a function of J. (G–I) Difference 2D IR spectra at E = 10 V/A as a function of J.

we see the the triplet structure along ω_3 axis becomes more prominent with stronger coupling between the vibration and plasmon. Addtionally, we can see in Figure 5.8 that it is contributions from the plasmon-like eigenstates that lead to this triplet structure.

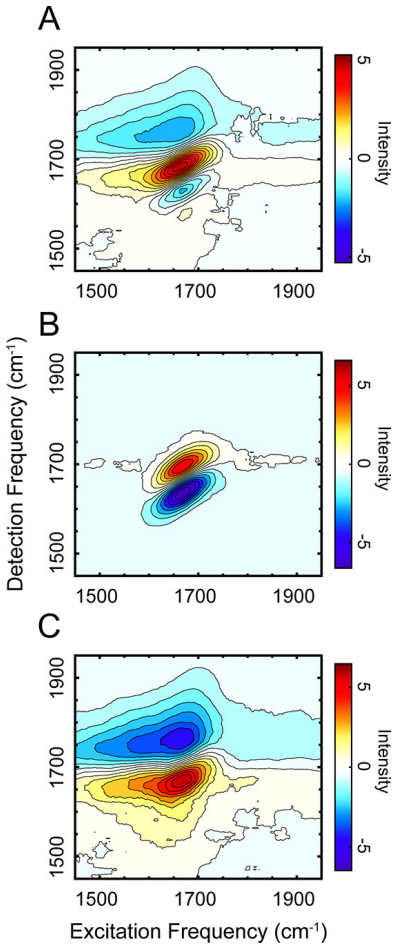

Figure 5.8: Decomposition of the 2D IR simulation for J = 40 cm–1 and E = 0 V/A showing the pathways where all of the interactions are with the vibration-like eigenstate. (A) Total spectrum for the vibration-like eigenstate. (B) Contribution to these pathways from the pure vibration. (C) Contribution to these pathways from the pure plasmon.

5.4 Concluding Remarks

In this chapter, we have discussed the general considerations and approach for designing and fabricating electrodes optimized for 2D IR spectroelectrochemical measurements with an emphasis on utilizing commercially available substrates and electrochemical cell to increase the accessibility of surface specific ultrafast IR experiments. We have developed a

layered electrode for performing 2D IR spectroelectrochemistry at the electrode-electrolyte interface that uses commercial Si ATR wafers with 20 nm of ITO and 1-2 nm Al_2O_3 grown via ALD, topped with 12 nm of sputtered Au. The ITO serves as the conductive layer for the working electrode, the Al_2O_3 as adhesion layer between the ITO and Au, and the Au provides plasmonic enhancement and that can readily be functionalized with thiols.

For the ketone-thiol studied in this work, MCB, we were able to measure the carbonyl response as a function of applied potential and observed similar trends to previous works in the linear and 2D vibrational response to interfacial electric fields with carbonyl stretches. While the vibrational response appears to shift in frequency linearly with applied field[41,64,101–103], we have also noted that the interfacial structure of the plasmonic film plays a large role in determining the lineshape and degree of phase twist of the vibrational spectra, which leads to complications in interpreting the spectra of surface-bound and coupled vibrational reporters. This structure is dependent both on the average thickness of the plasmonic layer, as well as the underlying substrate. We have also noted sensitivity to changes that occur around E_{pzc} which could provide another experimental tool for understanding how the EDL structures in response to the electrode surface charge.

There are other approaches to studying electrochemical interfaces with 2D IR, namely different experimental geometries and substrate/electrode material choices, which come with intrinsic advantages and disadvantages. A major challenge of doing 2D IR in ATR mode is having to pass through a large amount of prism material. For common ATR materials this becomes a problem because many of the high index of refraction materials are also highly dispersive, or have small band gaps that can lead to large background signals from free carriers that are excited when focusing IR beams into the material. Our approach uses thin Si wafers to minimize dispersion. We observe that it suffers from the

problem of a large free carrier background only at higher pump powers, and is not present in the spectra taken in this paper. CaF_2 has been used as an ATR element[102] to avoid the free carrier problem, but the index of refraction limits the use of the material for systems without concentrated electrolyte solutions, which approach the refractive index of CaF_2.[122] Other groups have avoided ATR mode and instead worked in the transmission geometry or in external reflectance.[64,123]. With these approaches, CaF_2 can be used without concern for the refractive index of the substrate, but with the technical challenge of keeping the path length through the cell sufficiently thin to reduce the solvent background while still thick enough to fit all the components of the electrochemical cell. All of the approaches except for the external reflection also use ITO as a conductive layer in addition to a plasmonic layer. A main reason for using ITO as the conductive layer is keeping the plasmonic layer sufficiently thin that the nanostructure with many small highly plasmonically active gaps is conserved. With external reflection, the absorption of the electrode and plasmonic materials is less of a concern, and the electrode material acts as a reflective mirror for the IR. This simplifies the experiment by allowing gold to be both the electrode and enhancement layer and removing the need for an adhesion layer. However, because the IR reflects externally, it passes through the solvent twice, doubling the absorption relative to a transmission cell of the same path length, exacerbating the background signal issue. Overall, we believe that ATR mode with layered electrodes provides the most flexibility for a variety of future experiments. While we expect the electrode material used in our samples can be readily changed to study specific systems of interest, there is the unaddressed issue of the limits of using Au as the plasmonic material and the functionalizable material. This limits any tethered vibrational probes to ones that can coordinate with Au, such as thiols, which have low stability at longer chain lengths due to

polymerization when also containing functional groups that can act as reporters such as amines, carbonyls, and nitriles. Other functional groups that can coordinate with Au are citrates, which contain carbonyls that obscure the desired response from carbonyls positioned within the double layer, or amines, which coordinate much more weakly than either thiols or citrates.[124] A possible solution to this constrains is the additional ALD layer such as Al_2O_3 on top of the Au that can be functionalized by other functional groups, such as silanes, and is sufficiently thin to allow for the plasmonic enhancement. The extensive library of commercially available silanes would open up a wider range of possible experiments, such as using varying chain lengths to extend the probe throughout the electric double layer to investigate how the rapidly changing electric field affects the hydrogen bonding and ion solvation structure and dynamics.[103]

The range of surface reactions that can be employed to build the required layers for electrochemical studies is very broad, and we hope that the general approach outlined in this chapter can be utilized to study the wide range of interfacial electrochemical systems that have broad applicability, such as in areas of energy storage and heterogeneous catalysis where molecular catalysts can be readily used or modified to serve as interfacial vibrational probes. At electrochemical interfaces, the reorganization of the solvent in the electric double layer plays a large role in accommodating charge transfer processes that occur at the interface.[125] The ability of solvent to reorient is strongly dependent on the strength of the interfacial electric field. We hope to directly probe the water structure and dynamics with electrochemical 2D IR to contribute to the understanding of how the water and ions in the EDL impact electrochemical performance.

Chapter 6

Characterizing Carbonyls at the Solid-liquid Interface

6.1 Introduction

The study of interfacial phenomena is pivotal in various fields, including electrochemistry, catalysis, and surface science.[126–128] Classical continuum theories, such as the Gouy-Chapman-Stern model, have long provided a foundational understanding of the electric double layer (EDL) at charged interfaces.[21–24] These models describe the distribution of ions near a charged surface and predict the potential drop across the EDL. While these theories have been instrumental in advancing our understanding of interfacial electrostatics, they possess inherent limitations. Notably, they often fail to capture the molecular-level intricacies and dynamic behaviors of solvated interfaces.[25–27] Such shortcomings include the inability to accurately represent specific ion effects, solvation structure variations, and the complex interplay between surface-bound species and their immediate environment.

In this context, our study aims to bridge the gap between classical theories and

molecular-level phenomena by utilizing ultrafast two-dimensional infrared (2D IR) spectroscopy. Our investigation focuses on two main aspects: the solvatochromism of MCB monolayers and the electrochemical behavior of 4MMP monolayers. By analyzing the spectral shifts, vibrational lifetimes, and coupling phenomena in these systems, we seek to unravel the complexities of interfacial interactions that classical theories often overlook. Specifically, we aim to address how the local environment and solvent dynamics influence the behavior of surface-bound molecules, and how these effects manifest in spectroscopic signatures. In this chapter, we note that while our experiments show sensitivity to the surface phenomena, the results presented also highlight the importance of combining experimental techniques with theoretical studies to achieve a more accurate and detailed picture of interfacial phenomena. Currently, this chapter focuses on the potential ways the experiments could be sensing the interfacial solvation structure rather than a detailed molecular structure due to lack of theoretical studies.

6.2 Methods

Linear absorption spectra were measured with a Bruker Tensor 70 Fourier transform IR spectrometer with a variable angle attachment for the ATR measurements (Pike, VeeMax III), set to 50° angle of incidence.

For CaF_2 substrates, all spectra were measured in transmission mode using two CaF_2 windows with a 6 μm spacer to reduce the solvent background from D_2O while keeping the windows from incidental contact that could damage the Au thin film. Only the first CaF_2 window in the beam path was coated to reduce reflection losses and interference from back-reflection off of a second Au film. For CaF_2 FTIR measurements the background

spectra were collected of air with the cell removed.

Electrochemical 2D IR spectra were taken as detailed in Chapter 5. Briefly, the ITO/Al_2O_3/Au/thiol monolayer samples on top of the Si ATR wafers were used as the working electrode in a Jackfish J2 Spectroelectrochemical cell with a Ag/AgCl (3 M KCl) reference electrode and Pt wire counter electrode. The Si ATR wafers are designed to be compatible with the Jackfish cell and are assembled as per the manual. A potentiostat (Gamry, Interface 1010E) was used to control the electrochemical potential of the sample. Ultrafast 2D IR measurements were taken in the pump-probe geometry with a custom built spectrometer described in detail elsewhere[99] using mid-IR pulses centered at 1700 cm^{-1} with a full-width half maximum bandwidth of 200 cm^{-1}, 15 μJ per pulse, and 100 fs pulse duration. Briefly, the probe pulse is split from the pump using the front face reflection of an uncoated wedged CaF_2 window. The waiting time τ_2 between the pump and the probe is controlled by a delay stage (Aerotech) in the probe beam path. The pump beam is sent through a pulse shaper (Phasetech, Quickshape) which generates a phase-locked pulse pair with controllable delay τ_1 and is used to compensate for dispersion. The probe and pump beams were focused into the sample with 90° off-axis parabolic mirrors. For transmission measurements, the sample was placed directly in the beam focus of a 4 inch focal length mirror (150 μm spot size). For ATR measurements, we used 6 inch focal length mirror (200 μm spot size at normal incidence) with the addition of two gold mirrors to create a 50° angle of incidence onto the ATR prisms. The pump intensity was attenuated ($100 - 200$ nJ per pump pulse) to prevent damage of the gold film and to mitigate the nonresonant response from the ATR element. The change in probe intensity induced by the pump is measured using a spectrograph (Horiba, Triax 190) equipped with a 64 element HgCdTe detector (IR Associates) to obtain the detection frequency axis.

For the transmission 2D IR measurements the pump and probe were set to the *ssss* polarization. To minimize pump scatter contamination of the signal, all 2D IR ATR measurements shown were measured in the cross-polarized *ppss* configuration with the pump *p*-polarized and the probe *s*-polarized with respect to the interface. The polarization of the pump and probe beams were set by $\frac{\lambda}{2}$ waveplates (Alphalas) and wire grid polarizers (Thorlabs). The polarization of the detected signal is set to *s* with a wire-grid analyzer placed immediately before the spectrograph.

6.3 Results and Discussion

6.3.1 MCB at the Interface

To begin our discussion at the surface, we look first at the solvatochromism of the MCB monolayer compared to that of MCB in solution. At the interface, the solvent field felt by the MCB carbonyl is different than in bulk solution. This has been observed before, and a model is proposed by Dawlaty et al.[41] that modifies the Onsager reaction field to account for the effect of image dipoles at the interface that reduce the overall field from a given solvent on the vibrational mode of interest.

The Onsager field for solution compared to the surface model for the Onsager field at in interface is shown in Figure 6.1. We see that the field at an interface never goes to zero as it does in the solution model due to the presence of image dipoles induced in the metal from the tethered molecule. This model also predicts that once the refractive index of the solution is less than 2-3, the field at the surface will be greater than that in bulk solution. This model can explain the trends we see for MCB monolayers verses MCB in solution, which are shown in Figure 6.2.

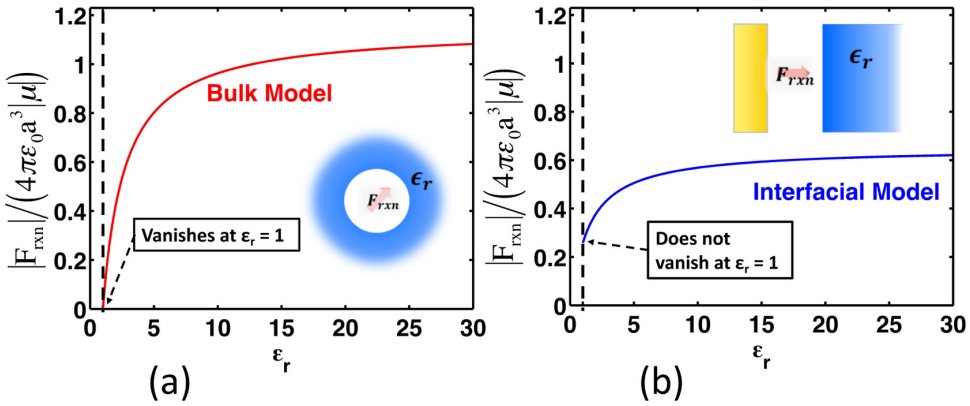

Figure 6.1: (a) Reduced Onsager field for bulk solution model. (b) Reduced Onsager field for interfacial model. (Reprinted with permission from J. Am. Chem. Soc. 2017, 139, 6, 2369–2378. Copyright 2017 American Chemical Society.)

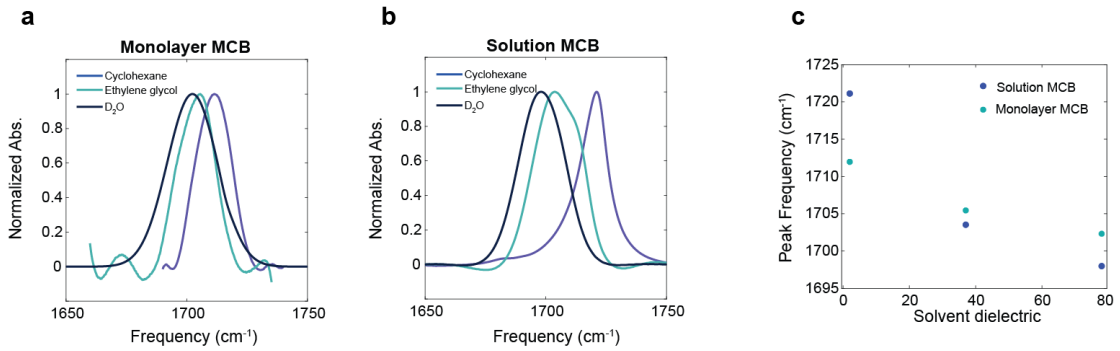

Figure 6.2: FTIR were taken in transmission mode with two sandwiched CaF_2 windows, and background subtracted by fitting either side of the peak with an arbitrary polynomial. (a) Monolayer MCB tethered to an 8 nm thick sputtered gold film on top of one of the CaF_2 windows. (b) MCB in bulk solution. (c) Peak frequency shifts as a function of the solvent dielectric.

In Figure 6.2 (a) we show the transmission 2D IR spectra of MCB tethered to an interface (8 nm sputtered gold on a CaF_2 window) with different solvents. When we compare the frequency shift of MCB monolayers in different solvents to that of MCB in bulk solution, we observe a similar decreased response of the vibrational frequency to the dielectric of the solvent in the monolayer case. We also observe that for cyclohexane the monolayer MCB is

shifted to lower frequencies than the corresponding bulk solution MCB. This can also be explained by the surface Onsager model, where at low solvent dielectrics the field from the image dipoles in the metal contributes to the Onsager field, keeping it from approaching zero.

The 2D IR spectra of MCB monolayers with different solvents were also measured and are compared to the corresponding FTIR spectra in Figure 6.3 by taking both the pump slice amplitudes (PSA) and the diagonal slices. We observe wider peak widths in the 2D IR spectra of the MCB monolayer compared to the FTIR of the MCB monolayer, especially on the red side of the spectrum. This could be due to generally more enhancement that is expected in the 2D IR case, but also due to non-Condon effects that lead to the red side of the spectrum being comparatively broader than the blue side for the 2D IR compared to the FTIR.[129] For the PSAs, the blue side of the spectrum also appears wider, but this is an artifact from the broad negative feature which is illustrated by comparing to the diagonal slices that only appear broadened on the red side of the spectrum. The 2D IR spectrum also is collected using polarized light, although for transmission spectra of a heterogeneous surface this should not lead to significant differences in the types of populations that are sampled.

The same triplet negative-positive-negative structure along the ω_3 axis is observed in the 2D IR spectra that is attributed to vibration/plasmon coupling. In Chapter 4, we observed that the degree of distortion along ω_3 was related to the thickness of the sputtered gold film, and in Chapter 5 we attributed this to the degree of coupling between the vibrational mode and the plasmon due to shifting of the plasmon resonance with changing surface structure. Here we see that the degree of distortion with different solvents appears to have minimal changes, especially when compared to the changes with changing gold film

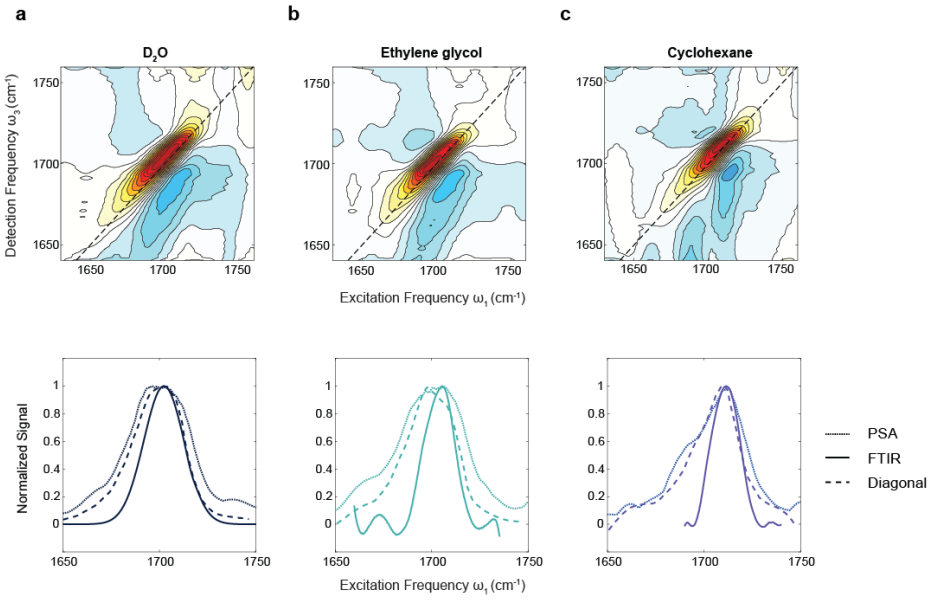

Figure 6.3: 2D IR spectra of MCB carbonyl stretch shown at $t_2 = 0.35$ waiting time under different solvent conditions including (a) D_2O, (b) ethylene glycol, and (c) cyclohexane. Spectra were taken of a MCB monolayer on a sputtered CaF_2 window that was sandwiched with an uncoated CaF_2 window. Lower panels show the pump slice amplitudes (dotted lines) overlaid with the diagonal slices (dashed lines) and FTIR spectra (solid lines) of the corresponding system.

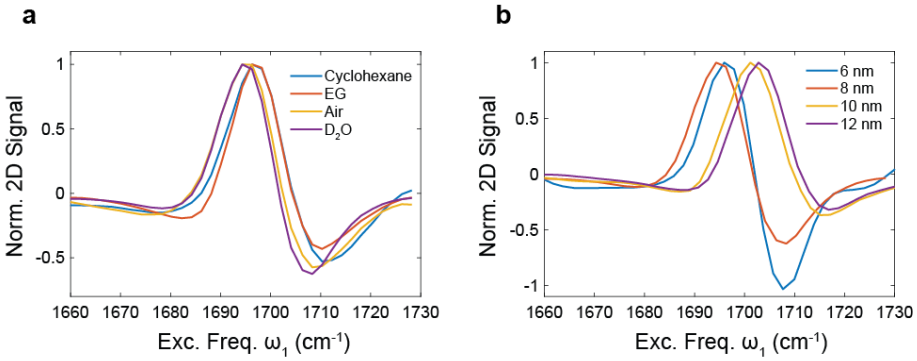

Figure 6.4: Antidiagonal slices taken at early t_2 = 350 fs waiting time and projected along the ω_1 frequency axis. (a) Slices from MCB on 8 nm of Au with varied solvents. (b) Slices from MCB on different Au film thicknesses with D_2O as the solvent. Slices are normalized to the maximum and are taken through the GSB/SE maximum.

thickness. To illustrate this, Figure 6.4 shows the anti-diagonal slices from the 350 fs waiting time 2D IR spectra for monolayers of MCB with (a) changing solvent and (b) changing gold film thickness.

The degree of distortion can be seen in the relative intensities of the GSB/SE and ESA peaks, where for the 6 nm gold film case the distortion is less and the intensities of the peaks are fairly equal. However, as the coupling between the vibration and plasmon increase, the ESA intensity becomes smaller relative to the GSB/SE peak, and the center peak frequency shifts lower onto the diagonal (apparent blue shift when projected onto the ω_1 axis). These changes are seen clearly in the gold film thickness example (2D IR spectra are shown in Figure 6.6), but the changes are more subtle when changing the solvent above the MCB monolayer. This could be due to competing refractive index and dielectric contributions, where both cyclohexane (n = 1.43, ϵ = 2.0) and ethylene glycol (n = 1.43, ϵ = 37) have higher indices of refraction than D_2O (n = 1.33, ϵ = 78), which has a linear relationship to, and redshifts, the plasmon frequency, but lower dielectrics which leads to a narrowing of the resonance compared to D_2O.[130–132] Additionally, the monolayer dielectric

and index of refraction also have an influence on the plasmon resonance and can screen the effects of the solvent[133]. In this case where the solvent effects may be screened, the small changes to the amount of distortion may be due to slight differences in the gold film thickness between samples. For the case where there is no solvent ('Air') above the sample, the antidiagonal slice as well as the center frequency of the GSB/SE peak in the 2D IR spectrum resemble that of the D_2O case. Since these experiments are done at room temperature and pressure, the center frequency similarity can be explained by the expected thin film of water that is present on surfaces under such conditions, while the antidiagonal slice similarity could be due to the thin film of water or simply due to the MCB monolayer having a larger effect than solvent on the plasmon resonance.[134–136]

To explore the vibrational dynamics of the MCB monolayer, we can look at the 2D IR as a function of waiting time. Example 2D IR spectra of MCB monolayers are shown in Figure 6.5 for the different solvents used to look at the solvatochromism, while Figure 6.6 shows similar 2D IR spectra for MCB monolayers on different thicknesses of gold films. The spectra are shown normalized individually for clarity of the spectral lineshape and lack of CLS decay within the vibrational lifetime of the tethered carbonyl.

While there is no measurable CLS decay, the vibrational lifetime can also indicate changes in the local environment of the vibrational probe, so now we turn to measuring the vibrational lifetime for clues as to how the local environment of the MCB monolayer is changing.

The first possible energy relaxation pathway to consider in our system of vibrationally excited monolayers is equillibration through intramolecular relaxation[137], which since our experiments look at one type of monolayer should be consistent and not change with changes in the solution or gold film thickness. We expect instead to be sensitive to changes

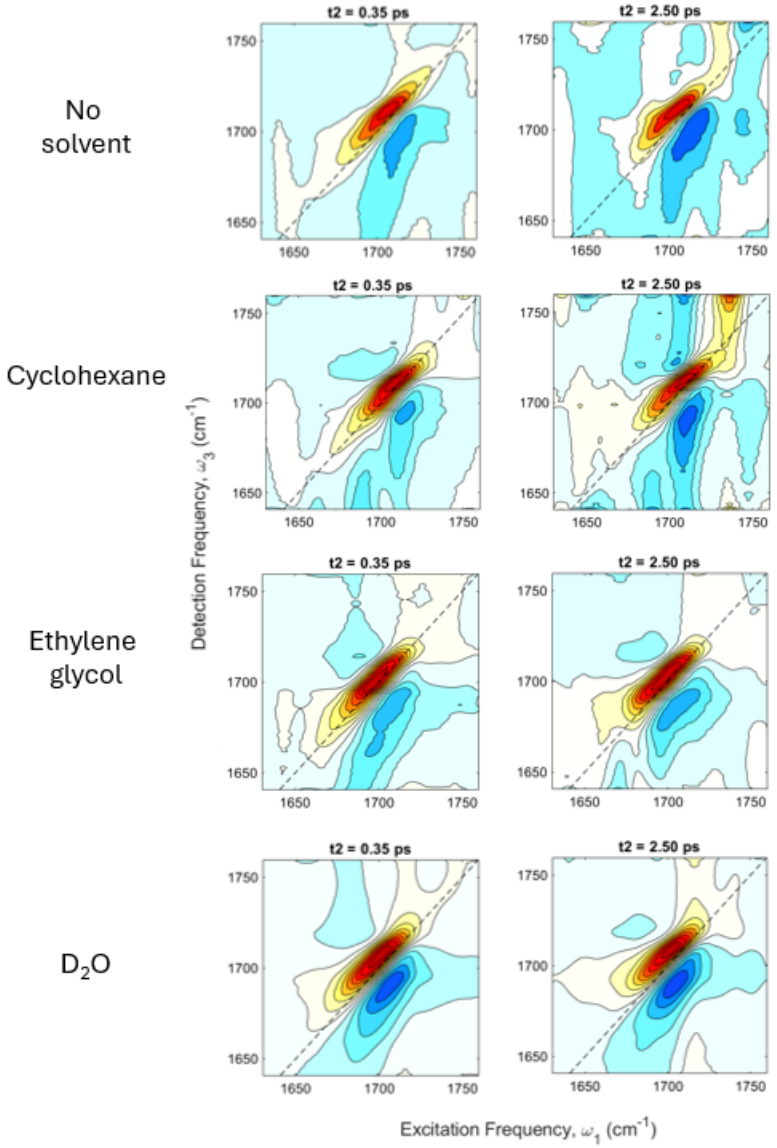

Figure 6.5: 2D IR spectra of MCB carbonyl stretch shown at select (t_2 = 0.35 and 2.5ps) waiting times under different solvent conditions. Spectra were taken of a MCB monolayer on a sputtered CaF_2 window that was sandwiched with an uncoated CaF_2 window.

in the intermolecular environment, of which we can consider hydrogen bonding (HB) interactions and dipole-dipole interactions.[138,139]

For short-chain thiol monolayers on heterogeneous metal films, we can expect them to be

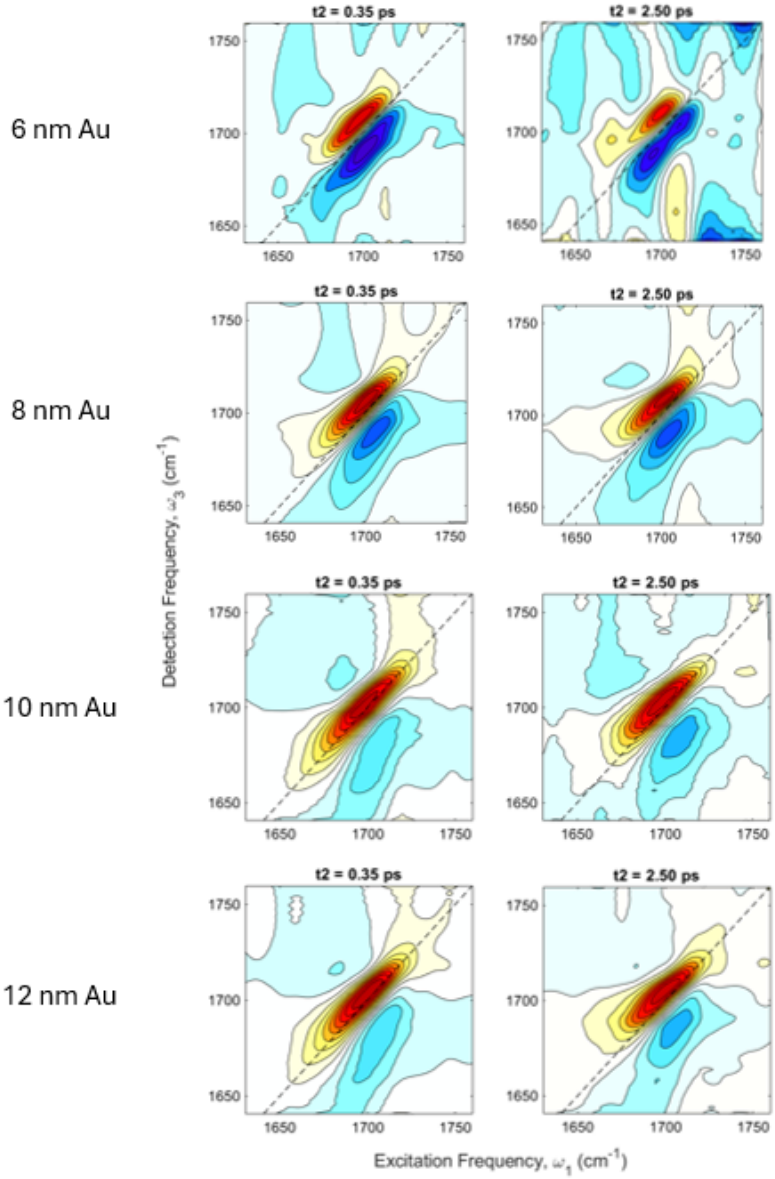

Figure 6.6: 2D IR spectra of MCB carbonyl stretch shown at select (t_2 = 0.35 and 2.5ps) waiting times for 6 nm, 8 nm, 10 nm, and 12 nm Au films with D_2O as the solvent. Spectra were taken with MCB tethered to a sputtered CaF_2 window that was sandwiched with an uncoated CaF_2 window.

quite disordered. As an upper bound, we can look at tightly packed thiol monolayers, which have surface density on gold of around 2.4 molecules nm^{-2}, which gives us a

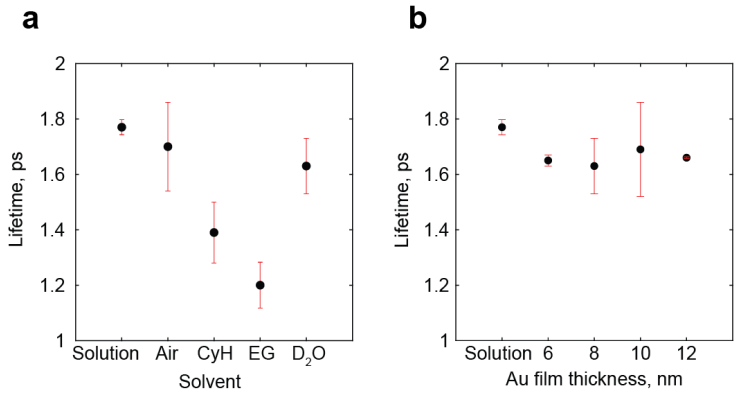

Figure 6.7: Measured vibrational lifetimes of the carbonyl stretch of MCB monolayers with (a) 8 nm sputtered Au and no solvent (Air), cyclohexane (CyH), ethylene glycol (EG) and D_2O. (b) MCB monolayers lifetime with D_2O as a solvent with different thicknesses of sputtered Au. Both (a) and (b) also includes the MCB carbonyl vibrational lifetime for MCB in bulk solution (Solution). To measure the lifetime, the peaks were integrated over a few points at the maximum of the GSB/SE peak and fit to a single exponential decay with an offset. The fits and details are shown and described in more detail in Figure C.13.

minimum distance of 0.6 nm apart.[140,141] Vibrational energy transfer (VET) scales as $1/r^6$ where r is the distance between the two molecules transferring energy. If our monolayer is densely packed, it may be reasonable to assume that we are seeing dipole coupling between the carbonyls and ultrafast energy transfer. However, as a lower bound the estimated coverage for cystamine monolayers on sputtered gold is 0.89 molecules nm^{-2}, which would lead to the molecules being approximately 1.1 nm apart, in which case vibrational energy transfer between two coupled carbonyls is very unlikely to be seen in the 1-2 picosecond lifetime of the carbonyl.[142,143] Instead, we expect changes in the solvation of the monolayer by the solvent to have the largest effect on the vibrational lifetime of the MCB carbonyl stretch. Indeed, we can see that this is the case by the lack of homogeneous broadening within the lifetime of the carbonyl stretch, indicating a longer static environment.

The last considerable influence we might expect on the vibrational lifetime is the strength

of the thiol-Au bond. When a molecule binds covalently to a metal surface, previous studies have shown that the vibrational lifetime decreases due to efficient energy transfer from the excited molecule to the metal.[144,145] This effect can be seen clearly when comparing physisorbed to chemisorbed monolayers, where the vibrational lifetime can be decreased significantly. However, these experiments of MCB in different solvents would be looking for more subtle effects of the bond strength on the vibrational lifetime, which we do not expect to be sensitive to based off previous work by Ziwei Yu and Renee Frontiera that looked at the relationship of the Hammett parameter to the vibrational lifetime of thiol benzyl monolayers and showed no correlation.[146]

Additionally we might anticipate that depending on the nature of the vibration and plasmon coupling, the vibrational lifetime might also be influenced by the strength of the coupling. However, as shown in Figure 6.7 (b), there is no difference to the lifetime as the gold film thickness is changed, even though the coupling changes significantly as illustrated in the diagonal slices in Figure 6.4.

What the vibrational lifetime is sensitive to is the solvent used. This is shown clearly in Figure 6.7 (a), where the vibrational lifetime decreases in order from D_2O > cyclohexane < ethylene glycol. The question now is how the carbonyl solvation is changing between solvents on a molecular scale that leads to these differences in vibrational lifetime. In the following discussion we will not include the no solvent (air) case, due to the water film that makes interpretation of the air sample closer to the D_2O case rather than actually looking at a monolayer with no solvent.

The first major difference between the cyclohexane sample and the other two solvents is the ability of the solvent to HB to the carbonyl. Since HBing is a strong interaction, we expect efficient energy transfer that could potentially decrease the lifetime with increasing

HB strength[137,139]. However, as already noted, the D_2O case actually has the slowest lifetime. Another explanation for the solvent effects is how the solvent changes the angle of the carbonyl relative to the surface, which would may have an effect on the vibrational lifetime. This would also be correlated to the intensity of signal from the monolayer, and we see that the order of intensity is from D_2O > ethylene glycol > cyclohexane (background subtracted spectra without normalization are shown in Figure C.14. However, without being able to correlate the orientation of the monolayer to the spectra, it is unclear how exactly orientation effects would show up in the spectra.

The investigation of the specific solvation structure of the monolayer at the surface is beyond the scope of this thesis and would likely involve complementary MD and systematic experimental results, but for this thesis we point to the conclusion that the complicated interplay between solvent structure, intermolecular interactions of the monolayer, and vibrational/plasmon coupling are much more complicated that continuum theories such as Gouy-Chapman predict, and that experiments of the nature developed in this thesis are key to understanding the complexity at the interface.

6.3.2 4MMP at the Electrochemical Interface

In this next section, we use 4MMP to investigate the changes to the monolayer's solvent environment with applied potentials. We do this by using the layered electrodes described in detail in Chapter 5, which are fabricated on top of thin Si ATR wafers and have 20 nm of ITO as electrode material, 1-2 nm of Al_2O_3 as an adhesion layer, and 12 nm of gold to provide plasmonic enhancement and a base for thiol monolayers. 4MMP is used instead of MCB because of higher observed monolayer stability and slightly higher absorption, both of which become important when subjecting the samples to electrochemical cycling.

In Figure 6.8, we show the 2D IR spectrum of the 4MMP monlayer in 100 mM KCl as a function of potential and t_2 waiting time. We see that as the potential goes from +400 mV to -500 mV, the peak intensity shifts from high frequencies to lower frequencies. This shifting of intensity also appears to be a re-weighting of separate, but overlapping, populations. This can further be illustrated by looking at the diagonal slices at early times, where there appear to be distinct peaks at 1696, 1710, and 1726 cm^{-1}, which are shown in Figure 6.9. Additionally, at the later times we see that there are crosspeaks between the different peaks in the +400 mV spectra. The rise and decay of the crosspeaks are shown in Figure C.15 alongside the 1696 cm^{-1} decay.

There are a few possibilities as to why we see the multi-peak structure and crosspeaks in the 4MMP spectra. The first is that we are looking at different HB environments, where we would expect that each additional HB would redshift the carbonyl frequency approximately 10-12 cm^{-1}.[11,147] This is still less than the frequency separation observed (14 and 16 cm^{-1}), and does not explain the presence of crosspeaks in the +400 mV spectrum, where the switching between HB species is known to be slower than the vibrational lifetime of the 4MMP carbonyl.[148–150] It also does not explain why we would not see separate peaks in the MCB case, nor do we see as dramatic of a shift going from the cyclohexane case to the D_2O case.

We could be observing rotations of the carbonyl, where each peak corresponds to a particular angle between the carbonyl dipole and the surface. However this is unlikely, especially since it should be evidenced by crosspeaks having very different intensities when going from a more parallel (blue shifted) orientation to a more perpendicular (red shifted) orientation due to selection rules at the interface. Additionally, it is unclear why in this picture the different orientations would show up as separated peaks, rather than a

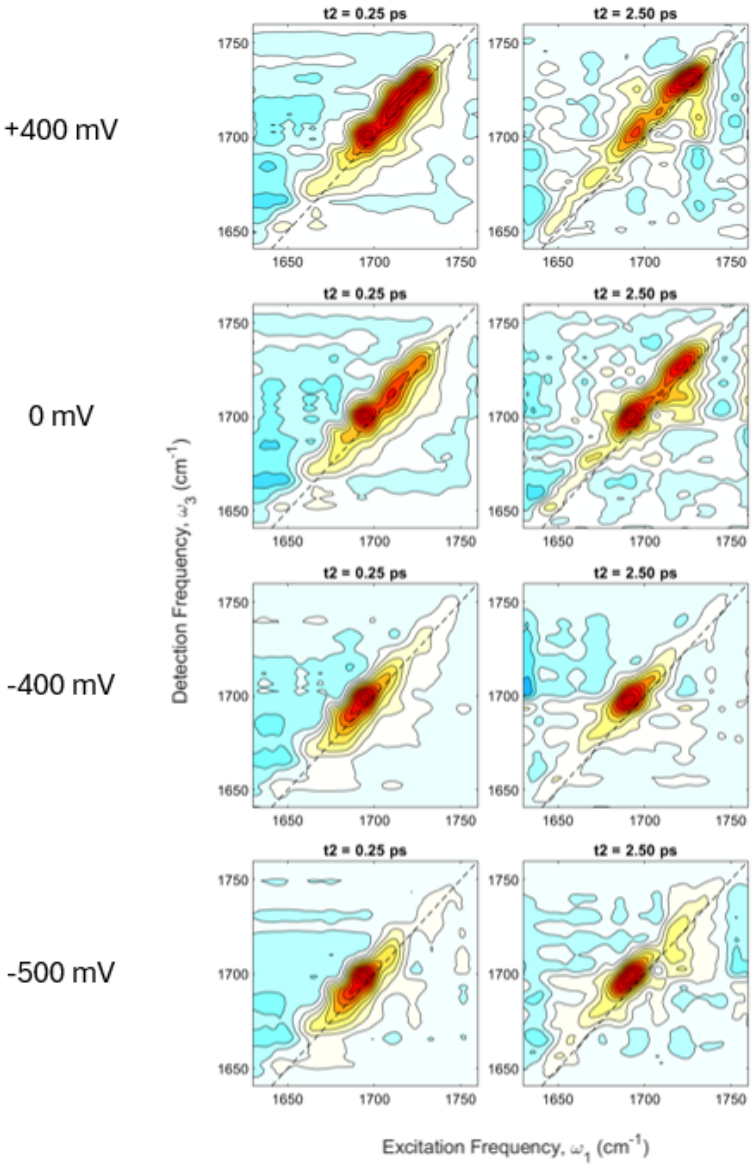

Figure 6.8: ATR 2D IR spectra taken of a 4MMP monolayer as a function of potential and shown for $t_2 = 0.35$ and 2.50 ps. Samples are (from base to solution side) Si ATR wafers, 20 nm ITO(5% Sn), 1-2 nm Al_2O_3, and 12 nm Au functionalized with 4MMP. 100 mM KCl in D_2O is used as the supporting electrolyte, with Ag/AgCl reference electrode and platinum wire counter electrode.

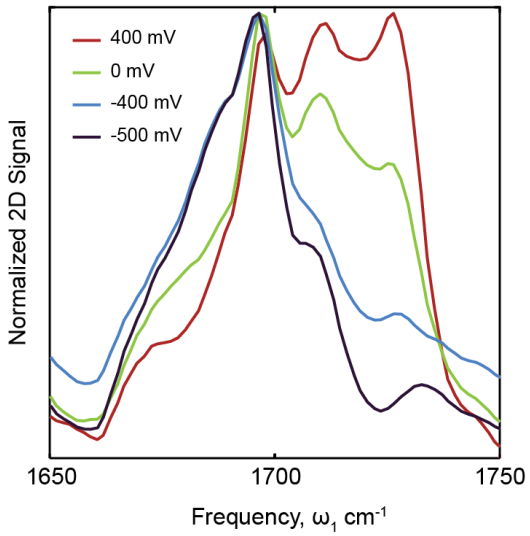

Figure 6.9: Diagonal slices taken from 4MMP 2D IR spectra at early (t_2 = 350 fs) waiting times for different applied potentials and projected along the ω_1 axis. Spectra are individually normalized to their maximum.

broadened lineshape. We also did not observe any crosspeaks in the MCB case with different solvents, which could be due to the shorter chain having less freedom of movement when tethered to the surface. However, in Chapter 5, the 2D IR spectra of MCB in the same electrochemical conditions also showed some peak sub-structure that was unexplained. However, since the multiple peaks only seem to appear in the cases where there are anions present, this points to this being an anion effect.

This leads us to what is the most likely explanation, which is that the peaks are arising from weak interactions with the chloride ions, where due to the partial negative charge of the carbonyl oxygen, even when there is a large concentration of anions at the surface (such as in the +400 mV case), the interaction remains weak enough due to electrostatic repulsion that the different solvation environments can exchange rapidly, leading to the observed crosspeaks.

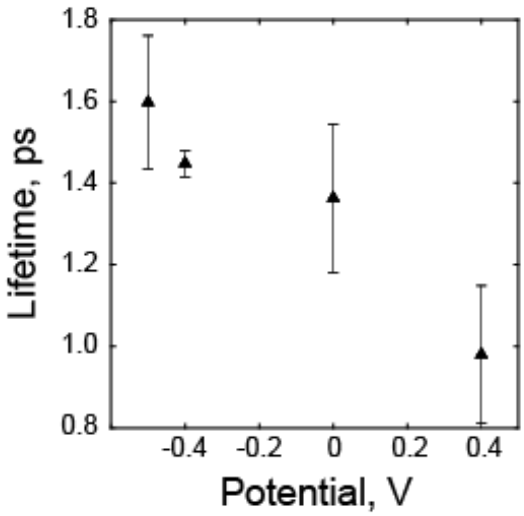

Figure 6.10: Vibrational lifetimes shown with standard deviations taken from three averages for 4MMP monolayers on layered electrodes with 100 mM KCl in D_2O supporting electrolyte and Ag/AgCl reference electrode.

However, this picture does not include an explanation for why the lifetime of the 1696 cm^{-1} peak increases as the potential becomes more negative. This change in lifetime with electric field has been recently been correlated in the case of different solvents by Lu Wei's group.[9] However, the case of water was not looked at in that study, and due to our observations of the changes in lifetime of MCB in D_2O not matching the general trend observed for other solvents, it is likely that there are much more complex effects than just electric field on our spectra. Additionally, to compare our results to the study done in Lu Wei's group, we would be assuming that the solvent field is comparable to the electric field from a surface potential, which has yet to be shown to be the case. If we accept for a moment the weakly bound anion picture, the 1696 cm^{-1} peak would be the population that is solvated by only water. However, there is no significant electrochromic frequency shift in any of the peaks, suggesting that if the weakly bound anion case is true, we are more

sensitive to solvation than the electric field.

6.4 Conclusions

In this chapter we have focused on investigating how the platform developed in Chapter 5 can be used to study interfaces and interfacial phenomena such as building of the electric double layer or interfacial effects on solvent organization. We see changes to the spectra that suggest sensitivity to these phenomena with out platform, but further work is required to correlate spectral changes to molecular level dynamics.

The solvatochromism of MCB monolayers reveals distinct differences between the interfacial environment and bulk solution. The Onsager reaction field model, modified to include image dipoles, effectively explains the observed trends in frequency shifts. The reduced Onsager field at the interface, which never approaches zero due to the presence of image dipoles, accounts for the observed frequency shifts in MCB monolayers compared to MCB in bulk solution.

The 2D IR spectra of MCB monolayers in various solvents showed broader peak widths compared to their FTIR spectra. This broadening, especially on the red side of the spectrum, suggests non-Condon effects and enhanced interactions at the interface. The presence of a triplet negative-positive-negative structure along the ω_3 axis, attributed to vibration/plasmon coupling, remained consistent across different solvents but varied significantly with the thickness of the gold film.

The vibrational dynamics of MCB monolayers, as studied through the 2D IR spectra and vibrational lifetimes, indicate that the local environment and solvent interactions significantly influence the vibrational lifetime. The lack of correlation between the gold film

thickness and vibrational lifetime, despite changes in coupling strength, suggests that the solvent environment plays a more critical role in determining the vibrational relaxation pathways. These findings corroborate the work by Kumar et al.[151] and Harris et al.[152], who demonstrated the impact of surface interactions on vibrational relaxation.

The studies on 4MMP monolayers under varying electrochemical potentials highlighted the impact of the solvent environment and potential-induced changes on the monolayer's behavior. The appearance of distinct peaks and crosspeaks in the 2D IR spectra under different potentials points to complex interactions between the monolayer and the electrolyte ions, particularly chloride ions. The observed multi-peak structure and potential-dependent changes in vibrational lifetimes suggest weak interactions with anions that alter the solvation environment of the monolayer. These results suggest that the platform introduced can extend the understanding of electrochemical interfaces.

Chapter 7

Outlook

A whole thesis devoted to the design of an experiment implies that the experiment is hard - but also worth doing. Throughout this thesis, there has been a strong focus on how hard the challenges faced have been, including the experimental geometry and ATR material (Chapter 2), the importance of selecting an appropriate vibrational probe, the need for enhancement to gain sensitivity to IR monolayers (Chapter 4), the difficulties of designing 2D IR compatible electrodes (Chapter 5), and the difficulty of interpreting the spectra once measured (Chapter 6). In this last chapter, the focus is instead on what we have found the limitations of our experiment to be, and how we might overcome them, starting with potentially using doped Si as an electrode, and potentially designing the plasmonic material to tune the plasmon resonance. Next, the importance of vibrational probe selection is discussed, along with potential ideas for designing vibrational probes. The last section focuses on future experiments that could provide insight into electron transfer at the interface, and the first steps taken.

7.1 Improving Electrode and Plasmonic Material

One limiting factor and challenge to overcome when designing interfacial experiments is achieving monolayer sensitivity. This is hard due to the intrinsically low oscillator strength in the IR, but also because the enhancement from plasmons in the IR is much lower than in the visible due to being largely off-resonant between the plasmon and vibrational modes. Additionally, the use of ATR geometry and multiple layers in the electrode introduce the possibility of additional noise from scattering and reflective losses that can obscure an already small signal. In order to improve the overall design of the experiment and enhance the capabilities, there are two clear avenues. The first is reducing the number of layers used in the electrode, which can be done by doping the top layer of Si in the ATR wafers, which would remove the need for the ITO and possibly the Al_2O_3 layer as well.

The experimental approach to surface-doping the Si uses methods similar to the ones already used in this thesis, and the experimental approach is explained briefly. First, alternating layers of B_2O_3 and Al_2O_3 can be grown via ALD directly on top of the Si. The Al_2O_3 is necessary because B_2O_3 has been shown to have plateaued growth after only a few nm, but linear growth when adding a more reactive Al_2O_3 layer. Due to B_2O_3 degrading when exposed to moisture, Al_2O_3 should be grown as the last few layers on top. Next, the Si can be doped with the boron by rapidly thermally annealing the samples up to 900°C. Afterwards the oxide layers can be removed via wet etching.[153–155]

The second proposed improvement is designing the gold surface to maximize enhancement, which can be done by using designed nanoparticles rather than sputtering, or by using ALD grown gold, which leads to more uniform gold islands with a greater level of control over the size. There are many different ways to fabricate nanoparticles, and only some are cited here. One potential disadvantage of this approach is additional plasmon character in

the spectra, and potentially reduced adhesion if using nanoparticles dried onto the electrode surface.

7.2 Design of Vibrational Probes

As explored in Chapter 3, the selection of vibrational probe can have a large impact on what part of a system can be explored. This was shown through different sensitivities to anions or cations, but also through specific interactions that showed up as whole new peaks, such as MCB and fluoride anions. Additionally, in Chapter 6 we saw that we may be sensitive to the orientation of the monolayer, and that intermolecular effects between thiol molecules may play a large role in the dynamics of the monolayer. This brings up the question of how to control those intermolecular and orientational effects. For intermolecular effects, mixed monolayers or monolayers where the molecule includes bulkier subgroups could be used to reduce potential interaction between neighboring molecules. The orientational effects could be approached by using stiff molecules that due to double bonds or benzene rings cannot rotate the functional group. An example of such a molecule is phenothiazines, although they would need to be modified to add a functional group as a spectroscopic handle, and while these would be a good test system to look at effects of orientation, the polarization effects of a conjugated system have shown to be the major factor in the spectral changes of a monolayer on an electrified interface, and not the changes in the solution environment.[118] Another potential modification can increase the brightness of a vibrational probe by isolating the functional group from the rest of the molecule through the addition of a heavy atom. This has been demonstrated before[10], and may provide another avenue that does not rely as much on tuning the plasmon resonance.

7.3 Ultrafast Electron Transfer

Ultimately, the preferred outcome from designing interfacial electrochemical experiments that can be studied with 2D IR is to observe surface phenomena that cannot be observed currently with other experimental methods. One such phenomena is ultrafast electron transfer that occurs on the picosecond timescale.[156] Such rates are feasible when looking at an ideal electron acceptor tethered to the interface, and efforts have been made to build this system using ferrocene as the electron acceptor, and click chemistry to bind it to the surface and include an amide vibrational probe. The approach is illustrated in Figure 7.1, and currently we have been able to tether the ferrocene to the surface and observe redox peaks through cyclic voltammatry, although currently the brightness of the amide is the limiting factor for observing spectral signatures. This could be addressed by tuning plasmon resonances, or using a probe brighter than the amide.

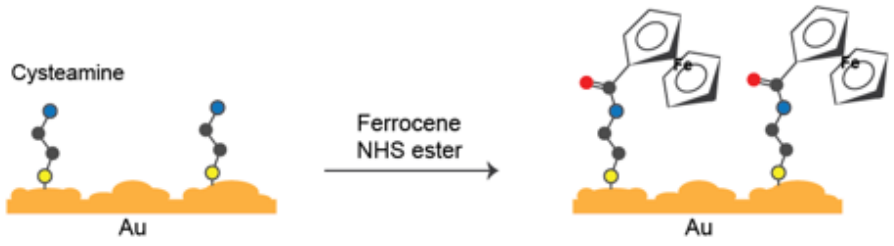

Figure 7.1: Illustration showing the functionalization method used to attach ferrocene to the electrode interface with an amide linker.

Overall, the impression to be left with is the extent of the parameter space when working with electrochemical interfaces. The surface, monolayer, and electrolyte system each play a key role in determining what can be learned from the 2D IR experiments developed in this thesis. Each of those parameters have several others that can be explored, leading to almost endless possibilities for experimental design. What this thesis provides is guidelines

for how to navigate the parameter space, and this chapter provides possible next steps that may be of interest to the broader electrochemical and spectroscopic communities.

Appendix A

Supplementary Information for Chapter 3

Background subtracted and normalized FTIR spectra are shown for all vibrational probes in all electrolyte solutions and concentrations used for analysis in Chapter 3.

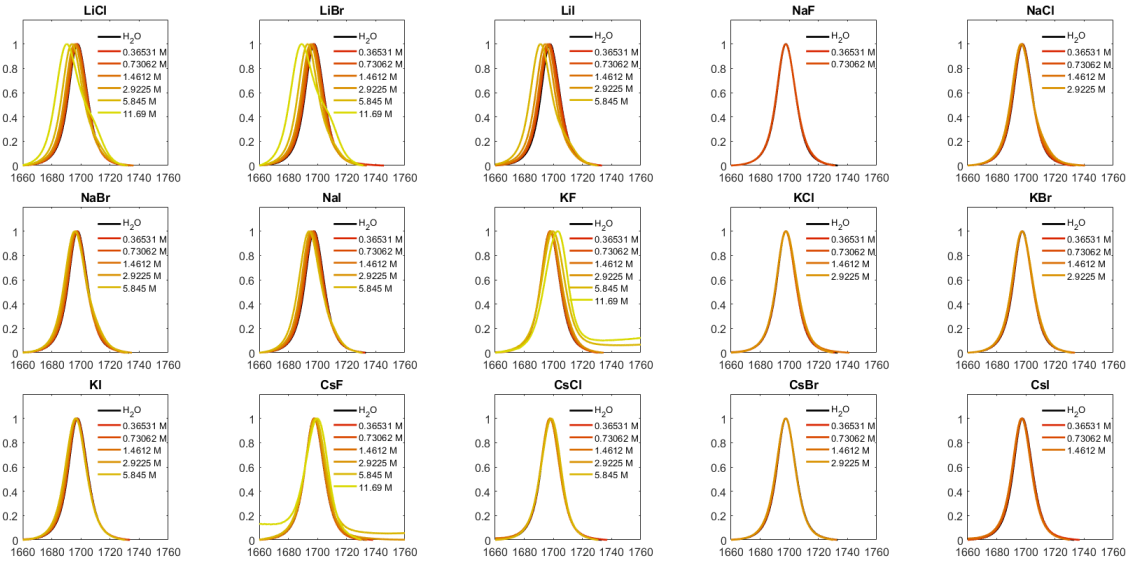

Figure A.1: Background subtracted and normalized FTIR spectra plotted for different salts (marked with title) and concentrations (marked with figure legends) for acetone carbonyl.

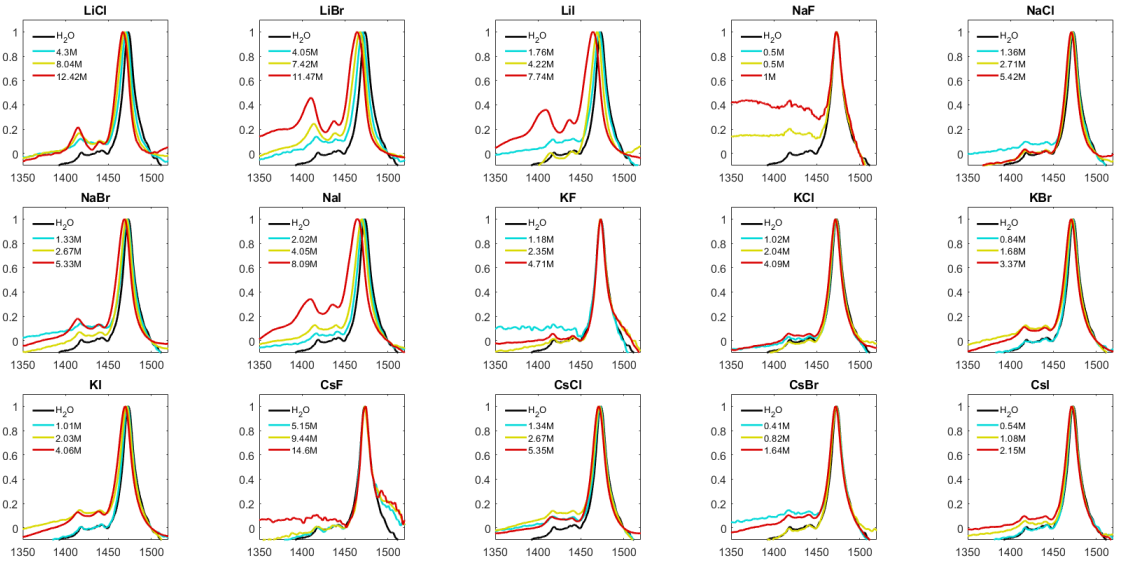

Figure A.2: Background subtracted and normalized FTIR spectra plotted for different salts (marked with title) and concentrations (marked with figure legends) for DMA^+ CH_3.

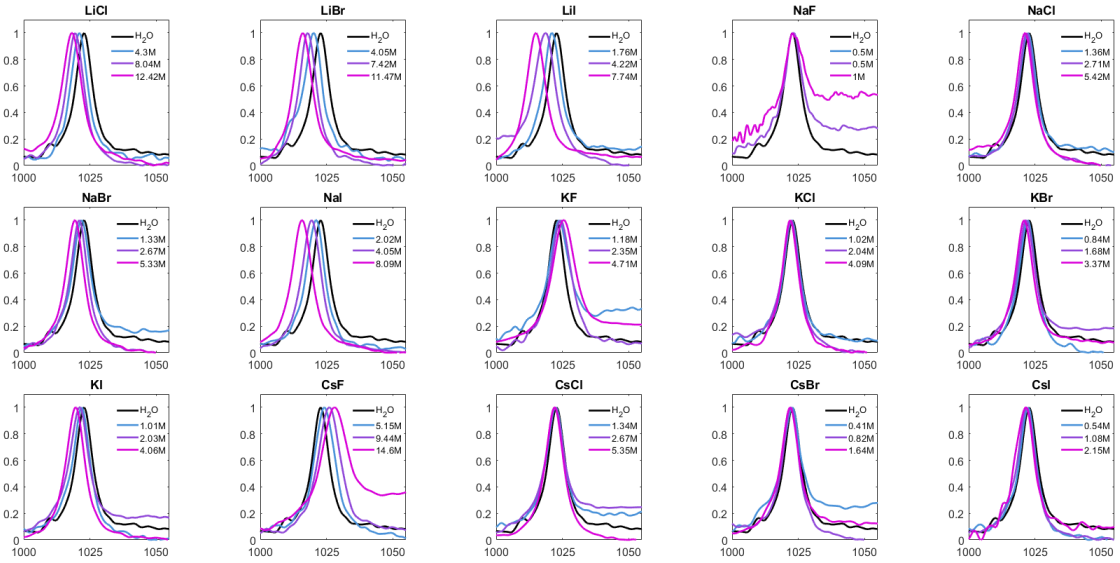

Figure A.3: Background subtracted and normalized FTIR spectra plotted for different salts (marked with title) and concentrations (marked with figure legends) for DMA^+ CNC.

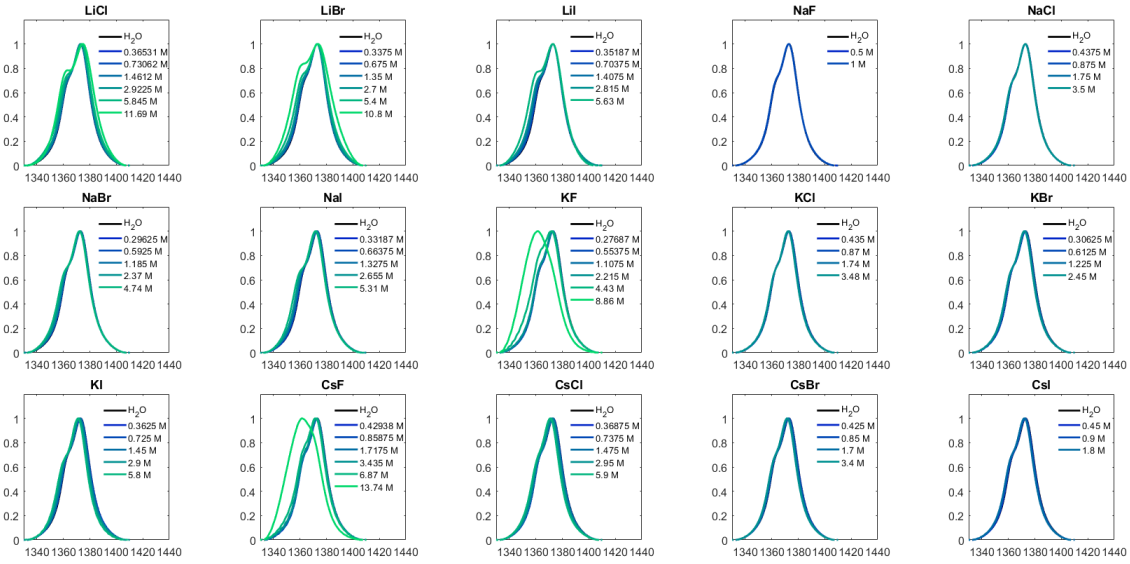

Figure A.4: Background subtracted and normalized FTIR spectra plotted for different salts (marked with title) and concentrations (marked with figure legends) for HOD bend.

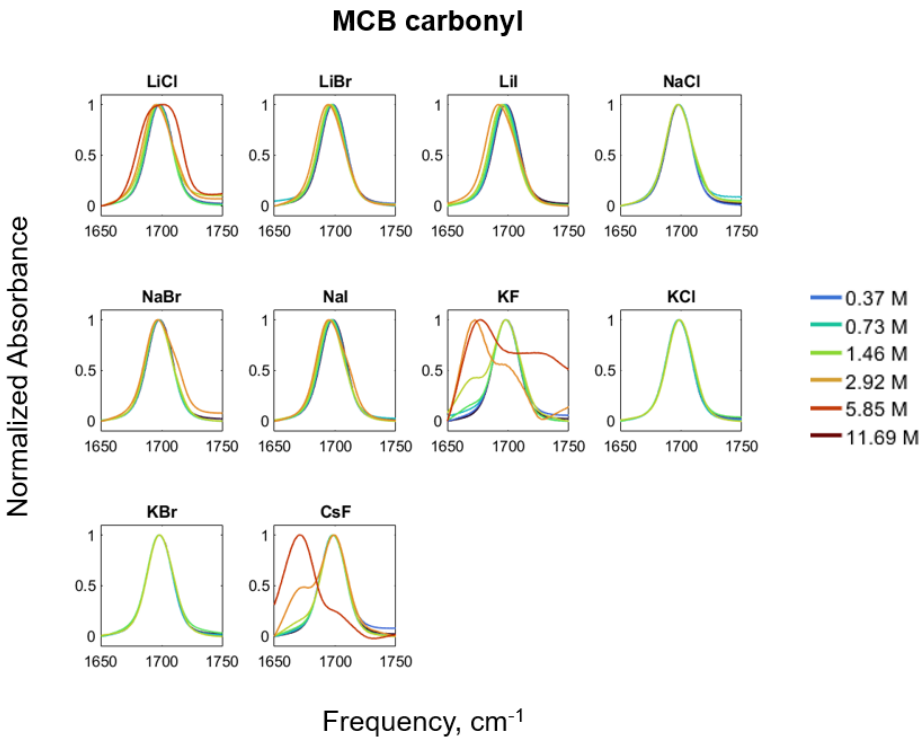

Figure A.5: Background subtracted and normalized FTIR spectra plotted for different salts (marked with title) and concentrations (marked with figure legends) for MCB carbonyl.

Appendix B

Supplementary info for Chapter 5

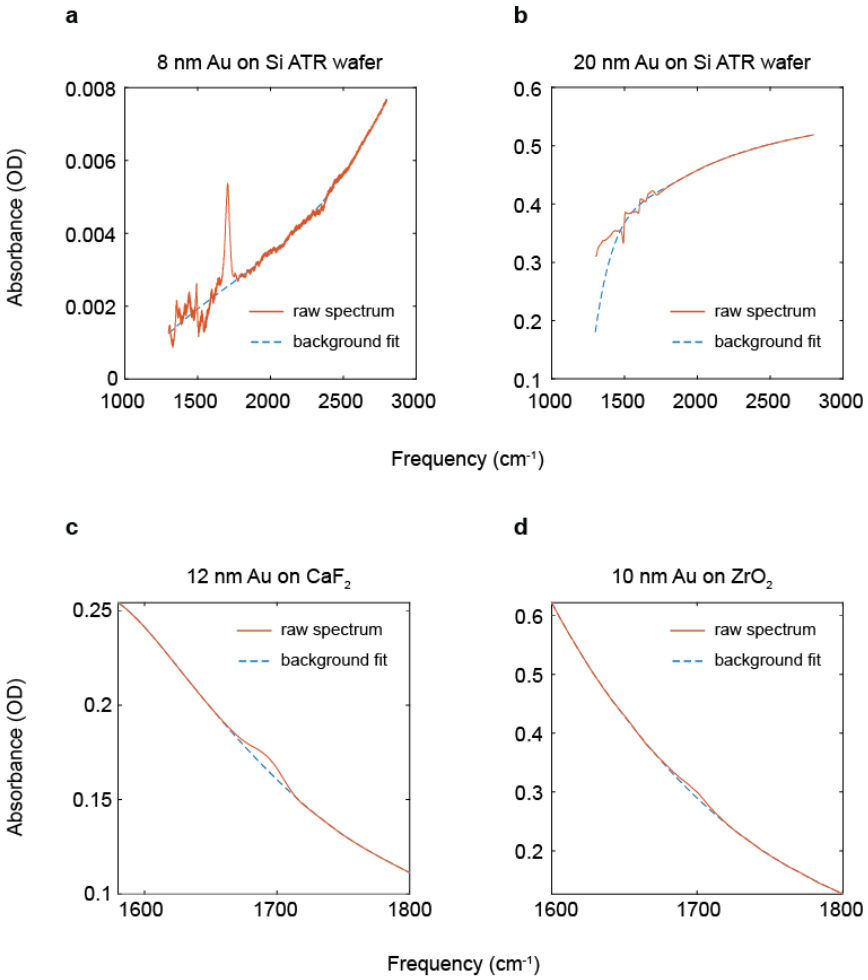

Figure B.1: Raw FTIR spectra and the baseline fitting for MCB functionalized Au films on different substrates. For Si ATR wafer substrates the spectra for 4 and 8 nm Au films were fit with a third order polynomial from 1800 to 2800 cm^{-1} and extrapolated down to 1300 cm^{-1} for background subtraction. (a) An example of the background fitting shown for 8 nm of Au on Si ATR wafers. For thicker films (12 nm and above), the spectra taken with the Si ATR wafers was fit with a seventh order polynomial from 1450 to 2800 cm^{-1}, excluding the region from 1451 to 1850 cm^{-1}. (b) Example of background fitting for 20 nm of Au on Si ATR wafers. For the CaF_2 and ZrO_2 substrates, the background for all spectra regardless of Au film thickness was fit with a sixth order polynomial from 1580 to 1800 cm^{-1} excluding the region from 1670 to 1730 cm^{-1}. (c-d) Example background fitting for 12 nm Au on CaF_2 and 10 nm Au on ZrO_2.

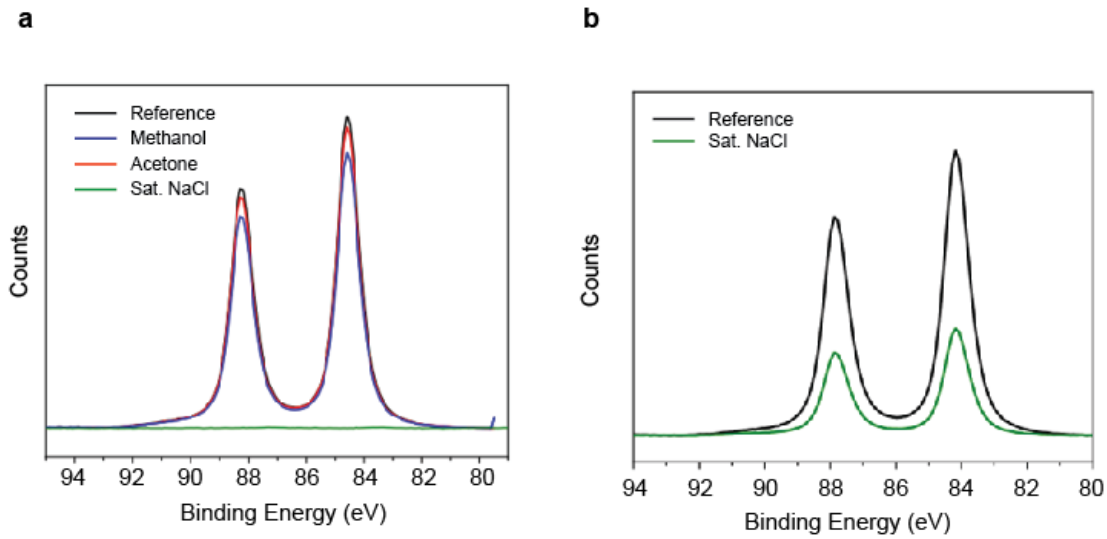

Figure B.2: XPS peaks of Au4f showing the change in peaks for (a) Au on 20nm of ITO and (b) Au on 1.2 nm of ALO on ITO.

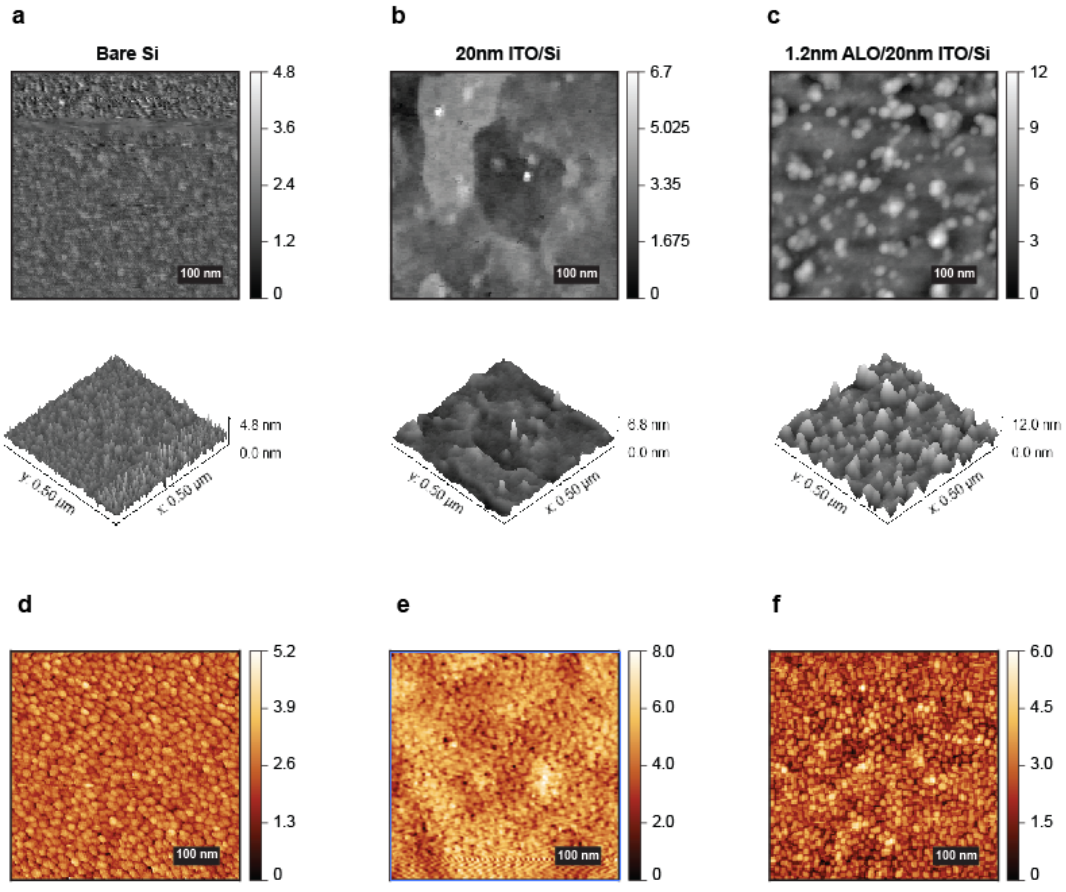

Figure B.3: AFM images of (a) bare Si wafers, (b) 20 nm ITO grown via ALD on Si, and (c) 1.2 nm of ALO grown via ALD on 20 nm of ITO on Si. (d-f) AFM images of the same substrates with 8 nm of Au sputtered on top. The structure of Au is noticeably different on ITO than the other substrates, and forms an interconnected pattern rather than separate islands.

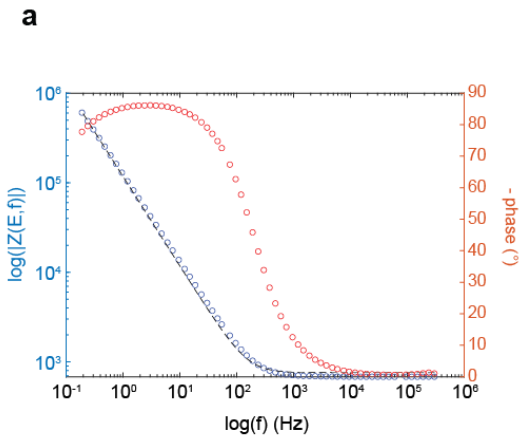

Figure B.4: (a) Example plot of the modulus of impedance, $|Z(E, f)|$, shown on the left y axis as a function of the AC frequency, f, in Hz and corresponding fit shown with the black dashed line. The negative phase is plotted on the right y axis.

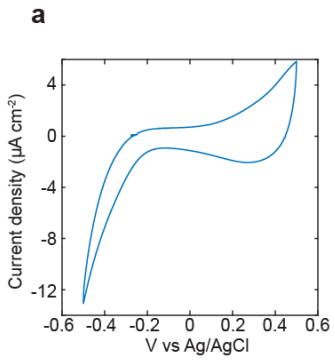

Figure B.5: (a) Cyclic voltammogram of the layered electrode (12 nm Au/1.2 nm Al_2O_3/20 nm ITO on Si ATR wafers) functionalized with MCB. Supporting electrolyte is 100 mM $KClO_4$ in H_2O.

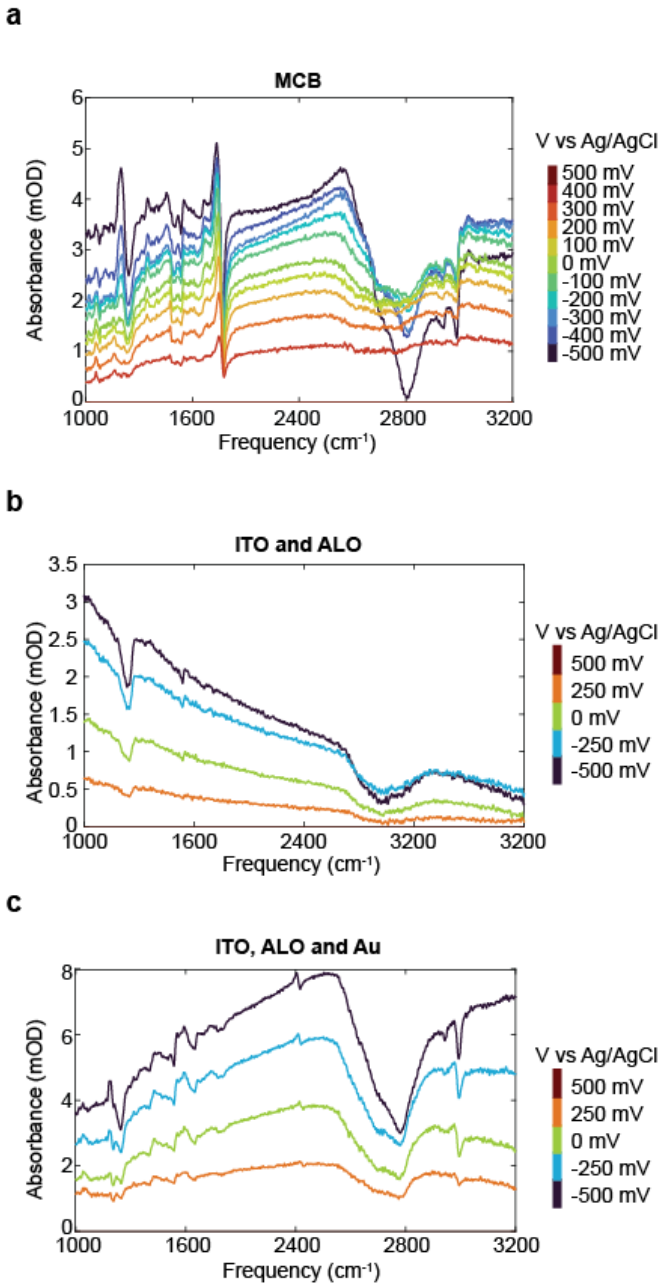

Figure B.6: (a-c) Raw difference spectra shown in reference to the 500 mV spectrum to show the increasing absorbance with more negative potentials. Supporting electrolyte is 100 mM KCl in D_2O. The baseline shift that is in the spectra for the (a) MCB functionalized electrode is shown to also be present in both (b) ITO/ALO samples and (c) ITO/ALO with 12nm of Au. Because it is a material response it is subtracted from the difference spectra shown in the main text for clarity.

Appendix C

Supplementary info for Chapter 6

2D IR spectra that were analyzed for the lifetime results presented in Chapter 6. The integrated peak areas are also shown as well as the lifetime fits for all averaged spectra. The error bars presented in Chapter 6 are taken by fitting each average (3-6) separately and plotting the standard deviation.

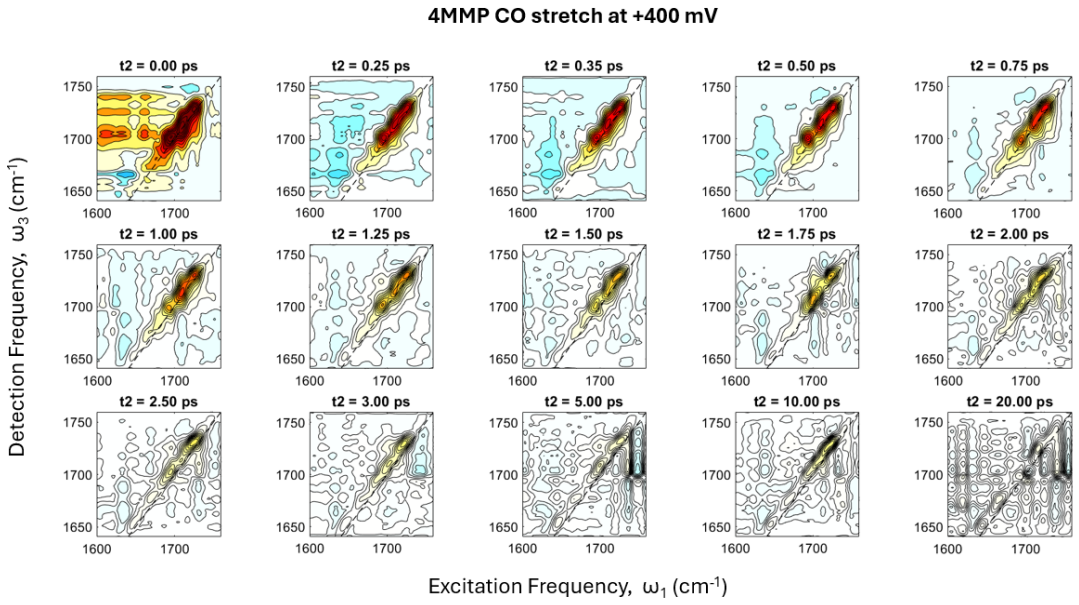

Figure C.1: 2D IR spectra as a function of waiting time t_2 for 4MMP on the layered electrode with 12 nm of sputtered Au and a $+400mV$ vs Ag/AgCl potential applied. Spectra are shown normalized to the second waiting time ($t_2 = 0.25ps$). The spectra at $t_2 = 0ps$ have artifacts arising from Si non-resonant response and are not included in the lifetime fitting. A ghost pulse at $t_2 = 0ps$ artificially enhances the signal at that time and is also excluded from the lifetime fitting.

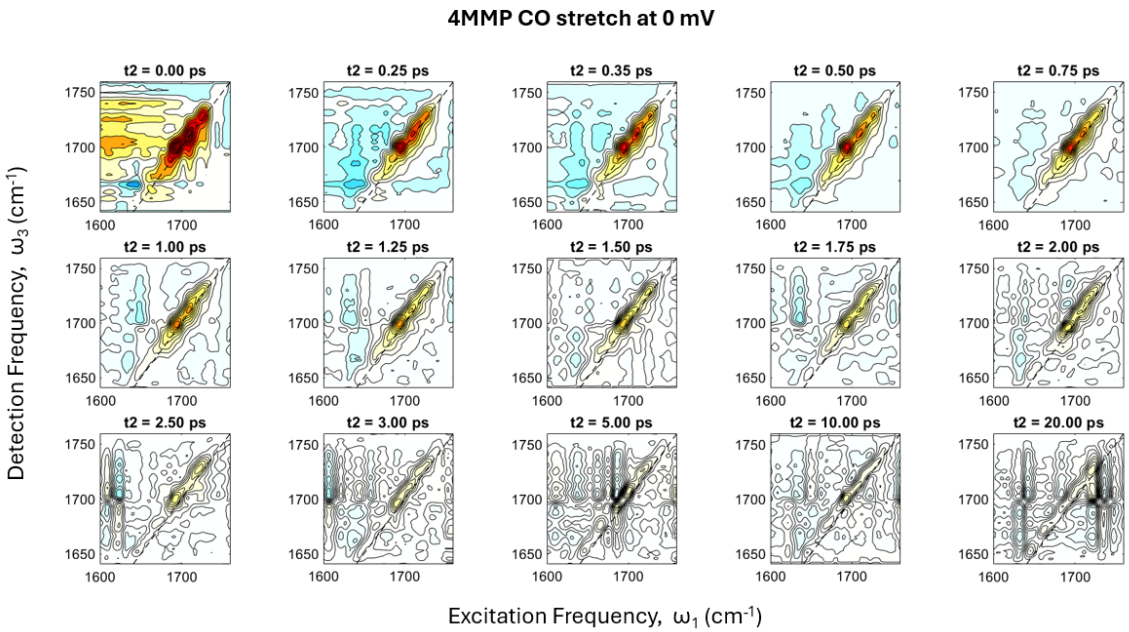

Figure C.2: 2D IR spectra as a function of waiting time t_2 for 4MMP on the layered electrode with 12 nm of sputtered Au and a $0mV$ vs Ag/AgCl potential applied. Spectra are shown normalized to the second waiting time ($t_2 = 0.25ps$). The spectra at $t_2 = 0ps$ have artifacts arising from Si non-resonant response and are not included in the lifetime fitting. A ghost pulse at $t_2 = 0ps$ artificially enhances the signal at that time and is also excluded from the lifetime fitting.

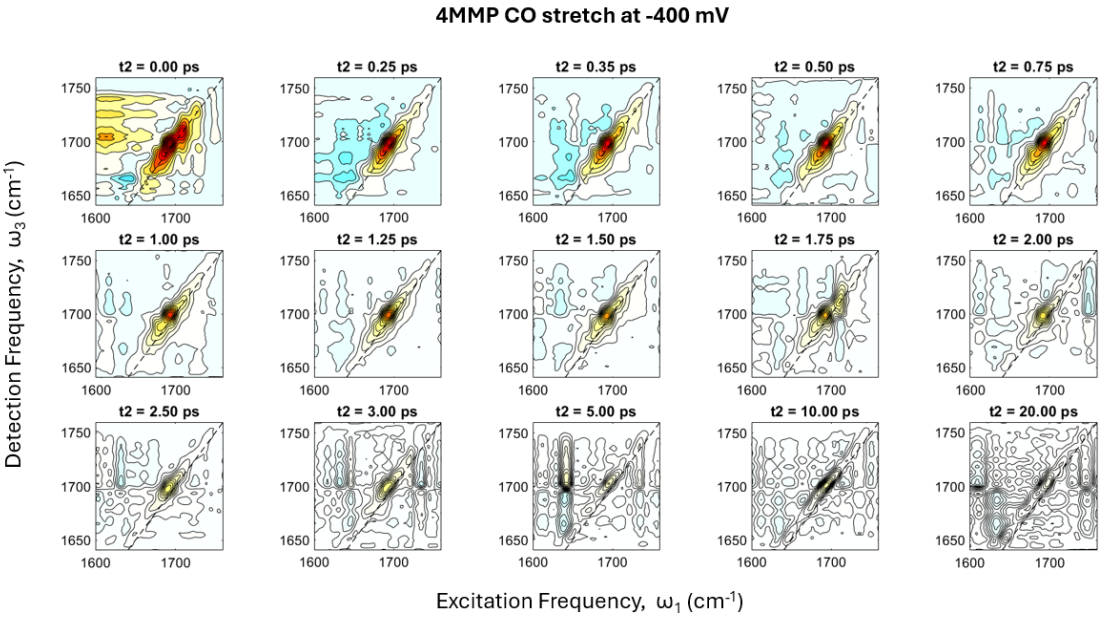

Figure C.3: 2D IR spectra as a function of waiting time t_2 for 4MMP on the layered electrode with 12 nm of sputtered Au and a $-400mV$ vs Ag/AgCl potential applied. Spectra are shown normalized to the second waiting time ($t_2 = 0.25ps$). The spectra at $t_2 = 0ps$ have artifacts arising from Si non-resonant response and are not included in the lifetime fitting. A ghost pulse at $t_2 = 0ps$ artificially enhances the signal at that time and is also excluded from the lifetime fitting.

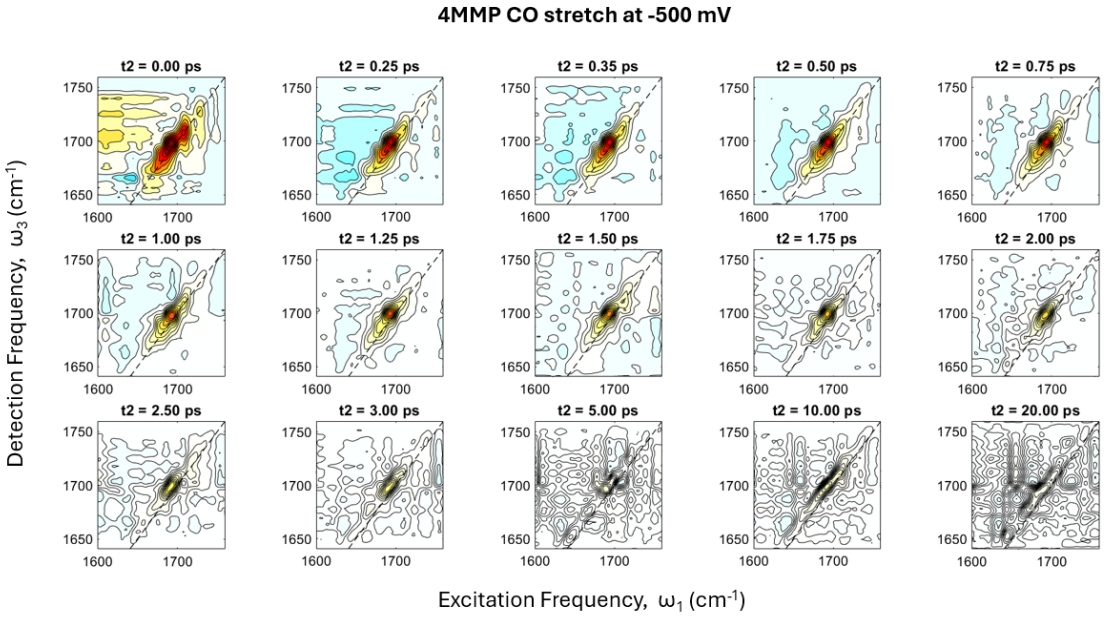

Figure C.4: 2D IR spectra as a function of waiting time t_2 for 4MMP on the layered electrode with 12 nm of sputtered Au and a $-500mV$ vs Ag/AgCl potential applied. Spectra are shown normalized to the second waiting time ($t_2 = 0.25ps$). The spectra at $t_2 = 0ps$ have artifacts arising from Si non-resonant response and are not included in the lifetime fitting. A ghost pulse at $t_2 = 0ps$ artificially enhances the signal at that time and is also excluded from the lifetime fitting.

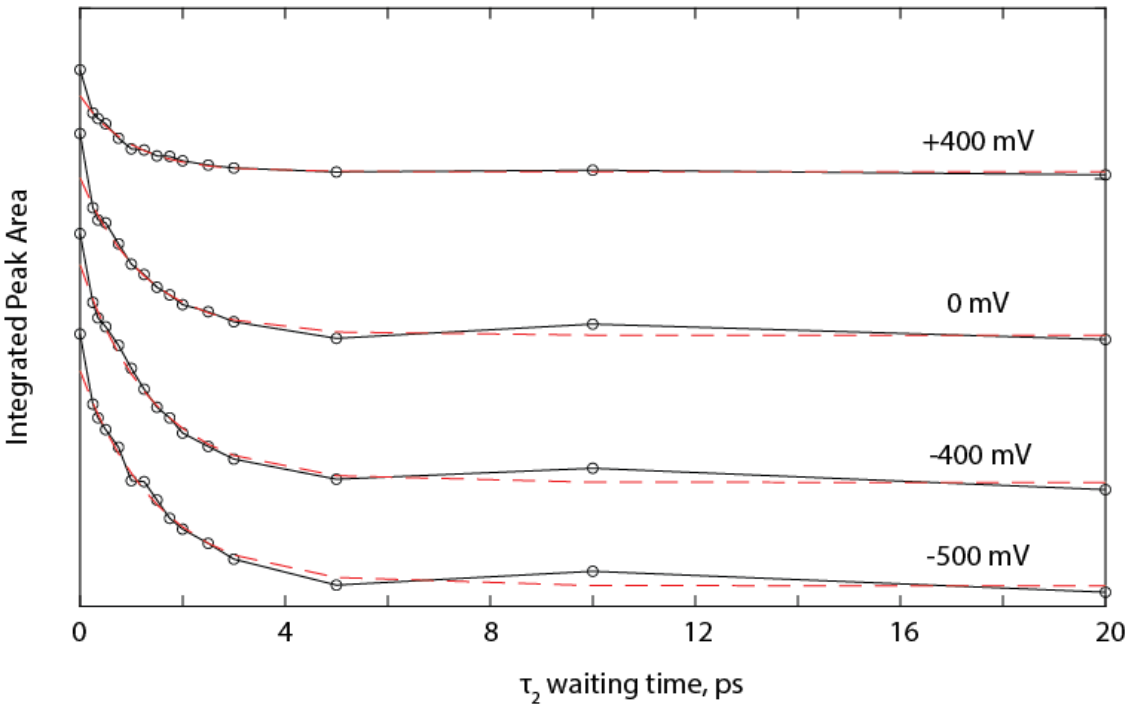

Figure C.5: Lifetime decay shown for averaged 4MMP CO stretch spectra. The decay for each potential is plotted offset for clarity. At more negative potentials the intensity shifts to lower frequency, increasing the intensity of the 1695 cm^{-1} peak that was used for lifetime analysis. The integrated area was taken as a square ± 2 cm^{-1} from the peak maximum on the ω_3 and ω_1 axes. The resulting lifetimes and standard deviation from three averages are discussed in Chapter 6.

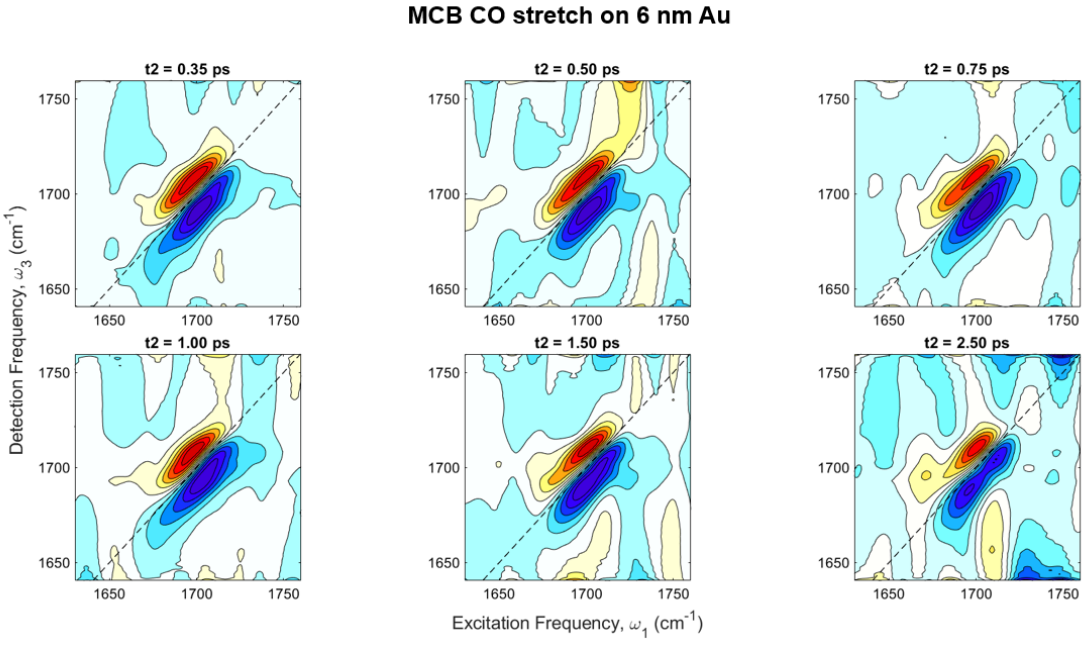

Figure C.6: 2D IR spectra as a function of waiting time t_2 for MCB on 6 nm thick sputtered Au film on a CaF_2 window taken in transmission mode. D_2O was used as the solvent and no spacer was used between the CaF_2 windows. The spectra are individually normalized.

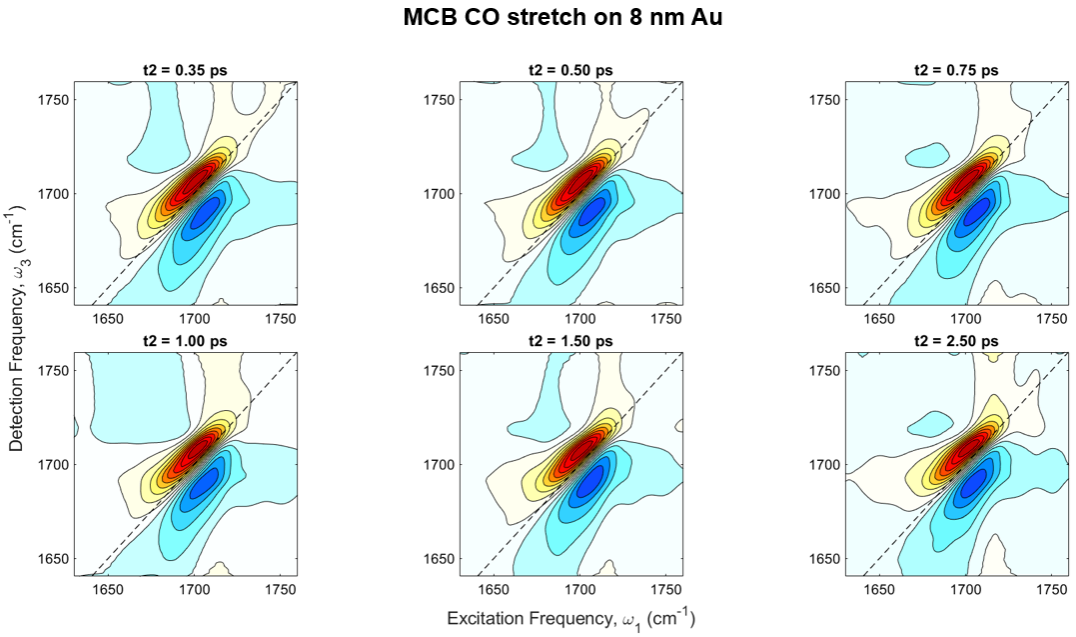

Figure C.7: 2D IR spectra as a function of waiting time t_2 for MCB on 8 nm thick sputtered Au film on a CaF_2 window taken in transmission mode. D_2O was used as the solvent and no spacer was used between the CaF_2 windows. The spectra are individually normalized.

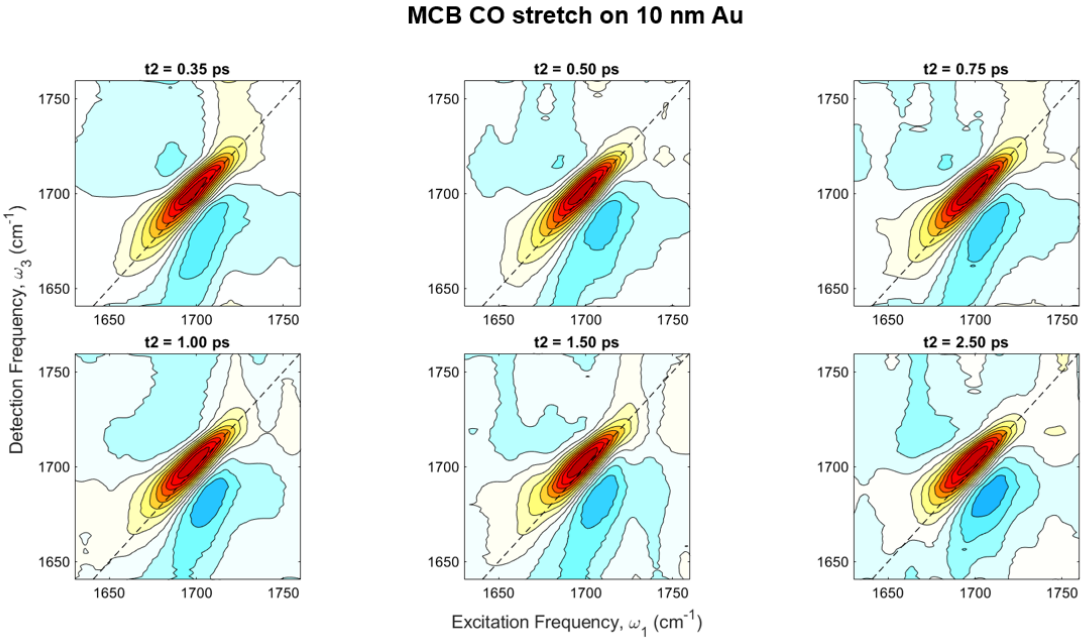

Figure C.8: 2D IR spectra as a function of waiting time t_2 for MCB on 10 nm thick sputtered Au film on a CaF_2 window taken in transmission mode. D_2O was used as the solvent and no spacer was used between the CaF_2 windows. The spectra are individually normalized.

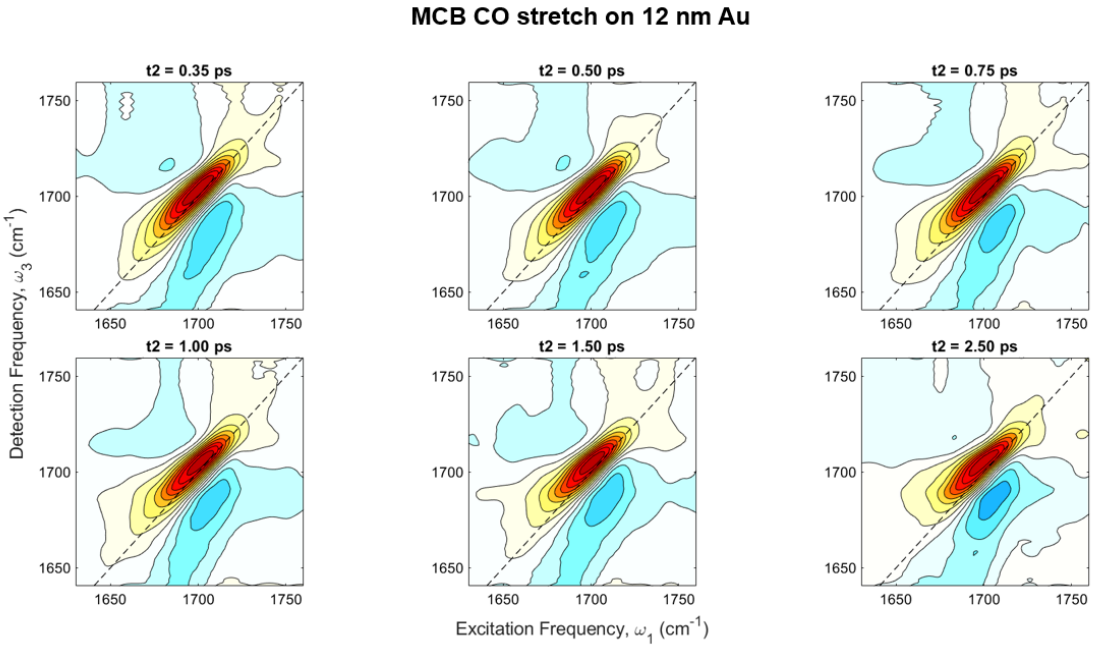

Figure C.9: 2D IR spectra as a function of waiting time t_2 for MCB on 12 nm thick sputtered Au film on a CaF_2 window taken in transmission mode. D_2O was used as the solvent and no spacer was used between the CaF_2 windows. The spectra are individually normalized.

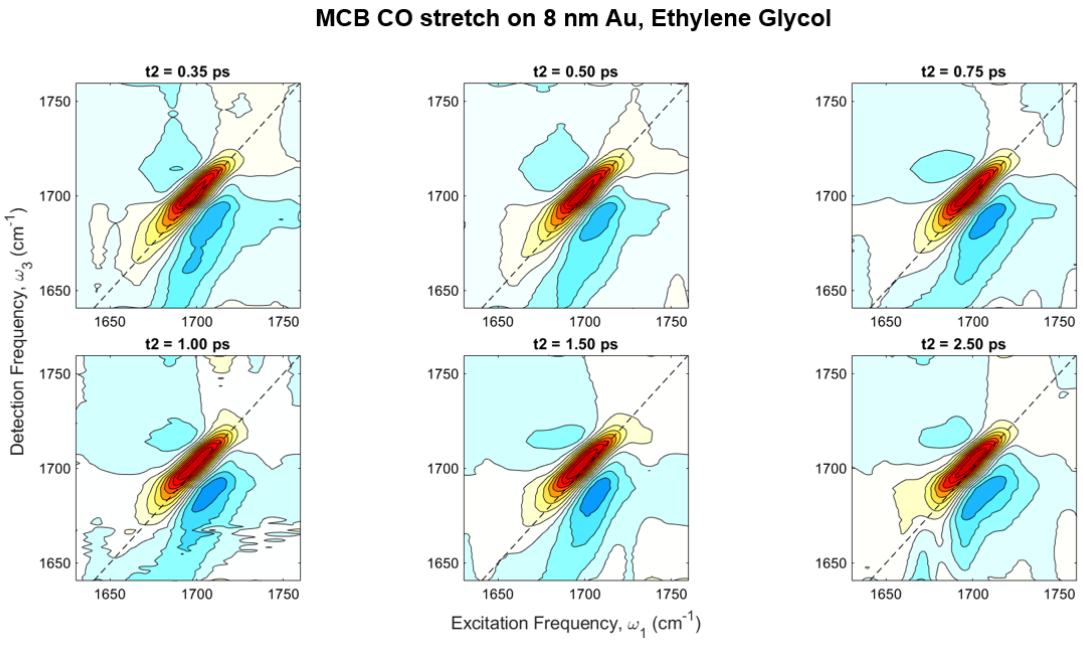

Figure C.10: 2D IR spectra as a function of waiting time t_2 for MCB on 8 nm thick sputtered Au film on a CaF_2 window taken in transmission mode. Ethylene glycol was used as the solvent and no spacer was used between the CaF_2 windows. The spectra are individually normalized.

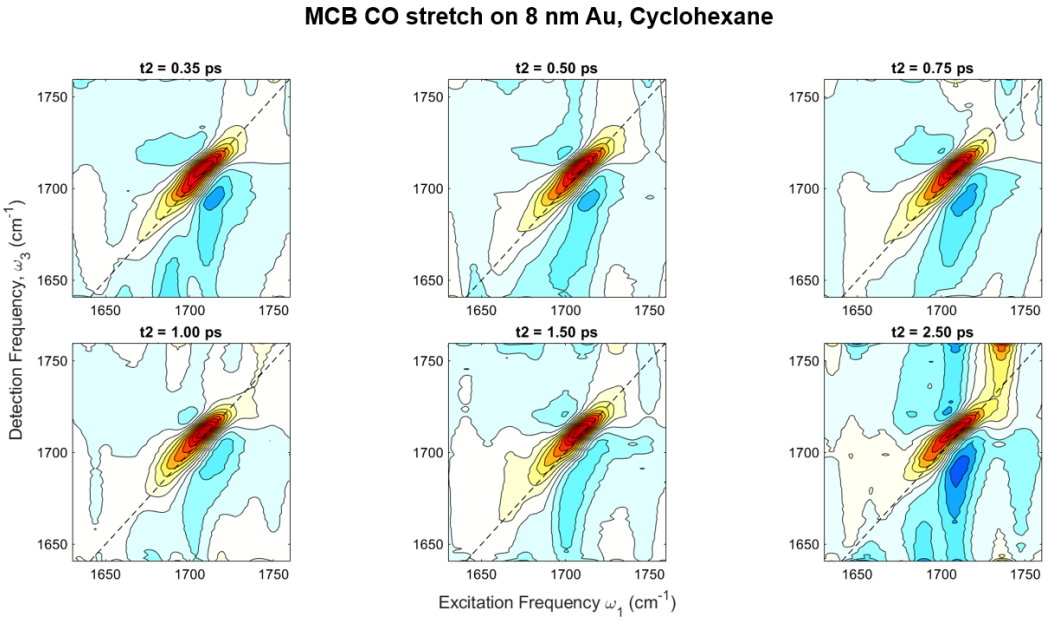

Figure C.11: 2D IR spectra as a function of waiting time t_2 for MCB on 8 nm thick sputtered Au film on a CaF_2 window taken in transmission mode. Cyclohexane was used as the solvent and no spacer was used between the CaF_2 windows. The spectra are individually normalized.

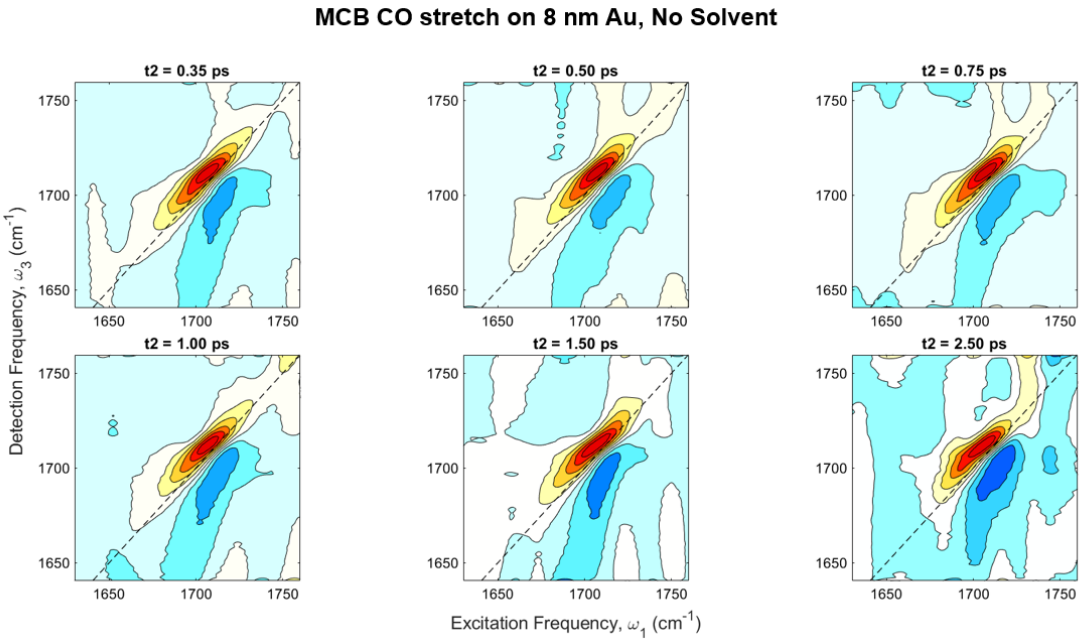

Figure C.12: 2D IR spectra as a function of waiting time t_2 for MCB on 8 nm thick sputtered Au film on a CaF_2 window taken in transmission mode. No solvent was used, the monolayer was exposed to air. The spectra are individually normalized.

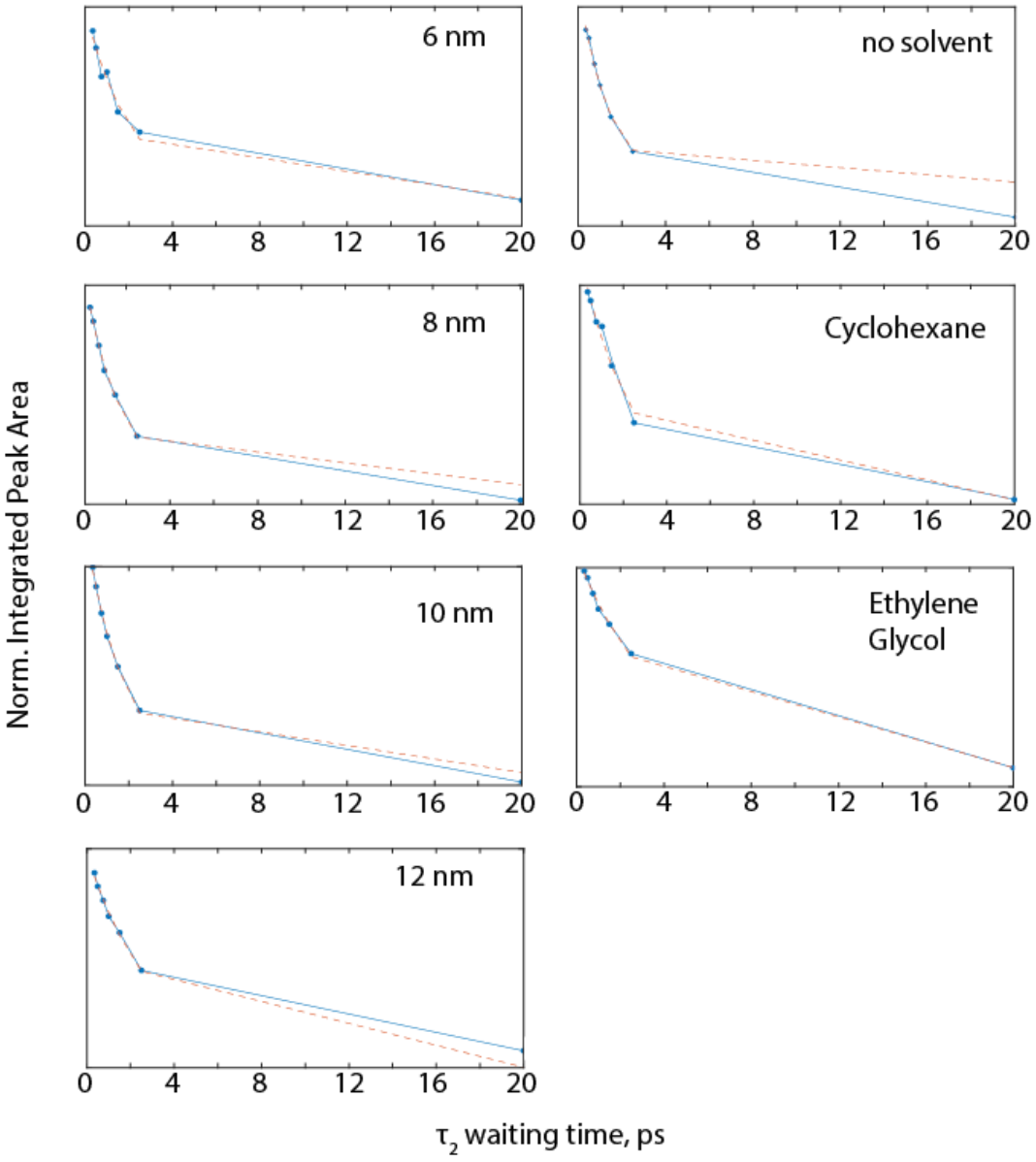

Figure C.13: Lifetime decay shown for averaged MCB CO stretch spectra for different Au film thickness (marked as 6 nm, 8 nm, 10 nm, and 12 nm) as well as different solvents with 8 nm of sputtered Au (no solvent, cyclohexane, and ethylene glycol). The integrated peak area was taken as a square ± 2 cm^{-1} from the peak maximum on the ω_3 and ω_1 axes. The resulting lifetimes and standard deviation from six averages are discussed in Chapter 6.

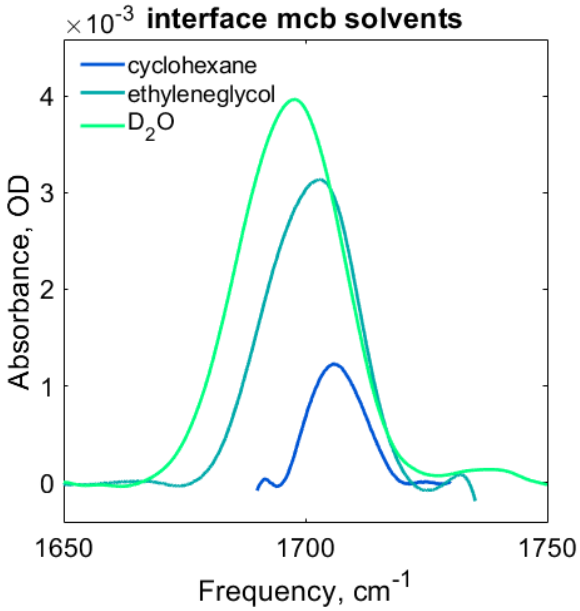

Figure C.14: FTIR taken of MCB monolayers on 8 nm Au films sputtered onto a CaF_2 window and measured in transmission mode with different solvents as displayed in the legend.

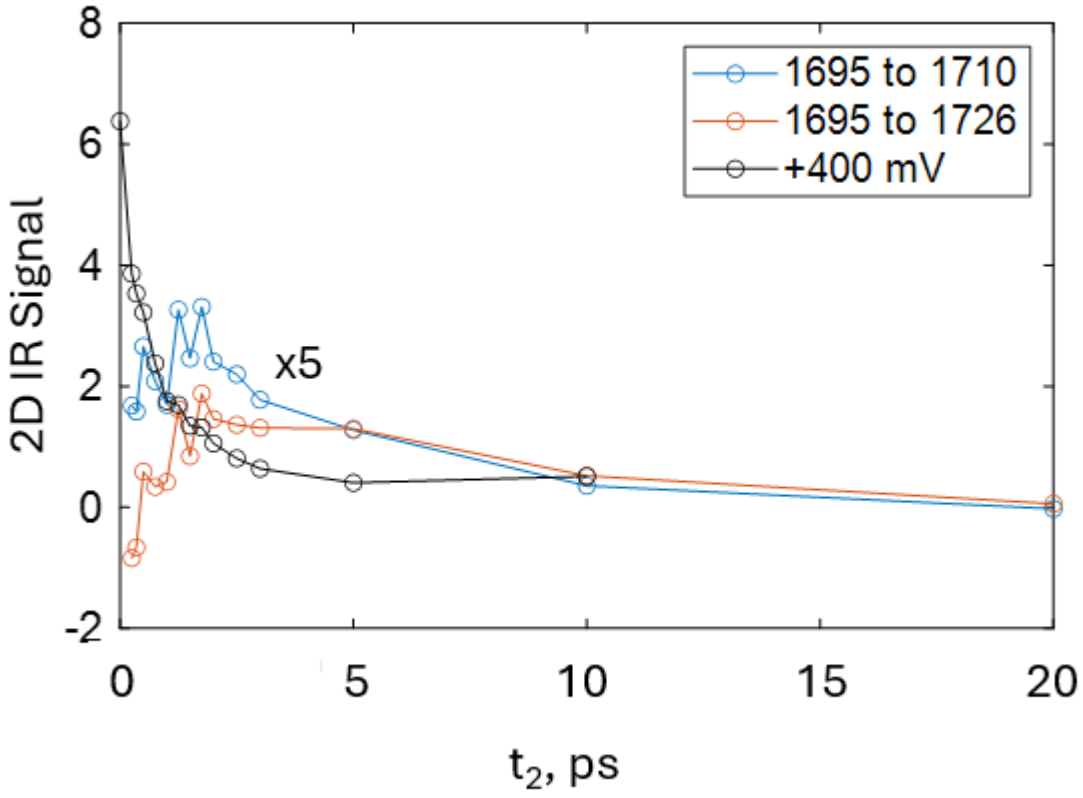

Figure C.15: Lifetime decay shown for averaged 4MMP CO stretch spectra at +400 mV and crosspeak growth from 1695 cm^{-1} to 1710 cm^{-1} and 1726 cm^{-1}. The integrated peak area was taken as a square ± 2 cm^{-1} from the peak maximum on the ω_3 and ω_1 axes.

Bibliography

(1) Błasiak, B.; Londergan, C. H.; Webb, L. J.; Cho, M. Vibrational Probes: From Small Molecule Solvatochromism Theory and Experiments to Applications in Complex Systems. Acc. Chem. Res. **2017**, *50*, 968–976, DOI: 10.1021/acs.accounts.7b00002.

(2) Choi, J.-H.; Oh, K.-I.; Lee, H.; Lee, C.; Cho, M. Nitrile and Thiocyanate IR probes: Quantum Chemistry Calculation Studies and Multivariate Least-square Fitting Analysis. J. Chem. Phys. **2008**, *128*, 134506.

(3) Lewis, N. H. C.; Iscen, A.; Felts, A.; Dereka, B.; Schatz, G. C.; Tokmakoff, A. Vibrational Probe of Aqueous Electrolytes: The Field Is Not Enough. J. Phys. Chem. B **2020**, *124*, 7013–7026.

(4) Fried, S. D. E.; Zheng, C.; Mao, Y.; Markland, T. E.; Boxer, S. G. Solvent Organization and Electrostatics Tuned by Solute Electronic Structure: Amide versus Non-Amide Carbonyls. The Journal of Physical Chemistry B **2022**, *126*, 5876–5886, DOI: 10.1021/acs.jpcb.2c03095.

(5) Bagchi, S.; Fried, S. D.; Boxer, S. G. A Solvatochromic Model Calibrates Nitriles' Vibrational Frequencies to Electrostatic Fields. J. Am. Chem. Soc. **2012**, *134*, 10373–10376, DOI: 10.1021/ja303895k.

(6) Błasiak, B.; Cho, M. Vibrational Solvatochromism. II. A First-Principle Theory of Solvation-Induced Vibrational Frequency Shift Based on Effective Fragment Potential Method. The Journal of Chemical Physics **2014**, *140*, 164107, DOI: 10.1063/1.4872040.

(7) Choi, J. H.; Cho, M. Vibrational Solvatochromism and Electrochromism of Infrared Probe Molecules containing C≡O, C≡N, C=O, or C-F Vibrational Chromophore. J. Chem. Phys. **2011**, *134*, 154513.

(8) Fafarman, A. T.; Sigala, P. A.; Herschlag, D.; Boxer, S. G. Decomposition of Vibrational Shifts of Nitriles into Electrostatic and Hydrogen-Bonding Effects. J. Am. Chem. Soc. **2010**, *132*, 12811–12813, DOI: 10.1021/ja104573b.

(9) Kocheril, P. A.; Wang, H.; Lee, D.; Naji, N.; Wei, L. Nitrile Vibrational Lifetimes as Probes of Local Electric Fields. J. Phys. Chem. Lett. **2024**, *15*, 5306–5314, DOI: 10.1021/acs.jpclett.4c00597.

(10) Kossowska, D.; Park, K.; Park, J. Y.; Lim, C.; Kwak, K.; Cho, M. Rational Design of an Acetylenic Infrared Probe with Enhanced Dipole Strength and Increased Vibrational Lifetime. J. Phys. Chem. B **2019**, 8.

(11) Nyquist, R. A.; Kirchner, T. M.; Fouchea, H. A. Vibrational Frequency Shifts of the Carbonyl Stretching Mode Induced by Solvents: Acetone. Appl. Spectrosc., AS **1989**, *43*, 1053–1055.

(12) Fried, S. D.; Wang, L.-P.; Boxer, S. G.; Ren, P.; Pande, V. S. Calculations of the Electric Fields in Liquid Solutions. J. Phys. Chem. B **2013**, 13.

(13) Fried, S. D.; Boxer, S. G. Measuring Electric Fields and Noncovalent Interactions Using the Vibrational Stark Effect. Accounts of Chemical Research **2015**, *48*, 998–1006, DOI: 10.1021/ar500464j.

(14) Mulder, W. H.; Párkányi, C. Theory of the Salt Effect on Solvatochromic Shifts And Its Potential Application to the Determination of Ground-State and Excited-State Dipole Moments. The Journal of Physical Chemistry A **2002**, *106*, Publisher: American Chemical Society, 11932–11937, DOI: 10.1021/jp026505o.

(15) Berkowitz, M. L. Molecular Simulations of Aqueous Electrolytes: Role of Explicit Inclusion of Charge Transfer into Force Fields. J. Phys. Chem. B **2021**, DOI: 10.1021/acs.jpcb.1c08383.

(16) Bian, H.; Wen, X.; Li, J.; Chen, H.; Han, S.; Sun, X.; Song, J.; Zhuang, W.; Zheng, J. Ion Clustering in Aqueous Solutions Probed with Vibrational Energy Transfer. PNAS **2011**, *108*, 4737–4742, DOI: 10.1073/pnas.1019565108.

(17) Chen, H.; Ruckenstein, E. Hydrated Ions: From Individual Ions to Ion Pairs to Ion Clusters. J. Phys. Chem. B **2015**, *119*, 12671–12676, DOI: 10.1021/acs.jpcb.5b06837.

(18) Wu, J. Understanding the Electric Double-Layer Structure, Capacitance, and Charging Dynamics. Chem. Rev. **2022**, *122*, 10821–10859.

(19) Shin, S.-J.; Kim, D. H.; Bae, G.; Ringe, S.; Choi, H.; Lim, H.-K.; Choi, C. H.; Kim, H. On the Importance of the Electric Double Layer Structure in Aqueous Electrocatalysis. Nat. Commun. **2022**, *13*, 174.

(20) Fleischmann, S.; Mitchell, J. B.; Wang, R.; Zhan, C.; Jiang, D.-e.; Presser, V.; Augustyn, V. Pseudocapacitance: From Fundamental Understanding to High Power Energy Storage Materials. Chem. Rev. **2020**, *120*, 6738–6782, DOI: 10.1021/acs.chemrev.0c00170.

(21) Doblhoff-Dier, K.; Koper, M. T. M. Modeling the Gouy–Chapman Diffuse Capacitance with Attractive Ion–Surface Interaction. J. Phys. Chem. C **2021**, *125*, 16664–16673, DOI: 10.1021/acs.jpcc.1c02381.

(22) Kant, R.; Singh, M. B. Generalization of the Gouy-Chapman-Stern Model of an Electric Double Layer for a Morphologically Complex Electrode: Deterministic and Stochastic Morphologies. Phys. Rev. E **2013**, *88*, 052303, DOI: 10.1103/PhysRevE.88.052303.

(23) Kinraide, T. B. Use of a Gouy-Chapman-Stern Model for Membrane-Surface Electrical Potential to Interpret Some Features of Mineral Rhizotoxicity. Plant Physiol **1994**, *106*, 1583–1592, DOI: 10.1104/pp.106.4.1583.

(24) Rytwo, G. Applying a Gouy–Chapman–Stern Model for Adsorption of Organic Cations to Soils. Applied Clay Science **2004**, *24*, 137–147, DOI: 10.1016/j.clay.2003.01.001.

(25) Tournassat, C.; Bourg, I. C.; Steefel, C. I. In Clays in Natural and Engineered Barriers for Radioactive Waste Confinement, 2015.

(26) Torrie, G. M.; Valleau, J. P. Electrical Double Layers. 4. Limitations of the Gouy-Chapman Theory. J. Phys. Chem. **1982**, *86*, 3251–3257, DOI: 10.1021/j100213a035.

(27) Shapovalov, V. L.; Brezesinski, G. Breakdown of the Gouy-Chapman Model for Highly Charged Langmuir Monolayers: Counterion Size Effect. J. Phys. Chem. B **2006**, *110*, 10032–10040, DOI: 10.1021/jp056801b.

(28) Li, P.; Jiang, Y.; Hu, Y.; Men, Y.; Liu, Y.; Cai, W.; Chen, S. Hydrogen Bond Network Connectivity in the Electric Double Layer Dominates the Kinetic pH

Effect in Hydrogen Electrocatalysis on Pt. Nat Catal **2022**, *5*, 900–911, DOI: 10.1038/s41929-022-00846-8.

(29) Parshotam, S.; Rehl, B.; Busse, F.; Brown, A.; Gibbs, J. M. Influence of the Hydrogen-Bonding Environment on Vibrational Coupling in the Electrical Double Layer at the Silica/Aqueous Interface. J. Phys. Chem. C **2022**, *126*, 21734–21744, DOI: 10.1021/acs.jpcc.2c06412.

(30) Kazi, O. A.; Chen, W.; Eatman, J. G.; Gao, F.; Liu, Y.; Wang, Y.; Xia, Z.; Darling, S. B. Material Design Strategies for Recovery of Critical Resources from Water. Adv. Mater. **2023**, *23*, 2300913.

(31) Barry, E. et al. Advanced Materials for Energy-Water Systems: The Central Role of Water/Solid Interfaces in Adsorption, Reactivity, and Transport. Chem. Rev. **2021**, *121*, 9450–9501.

(32) Wain, A. J.; O'Connell, M. A. Advances in Surface-Enhanced Vibrational Spectroscopy at Electrochemical Interfaces. Adv. Phys. X **2017**, *2*, 188–209.

(33) Ashley, K.; Pons, S. Infrared Spectroelectrochemistry. Chem. Rev. **1988**, *88*, 673–695.

(34) Wang, H.-L.; You, E.-M.; Panneerselvam, R.; Ding, S.-Y.; Tian, Z.-Q. Advances of Surface-Enhanced Raman and IR Spectroscopies: From Nano/Microstructures to Macro-optical Design. Light: Sci. Appl. **2021**, *10*, 161.

(35) Fockaert, L.; Würger, T.; Unbehau, R.; Boelen, B.; Meißner, R.; Lamaka, S.; Zheludkevich, M.; Terryn, H.; Mol, J. ATR-FTIR in Kretschmann Configuration Integrated with Electrochemical Cell as In Situ Interfacial Sensitive Tool to Study Corrosion Inhibitors for Magnesium Substrates. Electrochim. Acta **2020**, *345*, 136166.

(36) Le, F.; Brandl, D. W.; Urzhumov, Y. A.; Wang, H.; Kundu, J.; Halas, N. J.; Aizpurua, J.; Nordlander, P. Metallic Nanoparticle Arrays: A Common Substrate for Both Surface-Enhanced Raman Scattering and Surface-Enhanced Infrared Absorption. ACS Nano **2008**, *2*, 707–718.

(37) Schlücker, S. Surface-Enhanced Raman Spectroscopy: Concepts and Chemical Applications. Angew. Chem., Int. Ed. **2014**, *53*, 4756–4795.

(38) Langer, J. et al. Present and Future of Surface-Enhanced Raman Scattering. ACS Nano **2020**, *14*, 28–117.

(39) Ding, S.-Y.; Yi, J.; Li, J.-F.; Ren, B.; Wu, D.-Y.; Panneerselvam, R.; Tian, Z.-Q. Nanostructure-based Plasmon-Enhanced Raman Spectroscopy for Surface Analysis of Materials. Nat. Rev. Mater. **2016**, *1*, 1–16.

(40) Chowdhury, A. U.; Muralidharan, N.; Daniel, C.; Amin, R.; Belharouak, I. Probing the Electrolyte/Electrode Interface with Vibrational Sum Frequency Generation Spectroscopy: A Review. J. Power Sources **2021**, *506*, 230173.

(41) Sorenson, S. A.; Patrow, J. G.; Dawlaty, J. M. Solvation Reaction Field at the Interface Measured by Vibrational Sum Frequency Generation Spectroscopy. J. Am. Chem. Soc. **2017**, *139*, 2369–2378.

(42) Jiang, X.; Zaitseva, E.; Schmidt, M.; Siebert, F.; Engelhard, M.; Schlesinger, R.; Ataka, K.; Vogel, R.; Heberle, J. Resolving Voltage-Dependent Structural Changes of a Membrane Photoreceptor by Surface-Enhanced IR Difference Spectroscopy. Proc. Natl. Acad. Sci. U. S. A. **2008**, *105*, 12113–12117.

(43) Melin, F.; Hellwig, P. Recent Advances in the Electrochemistry and Spectroelectrochemistry of Membrane Proteins. Biol. Chem. **2013**, *394*, 593–609.

(44) Kottke, T.; Lórenz-Fonfría, V. A.; Heberle, J. The Grateful Infrared: Sequential Protein Structural Changes Resolved by Infrared Difference Spectroscopy. J. Phys. Chem. B **2016**, *121*, 335—350.

(45) López-Lorente, I.; Kranz, C. Recent Advances in Biomolecular Vibrational Spectroelectrochemistry. Curr. Opin. Electrochem. **2017**, *5*, 106–113.

(46) Machan, C. W. Recent Advances in Spectroelectrochemistry Related to Molecular Catalytic Processes. Curr. Opin. Electrochem. **2019**, *15*, 42–49.

(47) Ly, K. H.; Weidinger, I. M. Understanding Active Sites in Molecular (Photo)Electrocatalysis through Complementary Vibrational Spectroelectrochemistry. Chem. Comm. **2021**, *57*, 2328–2342.

(48) Ataka, K.-i.; Yotsuyanagi, T.; Osawa, M. Potential-Dependent Reorientation of Water Molecules at an Electrode/Electrolyte Interface Studied by Surface-Enhanced Infrared Absorption Spectroscopy. Am. J. Phys. Chem. **1996**, *100*, 10664–10672.

(49) Ostrander, J. S.; Lomont, J. P.; Rich, K. L.; Saraswat, V.; Feingold, B. R.; Petti, M. K.; Birdsall, E. R.; Arnold, M. S.; Zanni, M. T. Monolayer Sensitivity Enables a 2D IR Spectroscopic Immuno-biosensor for Studying Protein Structures: Application to Amyloid Polymorphs. The Journal of Physical Chemistry Letters **2019**, *10*, 3836–3842.

(50) Kraack, J. P.; Hamm, P. Surface-Sensitive and Surface-Specific Ultrafast Two-Dimensional Vibrational Spectroscopy. Chem. Rev. **2017**, *117*, 10623–10664.

(51) Chuntonov, L.; Rubtsov, I. V. Surface-Enhanced Ultrafast Two-Dimensional Vibrational Spectroscopy with Engineered Plasmonic Nano-antennas. J. Chem. Phys. **2020**, *153*, 050902.

(52) Gomes, R. J.; Birch, C.; Cencer, M. M.; Li, C.; Son, S.-B.; Bloom, I. D.; Assary, R. S.; Amanchukwu, C. V. Probing Electrolyte Influence on CO_2 Reduction in Aprotic Solvents. J. Phys. Chem. C **2022**, *126*, 13595–13606.

(53) Hartstein, A.; Kirtley, J. R.; Tsang, J. C. Enhancement of the Infrared Absorption from Molecular Monolayers with Thin Metal Overlayers. Phys. Rev. Lett. **1980**, *45*, 201–204, DOI: 10.1103/PhysRevLett.45.201.

(54) Advances of SERS and SEIRA: from nano/micro-structures to macro-optical design, en, 2024.

(55) Hamm, P.; Lim, M.; Hochstrasser, R. M. Non-Markovian Dynamics of the Vibrations of Ions in Water from Femtosecond Infrared Three-Pulse Photon Echoes. Phys. Rev. Lett. **1998**, *81*, 5326–5329, DOI: 10.1103/PhysRevLett.81.5326.

(56) El Khoury, Y.; Van Wilderen, L. J. G. W.; Vogt, T.; Winter, E.; Bredenbeck, J. A spectroelectrochemical cell for ultrafast two-dimensional infrared spectroscopy. Review of Scientific Instruments **2015**, *86*, Publisher: American Institute of Physics, 083102, DOI: 10.1063/1.4927533.

(57) Lotti, D.; Hamm, P.; Kraack, J. P. Surface-Sensitive Spectro-electrochemistry Using Ultrafast 2D ATR IR Spectroscopy. The Journal of Physical Chemistry C **2016**, *120*, Publisher: American Chemical Society, 2883–2892, DOI: 10.1021/acs.jpcc.6b00395.

(58) Yang, N.; Ryan, M. J.; Son, M.; Mavrič, A.; Zanni, M. T. Voltage-Dependent FTIR and 2D Infrared Spectroscopies within the Electric Double Layer Using a Plasmonic and Conductive Electrode. The Journal of Physical Chemistry B **2023**, *127*,

Publisher: American Chemical Society, 2083–2091, DOI: 10.1021/acs.jpcb.2c08431.

(59) Thomas, M. E.; Tropf, W. J. OPTICAL PROPERTIES OF DIAMOND.

(60) Optical Lenses, Crystran Knowledge Centre, https://www.crystran.com/knowledge-centre.

(61) Lewis, N. H. C.; Tokmakoff, A. Lineshape Distortions in Internal Reflection Two-Dimensional Infrared Spectroscopy: Tuning across the Critical Angle. The Journal of Physical Chemistry Letters **2021**, *12*, 11843–11849, DOI: 10.1021/acs.jpclett.1c03432.

(62) Bloem, R.; Garrett-Roe, S.; Strzalka, H.; Hamm, P.; Donaldson, P. Enhancing signal detection and completely eliminating scattering using quasi-phase-cycling in 2D IR experiments. Optics Express **2010**, *18*, 27067, DOI: 10.1364/OE.18.027067.

(63) Ataka, K.; Stripp, S. T.; Heberle, J. Surface-Enhanced Infrared Absorption Spectroscopy (SEIRAS) to Probe Monolayers of Membrane Proteins. Biochimica et Biophysica Acta (BBA) - Biomembranes **2013**, *1828*, 2283–2293, DOI: 10.1016/j.bbamem.2013.04.026.

(64) Yang, N.; Ryan, M. J.; Son, M.; Mavrič, A.; Zanni, M. T. Voltage-Dependent FTIR and 2D Infrared Spectroscopies within the Electric Double Layer using a Plasmonic and Conductive Electrode. J. Phys. Chem. B **2023**, *127*, 2083–2091.

(65) Uchida, T.; Osawa, M.; Lipkowski, J. SEIRAS Studies of Water Structure at the Gold Electrode Surface in the Presence of Supported Lipid Bilayer. Journal of Electroanalytical Chemistry **2014**, *716*, 112–119, DOI: 10.1016/j.jelechem.2013.10.015.

(66) Błasiak, B.; Ritchie, A. W.; Webb, L. J.; Cho, M. Vibrational Solvatochromism of Nitrile Infrared Probes: Beyond the Vibrational Stark Dipole Approach. Phys. Chem. Chem. Phys. **2016**, *18*, 18094–18111.

(67) Dereka, B.; Lewis, N. H. C.; Keim, J. H.; Snyder, S. A.; Tokmakoff, A. Characterization of Acetonitrile Isotopologues as Vibrational Probes of Electrolytes. J. Phys. Chem. B **2022**, *126*, 278–291, DOI: 10.1021/acs.jpcb.1c09572.

(68) Drexler, C. I.; Cracchiolo, O. M.; Myers, R. L.; Okur, H. I.; Serrano, A. L.; Corcelli, S. A.; Cremer, P. S. Local Electric Fields in Aqueous Electrolytes. J. Phys. Chem. B **2021**, *125*, 8484–8493, DOI: 10.1021/acs.jpcb.1c03257.

(69) Biswal, H. S.; Shirhatti, P. R.; Wategaonkar, S. O-H···O versus O-H···S Hydrogen Bonding. 2. Alcohols and Thiols as Hydrogen Bond Acceptors. J. Phys. Chem. A **2010**, *114*, 6944–6955, DOI: 10.1021/jp102346n.

(70) Mollerup, J. M.; Breil, M. P. Modeling the permittivity of electrolyte solutions. AIChE Journal **2015**, *61*, _eprint: https://onlinelibrary.wiley.com/doi/pdf/10.1002/aic.14799, 2854–2860, DOI: 10.1002/aic.14799.

(71) Li, M.; Zhuang, B.; Lu, Y.; Wang, Z.-G.; An, L. Accurate Determination of Ion Polarizabilities in Aqueous Solutions. The Journal of Physical Chemistry B **2017**, *121*, Publisher: American Chemical Society, 6416–6424, DOI: 10.1021/acs.jpcb.7b04111.

(72) Marcus, Y. Thermodynamics of Solvation of Ions. Part 5.—Gibbs Free Energy of Hydration at 298.15 K. Journal of the Chemical Society, Faraday Transactions **1991**, *87*, 2995–2999, DOI: 10.1039/FT9918702995.

(73) Kneipp, K.; Kneipp, H.; Kneipp, J., *Plasmonics for Enhanced Vibrational Signatures*; Shahbazyan, T. V., Stockman, M. I., Eds.; Springer Netherlands: Dordrecht, 2013, pp 103–124, DOI: 10.1007/978-94-007-7805-4_2.

(74) Enoch, S.; Bonod, N., *Plasmonics: From Basics to Advanced Topics*; Springer: 2012.

(75) Okamoto, K., Tuning of the Surface Plasmon Resonance in the UV-IR Range for Wider Applications In Frontiers of Plasmon Enhanced Spectroscopy Volume 2; ACS Symposium Series 1246, Vol. 1246, Section: 11; American Chemical Society: 2016, pp 247–259, DOI: 10.1021/bk-2016-1246.ch011.

(76) Sarid, D.; Challener, W. A., *Modern introduction to surface plasmons: theory, Mathematica modeling, and applications*; Cambridge university press: 2010.

(77) Sullivan, D. M.; IEEE Microwave Theory and Techniques Society., *Electromagnetic simulation using the FDTD method*; IEEE Press series on RF and microwave technology, OCLC: 557447655; IEEE Press: New York, 2000.

(78) Chaumet, P. C. The Discrete Dipole Approximation: A Review. Mathematics **2022**, *10*, 3049, DOI: 10.3390/math10173049.

(79) Hohenester, U.; Trügler, A. MNPBEM – A Matlab toolbox for the simulation of plasmonic nanoparticles. Computer Physics Communications **2012**, *183*, 370–381, DOI: 10.1016/j.cpc.2011.09.009.

(80) Hooshmand, N., Plasmonic Properties of Two Silver Nanocubes: Dependence on Separation Distance, Relative Orientation, Refractive Index of the Substrate, and Exciting Light Propagation Direction In
Frontiers of Plasmon Enhanced Spectroscopy Volume 2; ACS Symposium Series 1246, Vol. 1246, Section: 2; American Chemical Society: 2016, pp 21–40, DOI: 10.1021/bk-2016-1246.ch002.

(81) Johnson, R. W.; Hultqvist, A.; Bent, S. F. A Brief Review of Atomic Layer Deposition: From Fundamentals to Applications. Mater. Today **2014**, *17*, 236–246.

(82) Vogt, J.; Huck, C.; Neubrech, F.; Pucci, A., Plasmonic Light Scattering and Infrared Vibrational Signal Enhancement In
Frontiers of Plasmon Enhanced Spectroscopy Volume 2; ACS Symposium Series 1246, Vol. 1246, Section: 1; American Chemical Society: 2016, pp 1–19, DOI: 10.1021/bk-2016-1246.ch001.

(83) Demirdöven, N; Khalil, M; Golonzka, O; Tokmakoff, A Dispersion Compensation with Optical Materials for Compression of Intense Sub-100-fs Mid-Infrared Pulses. Opt. Lett. **2002**, *27*, 433.

(84) Adato, R.; Yanik, A. A.; Amsden, J. J.; Kaplan, D. L.; Omenetto, F. G.; Hong, M. K.; Erramilli, S.; Altug, H. Ultra-Sensitive Vibrational Spectroscopy of Protein Monolayers with Plasmonic Nanoantenna Arrays.
Proc. Natl. Acad. Sci. U. S. A. **2009**, *106*, 19227–19232.

(85) Adato, R.; Aksu, S.; Altug, H. Engineering Mid-Infrared Nanoantennas for Surface Enhanced Infrared Absorption Spectroscopy. Mater. Today **2015**, *18*, 436–446.

(86) Pfitzner, E.; Seki, H.; Schlesinger, R.; Ataka, K.; Heberle, J. Disc Antenna Enhanced Infrared Spectroscopy: From Self-Assembled Monolayers to Membrane Proteins. ACS Sens. **2018**, *3*, 984–991.

(87) Gandman, A.; Mackin, R.; Cohn, B.; Rubtsov, I. V.; Chuntonov, L. Two-Dimensional Fano Lineshapes in Ultrafast Vibrational Spectroscopy of Thin Molecular Layers on Plasmonic Arrays. J. Phys. Chem. Lett. **2017**, *8*, 3341–3346.

(88) Sun, X.; Li, H. Gold Nanoisland Arrays by Repeated Deposition and Post-Deposition Annealing for Surface-Enhanced Raman Spectroscopy. Nanotechnology **2013**, *24*, 355706.

(89) Arun Kumar, D.; Merline Shyla, J.; Xavier, F. P. Synthesis and Characterization of TiO_2/SiO_2 Nano Composites for Solar Cell Applications. Appl. Nanosci. **2012**, *2*, 429–436.

(90) Chen, L.; He, X.; Liu, H.; Qian, L.; Kim, S. H. Water Adsorption on Hydrophilic and Hydrophobic Surfaces of Silicon. The Journal of Physical Chemistry C **2018**, *122*, 11385–11391.

(91) Pucci, A.; Neubrech, F.; Weber, D.; Hong, S.; Toury, T.; de la Chapelle, M. L. Surface Enhanced Infrared Spectroscopy using Gold Nanoantennas. Phys. Status Solidi **2010**, *247*, 2071–2074.

(92) Enders, D.; Nagao, T.; Pucci, A.; Nakayama, T.; Aono, M. Surface-Enhanced ATR-IR Spectroscopy with Interface-Grown Plasmonic Gold-Island Films near the Percolation Threshold. Phys. Chem. Chem. Phys. **2011**, *13*, 4935–4941.

(93) Schofield, A. J.; Blümel, R.; Kohler, A.; Lukacs, R.; Hirschmugl, C. J. Extracting Pure Absorbance Spectra in Infrared Microspectroscopy by Modeling Absorption Bands as Fano Resonances. J. Chem. Phys. **2019**, *150*, 154124.

(94) Yi, J.; You, E.-M.; Ding, S.-Y.; Tian, Z.-Q. Unveiling the Molecule–Plasmon Interactions in Surface-Enhanced Infrared Absorption Spectroscopy. Natl. Sci. Rev. **2020**, *7*, 1228–1238.

(95) O'Callahan, B. T.; Hentschel, M.; Raschke, M. B.; El-Khoury, P. Z.; Lea, A. S. Ultrasensitive Tip- and Antenna-Enhanced Infrared Nanoscopy of Protein Complexes. The Journal of Physical Chemistry C **2019**, *123*, 17505–17509.

(96) Gupta, R.; Dyer, M. J.; Weimer, W. A. Preparation and Characterization of Surface Plasmon Resonance Tunable Gold and Silver Films. J. Appl. Phys. **2002**, *92*, 5264–5271.

(97) Bodine, M.; Rozyyev, V.; Elam, J.; Tokmakoff, A.; Lewis, N. H. C. Vibrational Probe at the Electrochemical Interface: Dependence on Plasmon Coupling and Potential on the Lineshape in Two-Dimensional Infrared Spectroscopy. In Preparation **2023**.

(98) Valentine, M. L.; Al-Mualem, Z. A.; Baiz, C. R. Pump Slice Amplitudes: A Simple and Robust Method for Connecting Two-Dimensional Infrared and Fourier Transform Infrared Spectra. J. Phys. Chem. A **2021**, *125*, 6498–6504.

(99) Lewis, N. H. C.; Tokmakoff, A. Lineshape Distortions in Internal Reflection Two-Dimensional Infrared Spectroscopy: Tuning across the Critical Angle. J. Phys. Chem. Lett. **2021**, *12*, 11843–11849.

(100) Khurana, K.; Jaggi, N. Localized Surface Plasmonic Properties of Au and Ag Nanoparticles for Sensors: A Review. Plasmonics **2021**, *16*, 981–999.

(101) Sarkar, S.; Maitra, A.; Banerjee, S.; Thoi, V. S.; Dawlaty, J. M. Electric Fields at Metal–Surfactant Interfaces: A Combined Vibrational Spectroscopy and Capacitance Study. J. Phys. Chem. B **2020**, *124*, 1311–1321.

(102) Lotti, D.; Hamm, P.; Kraack, J. P. Surface-Sensitive Spectro-electrochemistry Using Ultrafast 2D ATR IR Spectroscopy. J. Phys. Chem. C **2016**, *120*, 2883–2892.

(103) Bhattacharyya, D.; Videla, P. E.; Palasz, J. M.; Tangen, I.; Meng, J.; Kubiak, C. P.; Batista, V. S.; Lian, T. Sub-Nanometer Mapping of the Interfacial Electric Field Profile Using a Vibrational Stark Shift Ruler. J. Am. Chem. Soc. **2022**, *144*, 14330–14338.

(104) Reppert, M.; Tokmakoff, A. Electrostatic Frequency Shifts in Amide I Vibrational Spectra: Direct Parameterization Against Experiment. J. Chem. Phys. **2013**, *138*, 134116.

(105) Yamada, S. A.; Thompson, W. H.; Fayer, M. D. Water-Anion Hydrogen Bonding Dynamics: Ultrafast IR Experiments and Simulations. J. Chem. Phys. **2017**, *146*, 234501.

(106) Elam, J. W.; Groner, M. D.; George, S. M. Viscous Flow Reactor with Quartz Crystal Microbalance for Thin Film Growth by Atomic Layer Deposition. Rev. Sci. Instrum. **2002**, *73*, 2981–2987.

(107) Elam, J. W.; Baker, D. A.; Hryn, A. J.; Martinson, A. B. F.; Pellin, M. J.; Hupp, J. T. Atomic Layer Deposition of Tin Oxide Films using Tetrakis(dimethylamino) Tin. Journal of Vacuum Science & Technology A **2008**, *26*, 244–252.

(108) Elam, J. W.; Baker, D. A.; Martinson, A. B. F.; Pellin, M. J.; Hupp, J. T. Atomic Layer Deposition of Indium Tin Oxide Thin Films Using Nonhalogenated Precursors. The Journal of Physical Chemistry C **2008**, *112*, Publisher: American Chemical Society, 1938–1945.

(109) Nečas, D.; Klapetek, P. Gwyddion: an Open-source Software for SPM Data Analysis. Open Phys. **2012**, *10*, 181–188.

(110) Andvaag, I. R.; Morhart, T. A.; Clarke, O. J. R.; Burgess, I. J. Hybrid Gold–Conductive Metal Oxide Films for Attenuated Total Reflectance Surface Enhanced Infrared Absorption Spectroscopy. ACS Appl. Nano Mater. **2019**, *2*, 1274–1284.

(111) Andvaag, I. R.; Lins, E.; Burgess, I. J. An Effective Medium Theory Description of Surface-Enhanced Infrared Absorption from Metal Island Layers Grown on Conductive Metal Oxide Films. J. Phys. Chem. C **2021**, *125*, 22301–22311.

(112) Phan, V. T. T.; Andvaag, I. R.; Boyle, N. D.; Flaman, G. T.; Unni, B.; Burgess, I. J. Surface Sensitive Infrared Spectroelectrochemistry using Palladium Electrodeposited on ITO-Modified Internal Reflection Elements. Phys. Chem. Chem. Phys. **2022**, *24*, 2925–2933.

(113) Mohammad Miraz, A. S.; Sun, S.; Shao, S.; Meng, W. J.; Ramachandran, B. R.; Wick, C. D. Computational Study of Metal/Ceramic Interfacial Adhesion and Barriers to Shear Displacement. Comput. Mater. Sci. **2019**, *168*, 104–115.

(114) Alemany, P.; Boorse, R. S.; Burlitch, J. M.; Hoffmann, R. Metal-Ceramic Adhesion: Quantum Mechanical Modeling of Transition Metal-Alumina Interfaces. Am. J. Phys. Chem. **1993**, *97*, 8464–8475.

(115) Lica, G. C.; Tong, Y. J. Electrochemical Impedance Spectroscopic Measurement of Potential of Zero Charge of Octanethiolate-protected Au and Pd Nanoparticles. J. Electroanal. Chem. **2013**, *688*, 349–353.

(116) Shatla, A. S.; Landstorfer, M.; Baltruschat, H. On the Differential Capacitance and Potential of Zero Charge of Au(111) in Some Aprotic Solvents. ChemElectroChem **2021**, *8*, 1817–1835.

(117) Khatib, R.; Backus, E. H. G.; Bonn, M.; Perez-Haro, M.-J.; Gaigeot, M.-P.; Sulpizi, M. Water Orientation and Hydrogen-Bond Structure at the Fluorite/Water Interface. Sci. Rep. **2016**, *6*, 24287.

(118) Goldsmith, Z. K.; Secor, M.; Hammes-Schiffer, S. Inhomogeneity of Interfacial Electric Fields at Vibrational Probes on Electrode Surfaces. ACS Central Science **2020**, *6*, 304–311.

(119) Lake, W. R.; Meng, J.; Dawlaty, J. M.; Lian, T.; Hammes-Schiffer, S. Electro-inductive Effect Dominates Vibrational Frequency Shifts of Conjugated Probes on Gold Electrodes. Journal of the American Chemical Society **2023**, *145*.

(120) Birdsall, E. R.; Petti, M. K.; Saraswat, V.; Ostrander, J. S.; Arnold, M. S.; Zanni, M. T. Structure Changes of a Membrane Polypeptide Under an Applied Voltage Observed with Surface-Enhanced 2D IR Spectroscopy. The Journal of Physical Chemistry Letters **2021**, *12*, 1786–1792.

(121) Bodine, M.; Rozyyev, V.; Elam, J. W.; Tokmakoff, A.; Lewis, N. H. C. Vibrational Probe at the Electrochemical Interface: Dependence on Plasmon Coupling and Potential of the Lineshape in Two-Dimensional Infrared Spectroscopy. J. Phys. Chem. Lett. **2023**, *14*, 11092–11099, DOI: 10.1021/acs.jpclett.3c02987.

(122) An, N.; Zhuang, B.; Li, M.; Lu, Y.; Wang, Z.-G. Combined Theoretical and Experimental Study of Refractive Indices of Water–Acetonitrile–Salt Systems. J. Phys. Chem. B **2015**, *119*, 10701–10709.

(123) El Khoury, Y.; Van Wilderen, L. J. G. W.; Vogt, T.; Winter, E.; Bredenbeck, J. A Spectroelectrochemical Cell for Ultrafast Two-Dimensional Infrared Spectroscopy. Rev. Sci. Instrum. **2015**, *86*, 083102.

(124) Lyu, Y.; Becerril, L. M.; Vanzan, M.; Corni, S.; Cattelan, M.; Granozzi, G.; Frasconi, M.; Rajak, P.; Banerjee, P.; Ciancio, R.; Mancin, F.; Scrimin, P. The Interaction of Amines with Gold Nanoparticles. Adv. Mater. **2023**, 2211624.

(125) Ledezma-Yanez, I.; Wallace, W. D. Z.; Sebastián-Pascual, P.; Climent, V.; Feliu, J. M.; Koper, M. T. M. Interfacial Water Reorganization as a pH-dependent

Descriptor of the Hydrogen Evolution Rate on Platinum Electrodes. Nat. Energy **2017**, *2*, 1–7.

(126) Auer, A.; Ding, X.; Bandarenka, A. S.; Kunze-Liebhäuser, J. The Potential of Zero Charge and the Electrochemical Interface Structure of Cu(111) in Alkaline Solutions. J. Phys. Chem. C **2021**, *125*, 5020–5028, DOI: 10.1021/acs.jpcc.0c09289.

(127) Li, J.; Qian, H.; Chen, H.; Zhao, Z.; Yuan, K.; Chen, G.; Miranda, A.; Guo, X.; Chen, Y.; Zheng, N.; Wong, M. S.; Zheng, J. Two Distinctive Energy Migration Pathways of Monolayer Molecules on Metal Nanoparticle Surfaces. Nat Commun **2016**, *7*, 10749, DOI: 10.1038/ncomms10749.

(128) Shin, S.-J.; Kim, D. H.; Bae, G.; Ringe, S.; Choi, H.; Lim, H.-K.; Choi, C. H.; Kim, H. On the Importance of the Electric Double Layer Structure in Aqueous Electrocatalysis. Nat Commun **2022**, *13*, 174, DOI: 10.1038/s41467-021-27909-x.

(129) Schmidt, J. R.; Corcelli, S. A.; Skinner, J. L. Pronounced Non-Condon Effects in the Ultrafast Infrared Spectroscopy of Water. The Journal of Chemical Physics **2005**, *123*, 044513, DOI: 10.1063/1.1961472.

(130) Ghosh, S. K.; Nath, S.; Kundu, S.; Esumi, K.; Pal, T. Solvent and Ligand Effects on the Localized Surface Plasmon Resonance (LSPR) of Gold Colloids. J. Phys. Chem. B **2004**, *108*, 13963–13971, DOI: 10.1021/jp047021q.

(131) Kuryoz, P. Yu.; Poperenko, L. V.; Kravets, V. G. Correlation between Dielectric Constants and Enhancement of Surface Plasmon Resonances for Thin Gold Films. physica status solidi (a) **2013**, *210*, 2445–2455, DOI: 10.1002/pssa.201329272.

(132) Mahmoud, M. A.; Chamanzar, M.; Adibi, A.; El-Sayed, M. A. Effect of the Dielectric Constant of the Surrounding Medium and the Substrate on the Surface Plasmon Resonance Spectrum and Sensitivity Factors of Highly Symmetric Systems: Silver Nanocubes. J. Am. Chem. Soc. **2012**, *134*, 6434–6442, DOI: 10.1021/ja300901e.

(133) Xu, G.; Tazawa, M.; Jin, P.; Nakao, S.; Yoshimura, K. Wavelength Tuning of Surface Plasmon Resonance Using Dielectric Layers on Silver Island Films. Applied Physics Letters **2003**, *82*, 3811–3813, DOI: 10.1063/1.1578518.

(134) Santos, S.; Amadei, C. A.; Lai, C.-Y.; Olukan, T.; Lu, J.-Y.; Font, J.; Barcons, V.; Verdaguer, A.; Chiesa, M. Investigating the Ubiquitous Presence of Nanometric Water Films on Surfaces. J. Phys. Chem. C **2021**, *125*, 15759–15772, DOI: 10.1021/acs.jpcc.1c03767.

(135) Carrasco, J.; Hodgson, A.; Michaelides, A. A Molecular Perspective of Water at Metal Interfaces. Nature Mater **2012**, *11*, 667–674, DOI: 10.1038/nmat3354.

(136) Henderson, M. A. The Interaction of Water with Solid Surfaces: Fundamental Aspects Revisited. Surface Science Reports **2002**, *46*, 1–308, DOI: 10.1016/S0167-5729(01)00020-6.

(137) Tan, J.; Zhang, J.; Li, C.; Luo, Y.; Ye, S. Ultrafast Energy Relaxation Dynamics of Amide I Vibrations Coupled with Protein-Bound Water Molecules. Nat Commun **2019**, *10*, 1010, DOI: 10.1038/s41467-019-08899-3.

(138) Zhang, Z.; Piatkowski, L.; Bakker, H. J.; Bonn, M. Ultrafast Vibrational Energy Transfer at the Water/Air Interface Revealed by Two-Dimensional Surface Vibrational Spectroscopy. Nature Chem **2011**, *3*, 888–893, DOI: 10.1038/nchem.1158.

(139) Cringus, D.; Yeremenko, S.; Pshenichnikov, M. S.; Wiersma, D. A. Hydrogen Bonding and Vibrational Energy Relaxation in Water-Acetonitrile Mixtures. J. Phys. Chem. B **2004**, *108*, 10376–10387, DOI: 10.1021/jp0495141.

(140) Karpovich, D. S.; Blanchard, G. J. Direct Measurement of the Adsorption Kinetics of Alkanethiolate Self-Assembled Monolayers on a Microcrystalline Gold Surface. Langmuir **1994**, *10*, 3315–3322, DOI: 10.1021/la00021a066.

(141) Rouhana, L. L.; Moussallem, M. D.; Schlenoff, J. B. Adsorption of Short-Chain Thiols and Disulfides onto Gold under Defined Mass Transport Conditions: Coverage, Kinetics, and Mechanism. J. Am. Chem. Soc. **2011**, *133*, 16080–16091, DOI: 10.1021/ja2041833.

(142) Fernández-Terán, R.; Hamm, P. A closer look into the distance dependence of vibrational energy transfer on surfaces using 2D IR spectroscopy. The Journal of Chemical Physics **2020**, *153*, 154706, DOI: 10.1063/5.0025787.

(143) Laß, K.; Han, X.; Hasselbrink, E. The Surprisingly Short Vibrational Lifetime of the Internal Stretch of CO Adsorbed on Si(100). The Journal of Chemical Physics **2005**, *123*, 051102, DOI: 10.1063/1.1993550.

(144) Kumar, S.; Jiang, H.; Schwarzer, M.; Kandratsenka, A.; Schwarzer, D.; Wodtke, A. M. Vibrational Relaxation Lifetime of a Physisorbed Molecule at a Metal Surface. Phys. Rev. Lett. **2019**, *123*, 156101, DOI: 10.1103/PhysRevLett.123.156101.

(145) Harris, A. L.; Levinos, N. J. Vibrational Energy Relaxation in a Molecular Monolayer at a Metal Surface. The Journal of Chemical Physics **1989**, *90*, 3878–3879, DOI: 10.1063/1.455795.

(146) Yu, Z.; Frontiera, R. R. Intermolecular Forces Dictate Vibrational Energy Transfer in Plasmonic–Molecule Systems. ACS Nano **2022**, *16*, 847–854, DOI: 10.1021/acsnano.1c08431.

(147) Dundas, K. O. H. M.; Beerepoot, M. T. P.; Ringholm, M.; Reine, S.; Bast, R.; List, N. H.; Kongsted, J.; Ruud, K.; Olsen, J. M. H. Harmonic Infrared and Raman Spectra in Molecular Environments Using the Polarizable Embedding Model. J. Chem. Theory Comput. **2021**, *17*, 3599–3617, DOI: 10.1021/acs.jctc.0c01323.

(148) Ramasesha, K.; De Marco, L.; Mandal, A.; Tokmakoff, A. Water Vibrations Have Strongly Mixed Intra- and Intermolecular Character. Nature Chem **2013**, *5*, 935–940, DOI: 10.1038/nchem.1757.

(149) Woutersen, S.; Bakker, H. J. Resonant Intermolecular Transfer of Vibrational Energy in Liquid Water. Nature **1999**, *402*, 507–509, DOI: 10.1038/990058.

(150) Yu, C.-C.; Chiang, K.-Y.; Okuno, M.; Seki, T.; Ohto, T.; Yu, X.; Korepanov, V.; Hamaguchi, H.-o.; Bonn, M.; Hunger, J.; Nagata, Y. Vibrational Couplings and Energy Transfer Pathways of Water's Bending Mode. Nat Commun **2020**, *11*, 5977, DOI: 10.1038/s41467-020-19759-w.

(151) Kumar, S.; Jiang, H.; Schwarzer, M.; Kandratsenka, A.; Schwarzer, D.; Wodtke, A. Vibrational Relaxation Lifetime of a Physisorbed Molecule at a Metal Surface. Physical Review Letters **2019**, *123*, 156101, DOI: 10.1103/PhysRevLett.123.156101.

(152) Harris, A. L.; Levinos, N. J. Vibrational energy relaxation in a molecular monolayer at a metal surface. The Journal of Chemical Physics **1989**, *90*, 3878–3879, DOI: 10.1063/1.455795.

(153) Mane, A. U.; Elam, J. W.; Goldberg, A.; Seidel, T. E.; Halls, M. D.; Current, M. I.; Despres, J.; Byl, O.; Tang, Y.; Sweeney, J. Atomic Layer Deposition of Boron-Containing Films Using B2F4. Journal of Vacuum Science & Technology A **2015**, *34*, 01A132, DOI: 10.1116/1.4935651.

(154) Bedrossian, P.; Meade, R. D.; Mortensen, K.; Chen, D. M.; Golovchenko, J. A.; Vanderbilt, D. Surface Doping and Stabilization of Si(111) with Boron. Phys. Rev. Lett. **1989**, *63*, 1257–1260, DOI: 10.1103/PhysRevLett.63.1257.

(155) Kalkofen, B.; Amusan, A. A.; Bukhari, M. S. K.; Garke, B.; Lisker, M.; Gargouri, H.; Burte, E. P. Use of B2O3 Films Grown by Plasma-Assisted Atomic Layer Deposition for Shallow Boron Doping in Silicon. Journal of Vacuum Science & Technology A **2015**, *33*, 031512, DOI: 10.1116/1.4917552.

(156) Mataga, N.; Karen, A.; Okada, T.; Nishitani, S.; Kurata, N.; Sakata, Y.; Misumi, S. Picosecond Dynamics of Photochemical Electron Transfer in Porphyrin-Quinone Intramolecular Exciplex Systems. J. Phys. Chem. **1984**, *88*, 5138–5141, DOI: 10.1021/j150666a002.